Sensorless Position Estimation in Fault-Tolerant Permanent Magnet AC Motor Drives with Redundancy

Jae Sam An

Thesis submitted for the degree of

Doctor of Philosophy

The School of Electrical & Electronic Engineering,
Faculty of Engineering, Computer & Mathematical Sciences,
The University of Adelaide, Australia

September 2010

Table of Contents

Abstract

Safety critical applications are heavily dependent on fault-tolerant motor drives being capable of continuing to operate satisfactorily under faults. This research utilizes a fault-tolerant PMAC motor drive with redundancy involving dual drives to provide parallel redundancy where each drive has electrically, magnetically, thermally and physically independent phases to improve its fault-tolerant capabilities. PMAC motor drives can offer high power and torque densities which are essential in high performance applications, for example, more-electric airplanes.

In this thesis, two sensorless algorithms are proposed to estimate the rotor position in a fault-tolerant three-phase surface-mounted sinusoidal PMAC motor drive with redundancy under normal and faulted operating conditions. The key aims are to improve the reliability by eliminating the use of a position sensor which is one of major sources of failures, as well as by offering fault-tolerant position estimation. The algorithms utilize measurements of the winding currents and phase voltages, to compute flux linkage increments without integration, hence producing the predicted position values. Estimation errors due to parameter variations and inaccurate measurements are compensated for by a modified phase-locked loop technique which forces the predicted positions to track the flux linkage increments, finally generating the rotor position estimate.

The fault-tolerant three-phase sensorless position estimation method utilizes the measured data from the three phase windings in each drive, consequently obtaining a total of two position estimates. However, the fault-tolerant two-phase sensorless position estimation method uses measurements from pairs of phases and produces three position estimates for each drive. Therefore, six position estimates are available in the dual drive system. In normal operation, all of these position estimates can be averaged to achieve a final rotor angle estimate in both schemes. Under faulted operating conditions, on the other hand, a final position estimate should be achieved by averaging position estimates obtained with measurements from healthy phases since unacceptable estimation errors can be created by making use of measured values from phases with failures.

In order to validate the effectiveness of the proposed fault-tolerant sensorless position estimation schemes, the algorithms were tested using both simulated data and offline measured data from an experimental fault-tolerant PMAC motor drive system.

In the healthy condition, both techniques presented good performance with acceptable accuracies under low and high steady-state speeds, starting from standstill and step load changes. In addition, they had robustness against parameter variations and measurement errors, as well as the ability to recover quickly from large incorrect initial position information. Under faulted operating conditions such as sensor failures, however, the two-phase sensorless method was more reliable than the three-phase sensorless method since it could operate even with a faulty phase.

Declaration

This work contains no material which has been accepted for the award of any other degree or diploma in any university or other tertiary institution to Jae Sam An and, to the best of my knowledge and belief, contains no material previously published or written by another person, except where due reference has been made in the text.

I give consent to this copy of my thesis, when deposited in the University Library, being made available for loan and photocopying, subject to the provisions of the Copyright Act 1968.

I also give permission for the digital version of my thesis to be made available on the web, via the University's digital research repository, the Library catalogue, the Australasian Digital Theses Program (ADTP) and also through web search engines, unless permission has been granted by the University to restrict access for a period of time.

Signed: _____ **Date:** _____

Acknowledgements

I wish to thank my supervisor, Associate Professor Nesimi Ertugrul, for his advice, guidance, idea, support, motivation and kindness during this research. I am also happy to thank my co-supervisor, Dr. Wen L. Soong, for his warmth, smile, direction, encouragement, knowledge, assistance and suggestion.

I would like to thank all colleagues in my laboratory for their support, encouragement and friendship. In particular, my thanks are going to Dr. Jingwei Zhu for his help in my experimental works by providing a fault-tolerant PMAC motor drive system and its control. Dr. Ameen Gargoom has given a lot of kind assistance for my LabVIEW programming tasks as well.

I am pleased to thank members of the School of Electrical and Electronic Engineering for their administrative assistance, computing support, technical help and friendship. I also thank staff of the international student centre of the University of Adelaide for their assistance in student VISA matters.

This thesis would not have been possible without my wife's endless love, encouragement and support. I am also grateful to my cute son for his birth during my study in Australia. I thank my family and relatives in Korea for their help.

Jae Sam An

September 2010,

Adelaide, Australia.

List of Figures

List of Tables

Symbols and Abbreviations

B	damping coefficient of the motor and mechanical load	Nm/rad/s
Δh	hysteresis bandwidth	A
Δi_a , Δi_b , Δi_c , Δi_u , Δi_v , Δi_w	phase current increments between samples	A
$\lvert\Delta\psi\rvert$	amplitude of the flux linkage increments	Wb
$\Delta\psi_a$, $\Delta\psi_b$, $\Delta\psi_c$, $\Delta\psi_u$, $\Delta\psi_v$, $\Delta\psi_w$	phase flux linkage increments between samples	Wb
Δt	sampling time	s
$\Delta\theta_a$, $\Delta\theta_b$, $\Delta\theta_c$, $\Delta\theta_u$, $\Delta\theta_v$, $\Delta\theta_w$	estimated electrical rotor position increments of corresponding phases between samples	rad
$\Delta\theta_{ab}$, $\Delta\theta_{bc}$, $\Delta\theta_{ca}$, $\Delta\theta_{uv}$, $\Delta\theta_{vw}$, $\Delta\theta_{wu}$	rotor position increments obtained by utilizing pairs of phases A-B, B-C, C-A, U-V, V-W and W-U in the fault-tolerant PMAC motor modules 1 and 2	rad
$\delta\theta_{ab}$, $\delta\theta_{bc}$, $\delta\theta_{ca}$, $\delta\theta_{uv}$, $\delta\theta_{vw}$, $\delta\theta_{wu}$	phase differences between the flux linkage increments and the back EMF functions with respect to the predicted rotor position for pairs of phases A-B, B-C, C-A, U-V, V-W and W-U in the motor modules 1 and 2	rad
$\Delta\theta_1$, $\Delta\theta_2$	rotor position increments in the motor modules 1 and 2	rad
$\delta\theta_1$, $\delta\theta_2$	phase differences between the phase angles of the flux linkage increments and the predicted rotor positions	rad
e_a , e_b , e_c ,	phase back EMF voltages	V

e_u, e_v, e_w		
$e_1(\theta)$, $e_2(\theta)$, $e_3(\theta)$, $e_4(\theta)$, $e_5(\theta)$, $e_6(\theta)$	phase back EMF functions	
i_a, i_b, i_c, i_u, i_v, i_w	phase currents	A
$i_a(0)$	initial value of winding current in phase A	A
i_a^*, i_b^*, i_c^*	reference phase currents for the stator windings of the motor module 1	A
I_m	amplitude of the excitation current command	A
J	inertia of the motor and connected load	kgm^2
K	gain of the phase detector	
k, $(k-1)$	integers representing the k-th and $(k-1)$-th sampling instants	
k_e	Back-EMF constant	V/rad/s
K_p, K_i	proportional and integral gains of the PI controller	
L	phase inductance	H
p	number of pole pairs	
ω_r	mechanical angular speed of the rotor	rad/s
$\frac{1}{s}$	integrator	
R	phase resistance	Ω
T_e	net electromagnetic torque	Nm
T_{ea}, T_{eb}, T_{ec}, T_{eu}, T_{ev}, T_{ew}	phase electromagnetic torques	Nm
T_{e1}, T_{e2}	electromagnetic torques generated by the motor modules 1 and 2	Nm

θ	electrical rotor position	rad
θ_{ab} , θ_{bc} , θ_{ca}	electrical rotor position estimates obtained between phases A-B, B-C and C-A	rad
$\theta^*_{ab}(k)$, $\theta^*_{bc}(k)$, $\theta^*_{ca}(k)$, $\theta^*_{uv}(k)$, $\theta^*_{vw}(k)$, $\theta^*_{wu}(k)$	predicted rotor position values	rad
$\theta_{ab}(k-1)$, $\theta_{bc}(k-1)$, $\theta_{ca}(k-1)$, $\theta_{uv}(k-1)$, $\theta_{vw}(k-1)$, $\theta_{wu}(k-1)$	rotor position estimates at the previous sampling instant $(k-1)$	rad
θ_{act}	actual electrical rotor position of the fault-tolerant PMAC motor drive	rad
ε_{ab} , ε_{bc} , ε_{ca}	position estimation errors given from phases A-B, B-C and C-A	rad
θ_{f1} , θ_{f2}	phase angles of the flux linkage increments	rad
$\theta_1(k)$, $\theta_2(k)$	rotor position estimates of the motor modules 1 and 2	rad
$\theta^*_1(k)$, $\theta^*_2(k)$	predicted electrical rotor position values of the motor modules 1 and 2	rad
θ_{3ph} , ε_{3ph}	electrical rotor position estimate and position estimation error of the motor module 1 obtained by the three-phase position estimator	rad
θ_{2ph} , ε_{2ph}	averaged electrical rotor position estimate and the averaged electrical position estimation error of the motor module 1 obtained by the two-phase position estimator	rad
$\theta_1(k-1)$, $\theta_2(k-1)$	previous electrical rotor position estimates obtained at the $(k-1)$-th instant	rad
θ_r	mechanical rotor position	rad

T_l	load torque	Nm
v_a, v_b, v_c, v_u, v_v, v_w	phase voltages	V
v_{AB}	terminal voltage drop between the point A and the point B	V
v_{AN}, v_{BN}	terminal voltages at the points A and B with respect to the earthed negative DC power supply rail, respectively	V
V_{dc}	DC link input power supply voltage for the conventional three-phase inverter	V
V_{dc1}, V_{dc2}	DC link power supply voltages for the three-phase H-bridge inverter sets 1 and 2	V
A (or a), B (or b), C (or c), U (or u), V (or v), W (or w)	phases of the motor modules 1 and 2	
AC	alternating current	
A/D	analog to digital	
BLDC	brushless direct current	
CPU	central processing unit	
CT	current transducer	
d-axis	direct axis	
DIO	digital input and output	
DC	direct current	
DC Supply 1, DC Supply 2	DC input power supplies	
D1, D2, D3, D4	freewheeling diodes	
d-q	direct-quadrature	

(d-axis or q-axis)	(direct-axis or quadrature-axis)
DSP	digital signal processor
EKF	extended Kalman filter
EMF	electromotive force
FDI	fault detection and isolation
GUI	graphical user interface
H-inverter	H-bridge type inverter
H/W	hardware
E	incremental encoder
INFORM	indirect flux detection by on-line reactance measurement
I/O	input and output
IPM	interior permanent magnet
IPMSM	interior permanent magnet synchronous motor
K	kilo
MOSFET	metal-oxide-semiconductor field-effect transistor
MS	mega samples
MSPS	mega samples per second
P rail, N rail	positive and negative DC power supply rails of the inverter
N, P	north and south magnetic poles of permanent magnets mounted on the rotor
PC	personal computer
PI	proportional integral
PLL	phase-locked loop
PM	permanent magnet
PMAC	permanent magnet alternating current
PMSM	permanent magnet synchronous motor

PPR	pulses per revolution
PWM	pulse width modulation
q-axis	quadrature axis
QEI	quadrature encoder interface
RMS	root mean square
rpm	revolutions per minute
RTSI	real-time system integration bus
SMPM	surface-mounted permanent magnet
SNR	signal-to-noise ratio
S1, S2, S3, S4	power switches
SPM	surface-mounted permanent magnet
SPMSM	surface permanent magnet synchronous motor
SRM	switched reluctance motor
S/W	software
UART	universal asynchronous receiver/transmitter
VI	virtual Instruments
ZOH	zero order hold

1. Introduction

1.1 Overview

Electric motor drives have been increasingly used in safety critical applications whose failure or malfunction may result in serious injury or death, large capital loss or severe harm to the environment. There are various well-known examples of safety critical applications such as electric vehicles, nuclear power plants, airplanes or defence systems [1-8, 10-24]. Such applications have greatly depended on reliable motor drives with the ability to continue to operate satisfactorily in the occurrence of faults. These motor drives can be termed as fault-tolerant motor drives [6-8, 10-24]. For example, when a fault occurs in an electric motor drive of an electric vehicle, the motor drive should be capable of continuing to run safely with modest performance degradation until it is stopped for repair.

Although a large number of faults are possible in fault-tolerant motor drives, a limited number of failures will be considered in this thesis such as

a) The inverter failures: power device short-circuit, power device open-circuit and DC link capacitor failure.

b) Motor winding failures: winding short-circuit at the terminals, turn-to-turn short-circuit in a phase winding, phase-to-phase short-circuit, phase-to-ground short-circuit, and winding open-circuit.

c) The sensor, controller and power source related failures: current sensor faults, voltage sensor faults, position sensor faults, controller faults and power input source faults.

1.2 Literature Review

Fault-Tolerant Motor Drives

Switched reluctance motors (SRMs) have inherent fault-tolerant features due to their magnetic and electrical isolated topologies [6-8]. As each phase is wound around separate stator poles using concentrated windings in a SRM, the phase windings are magnetically decoupled. This prevents a fault current in one winding from inducing high voltages in adjacent phases magnetically. If excitation of a faulty phase is removed in the SRM, a fault current cannot flow through the healthy phases. In addition, each phase is electrically isolated and uses a separate H-bridge inverter. The end-windings in the SRM do not overlap so that the possibility of a phase-to-phase fault is decreased significantly. The main drawbacks of the SRMs are high torque ripple, large vibration, high acoustic noise, low torque/power density and poor efficiency which may not be desirable in high performance applications such as aerospace where a low mass and high efficiency are critical [9-11, 14, 19-21, 23].

In contrast to the SRMs, permanent magnet alternating current (PMAC) motors have two sources of excitation. A conventional PMAC motor contains three-phase armature windings on the stator with an $Y-$ or $\Delta-$ type winding configuration and a rotor containing permanent magnets for providing the magnetic field. Using high performance permanent magnet (PM) materials such as rare earth PMs, it can achieve a high power/torque per volume and excellent dynamic performance. Therefore, PMAC motors have been increasingly utilized in high performance applications. However, conventional PMAC motors are not inherently fault-tolerant unlike the SRMs as they usually have phase windings which are coupled magnetically, electrically and thermally.

In order to obtain fault tolerance in PMAC motor drives, a modular winding design methodology can be adopted to achieve physical, magnetic, electrical and thermal isolation between phase windings [10-24]. It was reported in a comparative study in [10], that the fault-tolerant PMAC motor drive not only has the ability to achieve a similar degree of fault tolerance as the SRM drive but also can produce significantly larger torque and power densities than the SRM. It was found that the fault-tolerant PMAC motors contained surface-mounted permanent magnet rotors [10-22]. In these designs, Halbach array permanent magnets mounted on the rotor were utilized to increase the air gap flux density. In some of these works, near-ideal sinewave back EMF voltages were achieved [23, 24]. Different number of phases and back EMF profiles were also achieved in these studies including the motors with 3 phases [11-14], 4 phases [11, 15, 16, 23, 24], 5 phases [11,15-18] and 6 phases [10, 15, 16,19-22], and the motors

with trapezoidal [11] or sinusoidal back EMF voltages [10, 12-24]. In order to achieve a parallel redundancy in the case of a complete motor drive breakdown (such as a controller or power source failure), a dual fault-tolerant PMAC motor drive on a common rotor shaft was proposed in [12-14], which also offers redundancy.

Fault Detection

When a fault occurs in a phase winding or a power device of a motor drive, it may lead to a catastrophic failure or may deteriorate seriously the performance of the motor drive if suitable actions are not taken. Consequently, the fault should be detected and isolated at an early stage to carry out the suitable post-fault schemes minimizing the negative effect on the motor drive. In fault-tolerant PMAC motor drives, extensive fault detection and isolation (FDI) techniques have been proposed to detect the presence of faults accurately and eventually to isolate them [14, 18, 20-22].

An approach to detect turn to turn faults due to the insulation breakdown was based on sensing phase currents in a six-phase fault-tolerant synchronous PM motor drive for an aircraft fuel pump [20, 21]. In this phase current sensing scheme, a lookup table was established to characterise the machine in terms of measured flux linkages with respect to currents and rotor angles. In each PWM interval in the current controllers, the measured phase currents were compared with their expected values obtained from the lookup table to detect the shorted turn faults where predetermined threshold levels were decided experimentally. This technique was able to detect even a single shorted turn fault in real time.

In addition to the phase current sensing approach described above, other fault detection methods have been developed [14, 21]. One of them was based on the voltage drops measured across the conducting power switches in each H-bridge inverter utilizing on-state voltage sensors [21]. In this on-state voltage sensing algorithm, the voltage drop measured was basically a function of the current flowing into a power device. The voltage drop was compared with a pre-determined value to generate a digital signal indicating whether an excessive current was conducting through the power device or not. To detect and identify power device short-circuit faults and terminal short-circuit faults in the winding phases, this approach made use of the digital signals obtained with all four on-state voltage sensors in each H-bridge inverter.

Instead of the on-state voltage sensing methodology described above, an alternative method was proposed that was based on a design methodology utilizing the commercially available switch driver circuits in a fault-tolerant PM brushless motor drive with redundancy [14]. In order to diagnose potential faults in both the inverters and the motor windings, the phase current sensing algorithm was combined with the on-state voltage sensing scheme proposed in [21] or the fault detection method developed in [14]. However, a DC link capacitor fault was not considered in these papers.

A technique for a five-phase fault-tolerant PMAC motor drive was developed in [18] to rapidly detect open and short circuit faults during current regulation. In the paper, in order to investigate the behaviour of the machine under normal and faulted operating conditions involving a partially short-circuited winding, the machine was mathematically modelled and back EMF voltages were computed using the flux linkage data obtained from a two-dimensional finite element analysis. In addition, a diagnostic index was proposed to provide quantitative information about fault severity and the ability to identify the faulty phase with respect to electrical angle. The detection of short-circuit faults was based on frequency analysis of phase voltages in a current controlled drive. Although the method can provide early fault detection, it requires a voltage sensor for each phase.

A model-based fault detection and isolation technique has been developed to determine the presence of faults in a fault-tolerant six-phase PMAC motor drive in [22]. This model-based technique consisted of two main steps: residual generation and decision making. In this method, phase current estimators utilizing a system model produced estimates for the phase currents, which were then compared to the measured phase currents, generating residuals. To avoid spurious fault detection, suitable threshold levels were decided for the residuals with a sufficient safety margin to diagnose the occurrence of faults.

Remedial Control after Fault Detection

Once a failure has been detected and isolated in the motor drives, suitable remedial actions may be taken to avoid the fault propagation to the adjacent phases for allowing them to continue to run satisfactorily or to compensate a torque loss due to the fault. A number of post-fault strategies have been developed in the fault-tolerant PMAC motor drives [11, 14-17, 19-21].

Remedial approaches for open-circuit faults were addressed in multi-phase fault-tolerant brushless DC motor drives with 3, 4 or 5 phases, where the fault-tolerant brushless motor drives had surface-mounted permanent magnets and trapezoidal back EMF voltages, and the windings were excited with rectangular currents [11]. Although average output torque loss can be compensated by increasing current values in remaining winding phases after the occurrence of an open-circuit fault, high torque ripples are generated if there is an open circuit fault (such as a phase or power switch open circuit). In order to reduce the ripple torques, the RMS values of each remedial reference phase current are limited to current values which are higher values than the rated value.

In a six-phase fault-tolerant PM motor drive for an aircraft fuel pump, two approaches have been developed to assure continued operation of the motor drive in a satisfactory manner after detection of faults [19-21]. When a shorted turn fault was detected in a winding phase, the terminals of that faulted winding were short-circuited by simultaneously turning on two upper switches in a corresponding H-bridge inverter [20, 21]. In the case of a short-circuited power device, a phase containing the shorted power device was short-circuited by turning on either two upper or two lower power switches of an H-bridge inverter [19, 21].

In [15], an optimal torque control strategy was developed for fault-tolerant PM brushless motor drives to minimize a ripple torque under open-circuit or short-circuit faults. This technique can eliminate a severe torque ripple due to a faulted phase. However, large time harmonics in phase currents produced a significant eddy-current loss in permanent magnets mounted on the rotor. Some simulation results given in the paper confirmed the effect of the eddy-current loss in the fault-tolerant PM brushless machines with 4, 5 and 6 phases.

Two optimal torque control methods have been developed for fault-tolerant PM brushless ac motor drives in [16, 17]. In both constant torque and constant power operating regions, these methods were able to produce a ripple-free torque under healthy and faulty conditions involving open-circuit and short-circuit faults. Also, the copper loss was minimized within the current and voltage constraints. However, the effectiveness of the optimal control schemes was not verified by test results.

Three remedial strategies were proposed to compensate the torque loss due to faults in a fault-tolerant PM brushless motor drive with redundancy in [14].

Sensorless Position Estimation Schemes

As was stated previously, the PMAC motors can be divided into two categories based on the back EMF waveforms: trapezoidal PMAC motors with trapezoidal back EMF voltages and sinusoidal PMAC motors with sinusoidal back EMF voltages [25, 26]. In a trapezoidal PMAC motor (also known as a brushless DC motor), rectangular currents are applied to the stator windings to produce a maximum electromagnetic torque at minimum torque ripple. On the other hand, a sinusoidal PMAC motor should be excited with sinusoidal phase currents to obtain a constant torque. It can be noted that the winding excitation currents in both motors should be synchronized with the corresponding back EMF voltages varying with respect to the rotor angle. Therefore, the rotor position information should be known to generate suitable switching signals to drive a power converter for current commutation as well as current control.

The rotor position can be obtained directly with a position sensor such as Hall-effect sensors, an optical encoder or a resolver [25-27]. The position sensors can be the main source of failures and hence are a key factor in reducing the reliability of the drives [25-27]. The sensors are fragile and sensitive to environmental factors involving temperature, humidity, vibration, shock, noise or dust. In addition, they need maintenance and connection wires between the motor and the controller. The initial mechanical assembly also is critical to obtain high accuracy position sensing. Furthermore, the position sensors may increase rotor inertia, motor size and cost of the motor drives. Therefore, it is useful to obtain the rotor position information without utilizing a position sensor.

A number of rotor position estimation techniques have been proposed in the literature to obtain the rotor position in PMAC motors without using a position sensor [22, 36-63, 65-81]. In a trapezoidal PMAC motor, the rotor position detection is mainly based on back EMF sensing, third harmonic component sensing or detection of the conduction states of freewheeling diodes of the converter circuit in the unexcited phase [36-41]. However, these methods have poor performance at low speed regions and require special starting schemes [36, 41, 82].

Some other techniques are based on the estimation of the rotor position using state observers, Kalman filters, hypothetical rotor position or flux linkages which require measured terminal voltages and winding currents in the PMAC motor [42-63]. However, such techniques have several disadvantages. They require expensive and powerful processors since they perform complicated computations. In addition, most of these techniques are sensitive to parameter changes due to temperature and saturation. Furthermore, these schemes have limited performance at low speed operation mainly due to the integrator drift.

Numerous sensorless position estimation techniques to obtain the rotor position in the PMAC motors have utilized magnetic saliencies due to geometric construction (such as salient pole machines) or saturation [65-81]. However, there is no inherent saliency in surface-mounted PMAC machines where the magnetic saliencies may only be produced by the magnetic saturation. Although most of the magnetic-saliency based methods have utilized signal injection including pulses or sinusoidal signals to extract the rotor position information from the magnetic saliencies [68-81], a few techniques did not utilize an external signal to track the inductance variation that is rotor dependent [65-67]. One of the advantages of such techniques is that the rotor position can be obtained even at low rotor speeds and at starting, and they are robust to parameter variations. However, they heavily rely on the magnetic saliencies and have poor performance at high speeds.

Although a large number of rotor position sensorless control methods have been proposed in the literature for PMAC motors, the majority of them have not taken into account motor drive failures. In addition, no research has been reported for the position detection in the presence of faults within machine windings, power converters or sensors in a fault-tolerant PMAC motor drive with redundancy.

1.3 Objectives

It should be reported here that this thesis investigates and addresses the issues related to the position estimation techniques for the dual motor fault tolerant drive. Although it is necessary to detect all potential faults and to remove them before performing position estimation, the fault detection and remedial strategies are beyond the scope of this research as it was addressed in details in [14].

The objectives of the thesis are:

- To establish a mathematical modelling framework and a simulation model of the fault-tolerant PMAC motor drive with redundancy to examine its performance under steady-state and transient conditions.
- To develop sensorless position estimation methods based on measurements of both phase voltages and winding currents to obtain the rotor position information indirectly. The primary aim of the proposed sensorless algorithms is to improve the reliability of position sensing and also to enhance the fault tolerance capability of the motor drive by obtaining multiple position estimation in the case of a fault.
- To investigate the feasibility of the proposed sensorless position estimation schemes under normal and faulty operating conditions in the fault-tolerant PMAC motor drive with redundancy.
- To verify the effectiveness of the proposed sensorless position estimation method utilizing off-line test data obtained from a real motor drive under normal and faulty operation.

1.4 Outline of Thesis

This thesis consists of seven chapters. Chapter 2 introduces the operating principles of the fault-tolerant permanent magnet AC (PMAC) motor with redundancy utilized in this study. The inverter circuit, the current waveform and the torque control involving the conventional current control scheme are also explained briefly in the same chapter.

Chapter 3 provides a detailed survey of sensorless rotor position estimation methods in PMAC motors. The chapter classifies the sensorless techniques and provides brief explanations about their distinguishing characteristics. The starting schemes are also covered in the literature survey.

Chapter 4 focuses on modelling and computer simulation of the motor drive. The mathematical model is given using the voltage, electromagnetic torque and motion equations, and Simulink^{TM} block models are developed to examine the performance of the motor drive. The chapter provides simulation results to study the operation of the drive over a wide operating range including starting.

In order to estimate the rotor position and to improve the reliability of the motor drive with redundant rotor position estimates, Chapter 5 develops two sensorless position

estimation methods involving three-phase and two-phase sensorless position estimation methods, which are based on the measurements of the phase currents and the phase voltages. The computer simulation models are also presented in the chapter to study the effectiveness of the developed methods under various operating conditions.

In order to validate the effectiveness of the sensorless position estimation methods developed in the previous chapter, Chapter 6 provides experimental studies utilizing off line measured data. A custom-written LabVIEW^{TM} program has been used to measure the real data and also to process the data for position estimation. This chapter also examines the behaviour of the position estimation methods under normal and faulty operating conditions.

Chapter 7 provides a summary of the thesis and highlights several distinctive features of the proposed sensorless position estimation methods. Some suggestions are also provided in the chapter for the future research.

2. The Fault-Tolerant Motor Drive Topology and Control Principles

2.1 Introduction

In order to improve the reliability of the system in safety critical applications, a fault-tolerant PMAC motor drive with redundancy was developed in [14]. This drive takes advantage of a parallel redundancy design methodology, which consists of two identical fault-tolerant PMAC motor drives with a common shaft. In this arrangement, even if one motor drive breaks down completely due to a catastrophic failure, such as a power supply or controller fault, the second drive module can continue to operate, resulting in increased reliability and fault tolerance.

Although such drive topology can offer redundancy and fault tolerance, it has some disadvantages over the conventional three phase drives. The main disadvantages of this system are the increased size and the cost. As it can be seen dual motor drive modules contain two motors, 6 H-bridge inverters, two controllers, and two power supplies which increase the size and the cost of such system.

It should be noted that under normal operation both motor modules share the load equally in the drive as they are corrected to a common shaft. However, if there is a fault in the drive (which needs to be identified and removed by a suitable fault detection and post-fault remedial schemes) an optimal torque control strategy utilizing healthy phases only in both modules needs to be adapted to compensate the torque reduction [14].

Figure 2.1 shows a block diagram of a prototype built in [14] that is also utilized in this research. As illustrated in the figure, each motor drive module includes a fault-tolerant three-phase surface-mounted sinusoidal PMAC motor, three separate H-bridge inverters all connected to a common DC power supply (labelled as DC supply), a Digital Signal Processor (DSP) based controller and related feedback circuits. Encoder in the figure represents an incremental encoder connected for rotor position sensing, and verification of the position estimation.

In this chapter, the fault-tolerant three-phase surface-mounted sinusoidal PMAC motors and the inverter topologies which are utilized in this research will be explained.

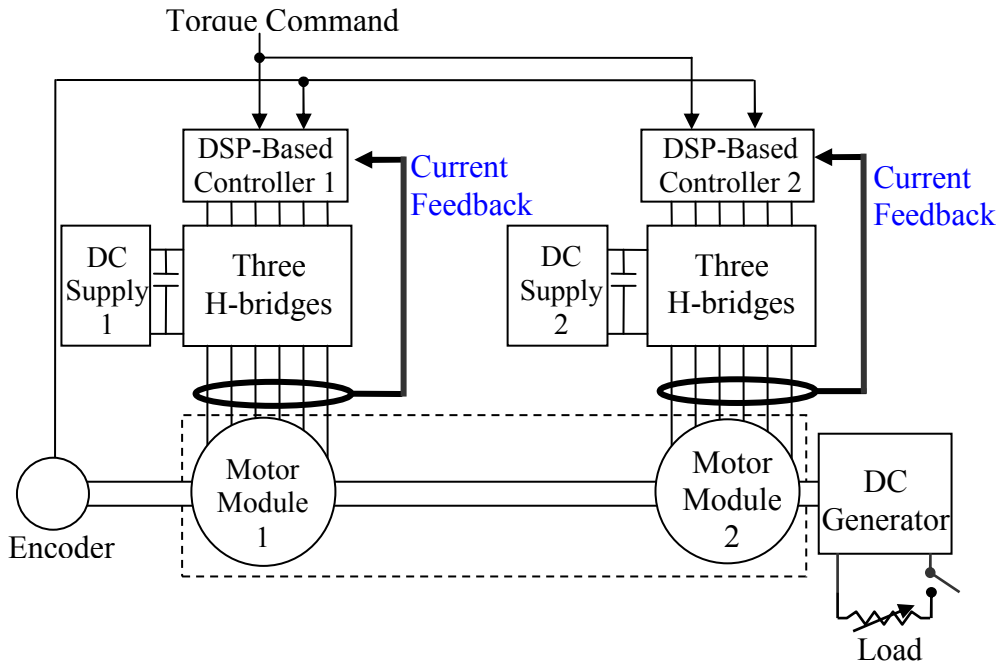

Figure 2.1 Block diagram of a prototype of the fault-tolerant three-phase surface-mounted sinusoidal PMAC motor drive system with redundancy.

2.2 The Motor and Inverter

2.2.1 The Brushless PM Motor Modules

In Figures 2.2 (a) and (b), conventional and fault-tolerant winding arrangements are demonstrated, where each PMAC motor contains 4 surface-mounted permanent magnet poles on the rotor and three stator phase windings. A, B and C represent the winding phases and N and S express the north and south magnetic poles of the permanent magnets mounted on the rotor. In the winding phases, sinusoidal back EMF voltages are induced due to the surface-mounted permanent magnets which are displaced with $2\pi/3$ electrical radians between phases. As shown in Figure 2.2 (a), the conventional winding arrangement in the stator generally does not give inherent fault-tolerant abilities as the conventional distributed configuration windings (Y or Δ connected windings) have both electrical and magnetic coupling between the phases [19].

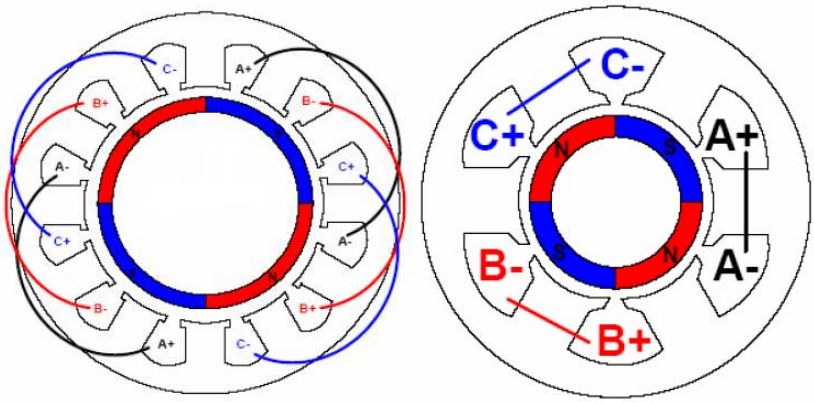

(a) (b)

Figure 2.2 (a) Conventional winding arrangement [28], (b) fault-tolerant winding arrangement [29] for a three-phase surface-mounted PMAC motor.

In order to obtain the fault tolerant winding configuration, however, each phase winding needs to be isolated electrically, magnetically, physically and thermally as shown in Figure 2.2 (b) [10, 14, 19-22] which includes concentrated winding design. This winding design (which is also utilized in this research) is capable of preventing a failure in a phase (such as a machine winding failure) from spreading to the adjacent phase windings, hence allowing the motor to continue to run in a satisfactory manner utilizing the remaining healthy phases. As shown in the figure, since each winding is wound around a single tooth, this arrangement minimises the occurrence of a phase to phase fault that is more serious than a failure in a single phase. This arrangement can also minimize the thermal and mutual magnetic coupling. To limit the short-circuit current to the rated current, 1 per unit inductance in each phase is also achieved by adjusting the depth and width of the slot during the design process.

2.2.2 Three-Phase H-Bridge Inverter

In order to provide electrical isolation between winding phases, each fault-tolerant three-phase PMAC motor module is driven by an inverter system that consists of three H-bridge inverters connected to a common DC power supply with a capacitor as illustrated in Figure 2.3 (b) [14]. As shown in Figure 2.3 (a), the conventional (non-isolated) three-phase inverter utilizes fewer power switches. However, the power switches in the fault-tolerant inverter configuration need to withstand only the phase voltage unlike the line voltage in the conventional Y-connected configuration [10, 14, 19, 21].

As shown in the figure, each H-bridge inverter drives one of the phases. Each inverter has four switching devices and four anti-parallel diodes that provide freewheeling paths to dissipate the stored energy in the motor winding during the turn-off period of the power switches. The two switches in each leg of the inverter are operated in complementary manner (when one is in its on-state, the other switch is in its off-state). However, in a practical system an additional time delay (the dead time) is also used to prevent a short circuit. The power switches and devices are assumed ideal in the simulation studies so that they are capable of turning off instantly and have no voltage drop during the conduction period.

In the H-bridge type inverter, the input is a constant DC input power supply voltage (V_{dc1}) as shown in Figure 2.3 (b). The output of the inverter is a phase voltage, which is equal to the terminal voltage and whose polarity can be changed by controlling the four power switches of the inverter using a pulse-width modulated (PWM) switching scheme. By controlling the output voltage, the magnitude and the direction of the output phase load current can be controlled.

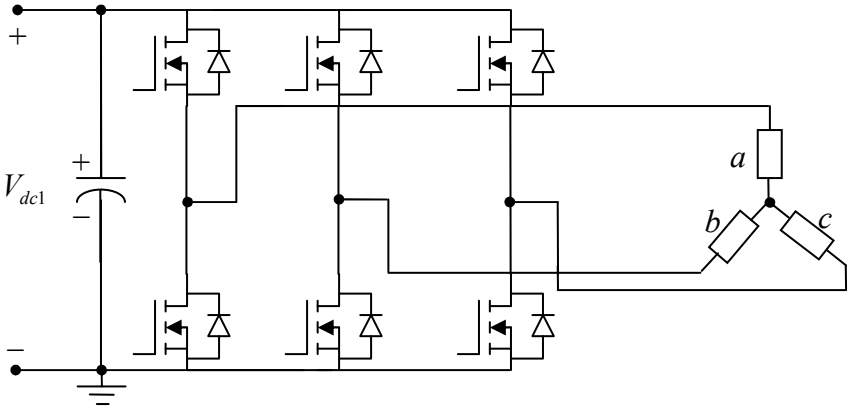

(a)

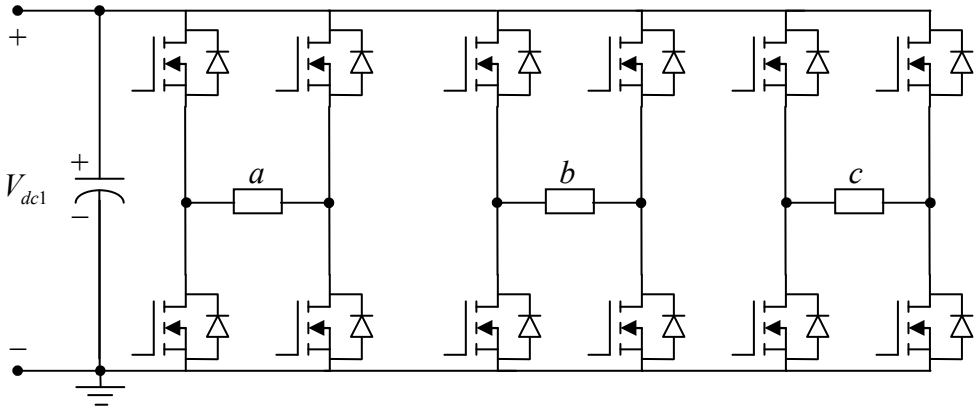

(b)

Figure 2.3 Schematic diagrams of a conventional three-phase inverter for a conventional PMAC motor with Y-type winding configuration (a) and a three-phase H-bridge inverter utilized in a fault-tolerant three-phase motor (b).

Bipolar Voltage PWM Switching Scheme of the H-Bridge Inverter

In this study, the bipolar voltage switching scheme is utilized to drive the H-bridge inverters [30]. In this type of switching method, diagonally opposite switches are turned on and off simultaneously. Therefore, the output voltage of the inverter varies between the positive DC input supply voltage ($+V_{dc1}$) and the negative DC input supply voltage ($-V_{dc1}$) as it will be demonstrated in Section 2.4.1. Although the switching signals for the inverter switches may be generated by various control strategies, the hysteresis current control scheme is used in this research.

2.3 Sinusoidal Current Excitation

In order to produce a constant electromagnetic torque in a surface-mounted PMAC motor with sinusoidal type back EMF voltages, sinusoidal excitation currents are required in the stator winding phases, which should be synchronized with the back EMF voltages [25, 26]. Each fault-tolerant three-phase PMAC motor module utilized in the study can be considered as a surface-mounted sinusoidal PMAC motor. The back EMF voltages of each module are aligned together. The modules are excited by sinusoidal winding currents to produce a constant total torque.

For the fault-tolerant motor module 1, the sinusoidal phase excitation currents can be expressed as a function of the instantaneous rotor position where the amplitude of the excitation current can be determined as in the torque control mode described in Section 2.4.2.

$$\begin{bmatrix} i_a^* \\ i_b^* \\ i_c^* \end{bmatrix} = I_m \begin{bmatrix} \sin(P\theta_r) \\ \sin(P\theta_r - \frac{2\pi}{3}) \\ \sin(P\theta_r - \frac{4\pi}{3}) \end{bmatrix} = I_m \begin{bmatrix} \sin(\theta) \\ \sin(\theta - \frac{2\pi}{3}) \\ \sin(\theta - \frac{4\pi}{3}) \end{bmatrix} \tag{5.1}$$

where I_m is the amplitude of the excitation current command, θ_r and θ are the mechanical and electrical rotor positions respectively, P is the number of pole pairs, and i_a^*, i_b^* and i_c^* are the reference phase currents for the stator windings of the motor module.

2.4 Current and Torque Control

In order to obtain the desired torque in each motor module, the phase currents should be regulated to follow the reference values as close as possible. Therefore, current and torque control approaches are briefly presented in this section.

2.4.1 Current Control

Hysteresis Current Control

Various current control techniques given in [30-35] can be used for brushless PM motor control, but the conventional hysteresis current control approach is employed in this

research to regulate the motor currents. Although the switching frequency does not remain constant in this method (it is a function of the inductance and the instantaneous back EMF voltage of the motor as well as the hysteresis bandwidth), it is simple to implement, robust and has excellent dynamic performance. In addition, it has an inherent feature to limit the peak current [30-35] that can be used to protect the inverter switches.

In this study, each motor module is driven by its hysteresis current controller, as shown in Figure 2.4. The hysteresis current controller is implemented with a closed-loop control system, where the phase current is measured by a current sensor and then compared with the reference current to generate the error signal. If the actual current exceeds the upper hysteresis band limit, the corresponding inverter switches are turned off to reduce the current. Conversely, if the actual current is lower than the hysteresis band limit, the load current is increased by controlling the inverter switches. Thus, the actual phase load current can be forced to track the reference current within a desired hysteresis band.

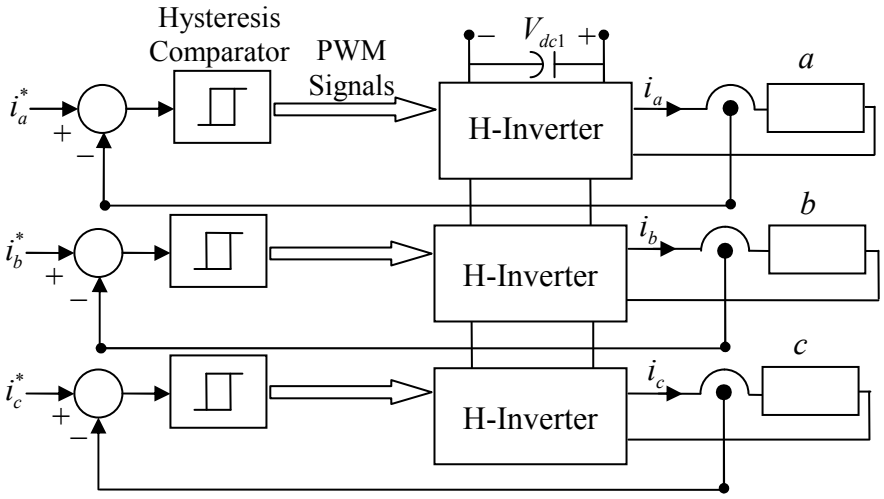

Figure 2.4 The schematic diagram of the hysteresis current control for the three-phase windings *a*, *b* and *c*.

Bipolar Voltage PWM Switching Technique in Hysteresis Current Control

Figure 2.5 shows a schematic diagram and typical waveforms of a hysteresis current regulated H-bridge inverter for winding phase A of one of the motor modules. In this control scheme, the H-bridge inverter is driven by the bipolar voltage PWM switching scheme as described earlier in Section 2.2.2.

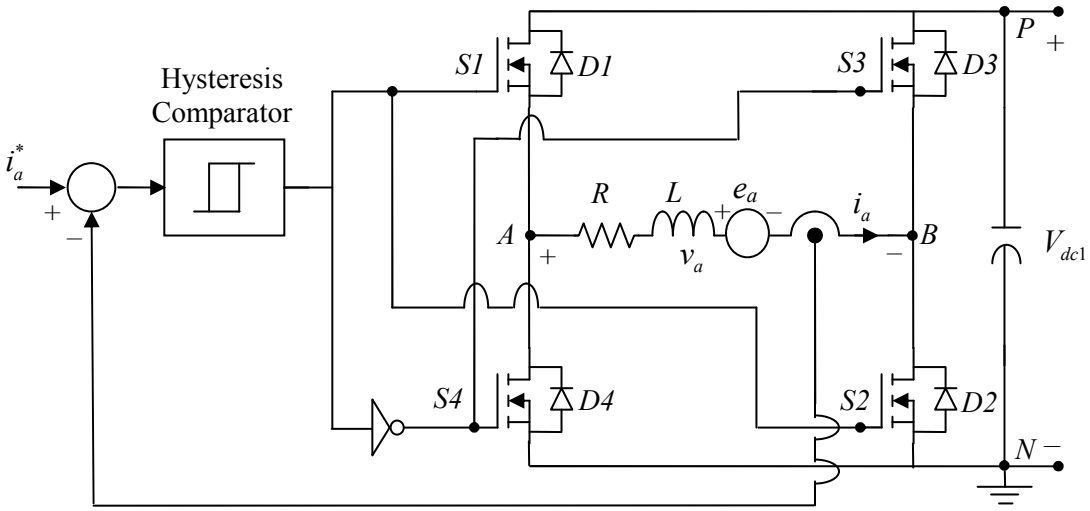

(a)

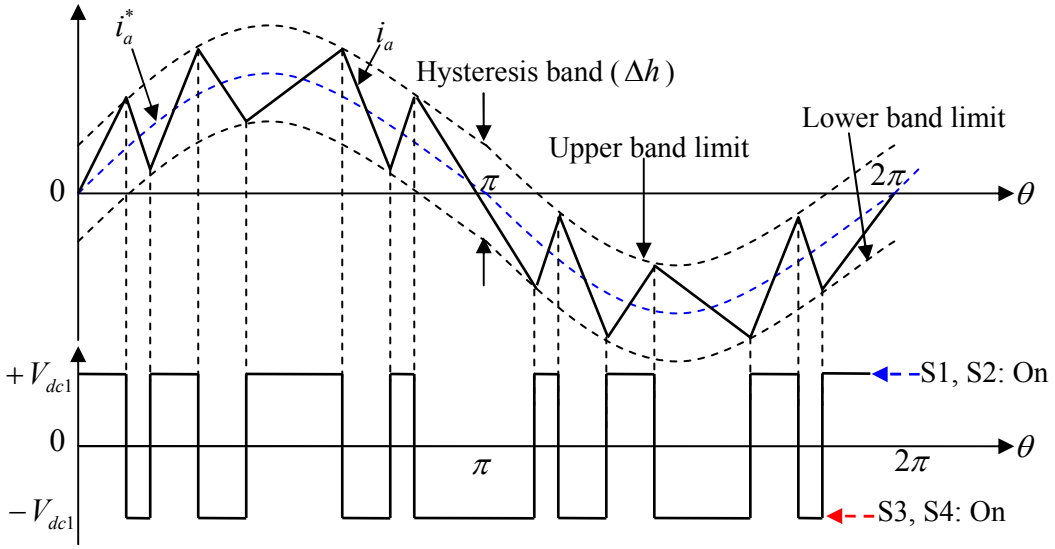

(b)

Figure 2.5 The principles of the operation of a hysteresis controller for one motor phase (a) Inverter schematic diagram, (b) typical waveforms of the inverter based on the bipolar voltage PWM switching modulation scheme.

As illustrated in Figure 2.5 (b), if the actual current i_a exceeds the upper hysteresis limit ($i_a \geq i_a^* + \Delta h/2$), the switch pair S3 and S4 of the inverter is turned on and the switch pair S1 and S2 is turned off, which applies a negative DC voltage to the phase winding that forces the actual current to decay. In this mode of operation, the terminal voltage at the point A (v_{AN}) is equal to 0 and the terminal voltage at the point B (v_{BN}) is equal to V_{dc1}. Therefore, the phase voltage across the load (v_a) is equal to the terminal

voltage drop ($v_{AB} = v_{AN} - v_{BN}$) between the point A and the point B which is obtained as $-V_{dc1}$.

The opposite switching occurs when the actual current drops below the lower limit of the hysteresis band ($i_a \le i_a^* - \Delta h/2$). The above switching states and corresponding terminal voltages for one of the motor phase is illustrated in Figure 2.5 (b).

Note that in the discussion above, the switches were assumed to be ideal, which allowed the states of the dual switch pairs in the H-bridge inverter to change simultaneously from on to off and vice versa. However, real power devices generally have a finite time to turn-on and turn-off. Therefore, to avoid a shoot-through fault in the H-bridge inverter, a dead time is usually inserted between the inverter switches on the same leg [30]. This means that all the switches of the H-bridge inverter should become off during the dead time. For example, if switch pair S1 and S2 turns off at a switching instant, the turn-on of the other switch pair (S3 and S4) should be delayed by the dead time. The dead time is chosen based on the turn-off times of the switching devices.

Note that during the dead time the phase voltage depends on the direction of the output current [25]. For example, when the phase current (i_a) is positive, the phase voltage will be equal to $-V_{dc1}$ as the output phase current flows through D4 to D3. On the other hand, when i_a is negative, the phase voltage becomes V_{dc1} due to the current flowing via D2 to D1. If the phase current is zero, the phase voltage will be identical to the back EMF voltage of that phase (e_a).

From the discussion above, it can be seen that the phase voltage of the stator winding depends on the switching states and the direction of the phase current. The above explanations can be given for all phases of the motor drive, which may involve multiple motor modules.

Table 2.1 illustrates the operation modes in the hysteresis current regulated H-bridge inverter utilizing the bipolar voltage switching scheme of the inverter given in Figure 2.5.

Table 2.1 Operation modes of the hysteresis current regulated H-bridge type inverter based on the bipolar voltage switching method in winding phase A of the motor drive in Figure 2.5.

Phase Current (i_a)	Switching Signals		Phase Voltage (v_a)
$i_a \geq i_a^* + \frac{\Delta h}{2}$	No Dead Time	$(S3, S4) : On$	$v_a = -V_{dc1}$
$i_a \leq i_a^* - \frac{\Delta h}{2}$		$(S1, S2) : On$	$v_a = V_{dc1}$
$i_a < 0$	Dead Time	$(S1, S2, S3, S4) : Off$	$v_a = V_{dc1}$
$i_a = 0$			$v_a = e_a$
$i_a > 0$			$v_a = -V_{dc1}$

2.4.2 Torque Control

The fault-tolerant PMAC motor module utilized in the study has surface-mounted permanent magnets on the rotor and sinusoidal back EMF waveforms in the stator windings, and the electromagnetic torque is directly proportional to the amplitude of the excitation currents. In addition, the sinusoidal winding currents are required to be in phase with the back EMF voltages of the winding phases to produce the constant torque [25]. Therefore, the output torque in the motor drive can be adjusted by regulating the phase currents which will be briefly explained below.

Figure 2.6 shows a block diagram of torque control for the motor module 1. As shown in the figure, the torque command input is given as the amplitude of the current command I_m. In the sinusoidal reference current generator, the reference phase winding currents are generated by the rotor position and I_m. Note that the rotor position information can be obtained by physical sensors or by a sensorless position estimation method.

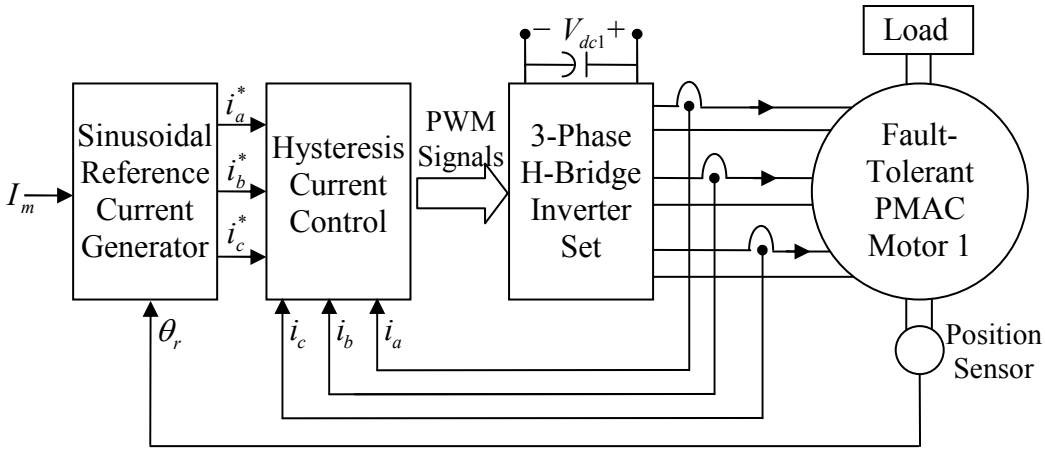

Figure 2.6 The schematic diagram of the torque control in the fault-tolerant three-phase PMAC motor drive.

2.5 Conclusion

This chapter summarized the principles of the current and torque control of the fault-tolerant PMAC motor drive with redundancy. The motor topology considered in the study involves two identical motor systems to offer redundancy against complete motor failure. Each motor module contains a fault-tolerant three-phase surface-mounted PMAC motor with sinusoidal back EMF voltages and three-phase H-bridge inverters with a common power DC input supply. Separate H-bridge inverters are employed to isolate the phase windings electrically. Magnetic and physical phase isolation is also introduced to the motor modules. The motor design also has 1 per unit phase inductance to limit the short-circuit winding current to the rated current.

The torque control approach involving the hysteresis current control strategy was also explained briefly in the chapter. The conventional hysteresis current controller for individual phases was considered in the control system to produce the switching signals to drive the corresponding H-bridge inverter. In this research, the H-bridge inverter is operated by the well-known bipolar voltage switching PWM method.

3. Survey of Sensorless Position Estimation Methods in PMAC Motors

3.1 Introduction

According to the back-EMF waveform, PMAC motors can be divided into two categories: brushless DC motors with trapezoidal back EMF (trapezoidal PMAC motors) and PM synchronous motors with sinusoidal back EMF (sinusoidal PMAC motors). As the name suggests, the back EMF of each phase has a trapezoidal shape back EMF waveforms with a 120 degrees flat-top in a trapezoidal PMAC motor with three phase windings. Therefore, in order to produce a smooth electromagnetic torque, the rectangular-shaped winding currents should be in phase with the back EMF voltages. To achieve this, the power devices of the inverter should be commutated every 60 degrees electrical based on the rotor position.

On the other hand, the sinusoidal PMAC motor with three-phase windings are required to be excited with sinusoidal winding currents to produce a constant electromagnetic torque where the excitation phase currents should also be synchronized with the back EMF voltages.

Conventionally, sensors such as Hall-Effect sensors, optical encoders or resolvers have been employed to obtain the rotor position information directly in PMAC motors. However, such sensors have various disadvantages and limitations. For example, they are weak and sensitive to environmental factors such as temperature, dust, humidity, vibration and shock, which may be the major source of failures in the motor drives to decrease the reliability of the motor drive significantly. Using sensors also increases the cost, system inertia and size of the motor drive. Special mechanical arrangements are required to mount them on the shaft to ensure reliability and accuracy. In addition, a number of electrical connection wires between the motor and the controller also increases. Therefore, a number of position estimation techniques have been investigated in the PMAC motors to eliminate or reduce the above mentioned disadvantages and limitations.

The layout of this chapter is as follows. In Section 3.2, the sensorless position detection methods for trapezoidal PMAC motors are discussed. Next in Section 3.3, the indirect position estimation techniques are provided for sinusoidal PMAC motors, some of which may also be applied to trapezoidal PMAC motors. Special starting schemes are discussed in Section 3.4. Finally, Section 3.5 draws conclusions and summarises the results.

3.2 Sensorless Position Estimation Methods in Trapezoidal PMAC Motors

In a brushless DC motor (a trapezoidal PMAC motor) with three phase windings, the back EMF of each phase has a trapezoidal waveform with a 120° electrical flat top which requires only two of the three phases to be excited at any instant. With respect to the rotor position, the power devices usually are commutated sequentially in every 60° electrical to synchronize the winding excitation to the back EMF waveform. Ideally, the back EMF waveforms should be in phase with the stator current to produce the maximum electromagnetic torque. To obtain the rotor position without using an electromechanical position sensor, numerous sensorless position estimation algorithms have been proposed in the literature.

3.2.1 Techniques Based on the Back EMF Detection

A method presented in [36] was based on measuring the back EMF waveform of the unexcited phase to determine the electronic commutation instants. In this reference, the three terminal voltages and the neutral voltage of the motor with respect to the negative DC bus voltage were measured to detect the instant at which the back EMF of the unexcited phase crossed zero. The terminal voltage was equal to the neutral voltage at the instant of the zero crossing of the back EMF waveform. In order to utilize the zero crossing point to generate the switching sequence, this detected point was phase shifted by 90° electrical in the method. A drawback of this technique is its lack of robustness at low speeds, since the back EMF amplitude is a direct function of the motor speed. In addition, the method is sensitive to noise due to the inverter switching in detecting the zero crossing instant.

In [37], position estimation was achieved by integrating the back EMF of an unexcited phase to reduce switching noise sensitivity and to adjust the inverter switching instants automatically with respect to the rotor speed variation. In this method, the open phase back EMF was integrated from the zero crossing instant to a pre-set threshold level where the threshold voltage was kept constant throughout the speed range. However, the back EMF integration approach is parameter dependent since the threshold is a function of the back EMF constant which may vary as a function of the temperature.

In order to eliminate the parameter dependency of the back EMF integration method mentioned above, an approach in [38] utilized a variable threshold level in a brushless DC motor for variable-speed household refrigerators. Similar to the previous scheme in [37], the open phase back EMF at first was integrated from the zero crossing point until the integral (called the commutation integral) reached a threshold level. Next, the new open phase back EMF was integrated to the back EMF zero crossing. Then, the resulting integral was compared to the commutation integral. If two integrals did not match, the threshold level was adjusted to allow the integrals to be identical.

The back EMF based schemes show good performance in the medium to high speed range. However, the common problem of these schemes is that the performance is dependent on the rotor speed because the magnitude of back EMF voltage is proportional to the rotor speed. This fact causes the variation of the signal-to-noise ratio according to the rotor speed and degrades the performance of the back EMF based methods when the rotor rotates at a low speed where the magnitude of the back EMF voltage is very small or zero.

3.2.2 Techniques Based on the Stator Third Harmonic Voltage

The third harmonic of the back EMF can be used in determination of the switching instants in the 120° electrical current conduction mode in a star-connected trapezoidal PMAC motor [39, 40]. In this type of motor, the open-circuit stator phase voltages (back EMF voltages) have trapezoidal waveform voltages that contain a fundamental and higher-order frequency harmonics. In the method, the third harmonic component was extracted from the stator phase voltages while the fundamental component was eliminated by the summation of the three phase voltages. The other higher order components obtained from the summation of the three phase voltages were eliminated

by using a low pass filter. The resulting third harmonic signal provides a constant phase relationship with the rotor flux under any speed and load condition. In order to detect the third harmonic voltage, a three-phase network with Y-type resistor configuration was connected across the Y-connected motor windings. The voltage across the two neutrals (between the neutral of the resistor network and the neutral of the motor windings) determined the third harmonic voltage. This voltage was integrated and was input to a zero crossing detector which was utilized to determine the switching sequence in the inverter.

Unlike the back EMF-based methods, the third harmonic signal is usually free of the inverter switching noise. As a result, the technique is not sensitive to delays of filters and shows better performance over a broader speed range than the back EMF methods described earlier. In addition, since the third harmonic can be detected at low speeds, this method can obtain a better starting performance than the back EMF based techniques. On the other hand, it is not easy to obtain the relative phase relationship between the third harmonic and the corresponding phase at low speeds because the third harmonic component has relatively low values at low speeds, and is also effected by saturation.

3.2.3 Techniques Based on Conducting States of Free-Wheeling Diodes

The rotor position information can be determined using the conducting states of the free-wheeling diodes of the inverter in an unexcited phase of a trapezoidal PMAC motor [41]. As was stated previously, in the 120° electrical operation of a trapezoidal PMAC motor with Y-type configuration, one of the three winding phases is always open-circuited. For a short period after opening the phase, the phase current flows via a free-wheeling diode of the inverter. This open-phase current becomes zero in the middle of the commutation interval that corresponds to the instant where the back EMF of the unexcited phase crosses zero. The position information can be obtained every 60° electrical by detecting whether the free-wheeling diodes are conducting or not. This approach however gives limited performance at low speeds. Furthermore, the method requires six additional isolated power supplies, one for the comparator circuitry of each free-wheeling diode in the inverter.

3.3 Sensorless Position Estimation Methods in Sinusoidal PMAC Motors

A PM synchronous motor (PMSM) or a sinusoidal PMAC motor has basically the back EMF voltages with sinusoidal waveforms. Hence, the sinusoidal PMAC motor essentially requires sinusoidal stator winding currents to generate a constant electromagnetic torque, which should also be in phase with the back EMF voltages. Unlike a trapezoidal PMAC motor with 120° electrical conduction, more accurate rotor position feedback is required in the sinusoidal PMAC motor continuously. A range of techniques have been developed to control the sinusoidal PMAC motor without using a position sensor which will be briefly explained below.

3.3.1 Techniques Based on the Flux Linkages

Several sensorless position estimation methods have been developed which measure the currents and terminal voltages and estimate the flux linkages of the sinusoidal PMAC motors. The basic principle of the methods is based on the orientation in the stationary reference frame. The three phase sinusoidal currents and the voltages, hence the flux linkages, of a sinusoidal PMAC motor can form three rotating phasors. These phasors rotate synchronously in the stationary reference frame and therefore the phase of the stator flux linkage phasor reflects the rotor position information of the motor.

In [42-45], the position information was determined by using the measurements of the motor terminal voltages and the line currents to calculate the flux linkages. The algorithms contained a two current-loop configuration to be utilized to correct the predicted position and the flux linkage estimates respectively. The proposed algorithms were applied to both the trapezoidal and the sinusoidal PMAC motors. Although the algorithms had been tested using off-line real data in [42, 43], the method was also tested using a DSP-based system in a closed loop real-time system in [44]. In addition, the machine nonlinearities such as saturation were taken into account in [45] which was the continuation of the previous studies. The performance of the algorithms presented in the literature depends on the quality and accuracy of the estimated flux linkages and measured values of voltages and currents. Parameter variations due to temperature and saturation also affect the accuracy of the position information in this method even under

a constant speed operation. Another drawback is that the algorithm cannot perform at low and zero speeds.

A six-phase fault-tolerant PMAC motor drive is investigated in [22]. In order to improve the reliability of such drive, two indirect position estimation schemes are also proposed for aero-engine fuel pumps in electric aircraft application. To estimate the rotor position, two different estimation techniques were proposed in [22]: the individual phase based estimation and all phase estimation. Both methods utilize the mathematical model of the six-phase fault-tolerant PMAC motor based on the relationship between the flux linkage, the current and the rotor position, hence requiring voltage and current measurements in all six phases.

As the name indicates, the indirect phase based estimation obtains a single rotor position estimate for each phase winding utilizing the phase voltage and the phase current measurements resulting six different rotor position estimates in total. On the other hand, the all phase estimation method uses the measured information from all six phases to produce a single rotor position estimate, which is more accurate than the previous technique. However, it is prone to failure as it requires healthy measurements in all phases. Although the developed estimation schemes in [22] offer significant improvements for position estimation in fault tolerant motor drives, their performance is limited at low speeds since both techniques perform poorly due to the integration drift in the flux linkage calculation..

When the stator flux linkage phasor has been determined, the instantaneous phase angle of the rotating phasor can be directly derived by an arc tangent function. If the stator power factor has to be unity, the phase angle can be used as the rotor position information to create the appropriate current command signals as described in [46]. The motor drive system controlled by this position information can achieve near unity power factor over a wide range of torque and speed. However, unity power factor is not always required by most applications of sinusoidal PMAC motor drives. In addition, the accuracy of the position and the speed calculation is limited by the integration drift in the calculation of the stator flux linkages.

To avoid the integration drift in the flux linkage computations, an improved method was proposed in [47]. The proposed method used the voltages and currents to directly calculate the phase angle of the stator flux linkage instead of conventional flux linkage

calculation based on an integration method. Moreover, a load angle, which was estimated based on the steady state relationship between the torque and the flux linkage, was introduced to compensate the difference between the rotor position and the stator flux linkage angle. However, two major problems still exist in this approach. The first one is that it is sensitive to noise in the measured voltages and currents, which may include high frequency harmonic components due to the PWM control, and delays in the low pass filter. The second problem is the difficulty of the trigonometric function calculation for the phase of the stator flux linkage using the two flux-linkage components, which are sinusoidal functions.

3.3.2 Techniques Based on Kalman Filters

Since a PMSM is a nonlinear dynamic system, extended Kalman filter (EKF) schemes have been used to estimate states in the PMSM involving the rotor position and the rotor speed in [48-53]. Besides the estimation of the rotor position and speed, the estimated states include the stator currents [48-50, 52, 53] or the stator flux linkages [51]. In addition, the load torque estimation was also obtained on-line to improve the estimation of mechanical states of the motor drive in [52]. Most of the EKF based observers were based on state-space models in the stator reference frame for the PMSMs as shown in [48-51]. However, state models for interior PMSMs were usually proposed in the rotor reference frame as shown in [52, 53] to reduce computing time required by the EKF in the stator reference frame and to simplify the motor equations. Furthermore, although measurements of stator voltages and winding currents were utilized in some of the EKF techniques as shown in [48, 51, 52], the others utilized measured winding currents and voltage references instead of the use of the measured stator voltages as seen in [49, 50, 53]. In [49], a self-tuning strategy of the covariance matrices for the EKF was developed for a surface-mounted PMSM to avoid the disadvantages due to conventional trial-and-error tuning methods.

The EKF based observer requires a powerful signal processor to perform the complicated mathematical computations and to manipulate large amounts of data [48, 52]. In addition, as the EKF method is sensitive to parameter variations, an on-line parameter identification scheme is required to be employed in the control system to achieve greater robustness and reliability of the filter [52].

3.3.3 Techniques Based on State Observers

A number of papers have been published regarding estimating the electrical and mechanical states of the sinusoidal PMAC motor using observers [54-63]. Nonlinear state observers were utilized to estimate the rotor position and the rotor speed of a PMSM in [54, 55]. These observers were based on the electrical and mechanical equations of the motor. In [54], a state-space model for a PMSM was developed in the rotating reference frame. However, a model described in the stationary reference frame was obtained for a surface-mounted PMSM in [55]. In order for the nonlinear state observers to be stable, the gains of the observers have to be optimized. However, it is complicated to determine optimum gains of the nonlinear observers under all operating conditions due to the nonlinearity of the motor. In addition, these nonlinear observers require knowing mechanical parameters of the motor such as the machine inertia and the load torque which are not easily detected and vary during normal operation.

To improve the difficulty in achieving the optimum gains of the observer due to non-linearity of the PMSM, reduced order state observers were proposed in [56-62]. In [56], a reduced order observer was based on a linear state-space model in the rotating reference frame for a PMSM. The motor model involved electrical and mechanical equations and contained four states: the d- and q-axis currents, the rotor position and the rotor speed. In the model, nonlinear terms were eliminated by adopting suitable control inputs and by neglecting the coulomb friction of the mechanical equation. Utilizing the linearised model, the observer directly produced estimates of the rotor position and the rotor speed. This reduced order observer simplifies the system and has less computational burden than a full order state observer or an extended Kalman filter technique. However, it still needs to know machine mechanical parameters such as the motor inertia, the load torque and the viscous damping coefficient.

In [57], the rotor position and the rotor speed were obtained by the use of a reduced order observer based on back EMF estimation in a PMSM. With the assumption that the rotor speed was constant during every short sampling interval, a linear motor model was developed in the stationary reference frame, which contained four states involving stator currents and back EMF voltages for the stationary reference frame. The rotor position and the rotor speed were obtained by the use of the back EMF voltages estimated by the

observer. The main benefit of this method does not need to know the mechanical parameters of the motor as the model did not include mechanical equations.

In order to estimate the rotor position and the rotor speed of an IPMSM, sensorless schemes have been described based on a motor model with an extended back EMF voltage either in the stationary reference frame [58] or in the rotating reference frame [59-61]. In the methods, the extended back EMF voltage contains the rotor position information consisting of the back EMF voltage generated by permanent magnets and a voltage due to the saliency of the motor. For medium and high operating speeds, a reduced order observer was utilized to estimate the extended EMF. Using the estimated values of the extended EMF, the rotor position and the rotor speed were estimated.

The difference between the detected actual state variables and the estimated state variables was used to obtain the position information in [62]. The procedure reported in [62] is based on the analytical model of the motor. In the control strategy in [62], the measured three phase voltages and currents were transformed to a hypothetical coordinate system. Then, the hypothetical voltages were determined based on the measured current and the motor model. In the final stage, the angular difference between the actual and hypothetical axes was estimated by the voltage difference between the actual and the hypothetical axes. Self-synchronization was achieved by making the angular difference zero and by changing the calculated speed of the motor. However, the method proposed in [62] is dependent on the accuracy of the measured currents and/or the voltages, and is also sensitive to the motor parameter variations. As in the back EMF based position detection method, this technique also fails at low operating speeds and is computationally intensive requiring fast processors.

In order to obtain the rotor position and the rotor speed of a surface-mounted PMSM (SPMSM), an adaptive sliding mode observer was developed based on the current estimation in [63]. In the method, the flux due to the permanent magnets on the rotor was utilized as a state variable to achieve a linear model of the motor. Due to the linear motor model, the stability of the sliding mode observer was easily guaranteed. The pole assignment was also simplified since the order was reduced in the error equation of the observer.

Generally, the state observers are heavily dependent on the machine parameters. Therefore, performance of the rotor position estimation will deteriorate as the

parameters of the machine vary with thermal and operational conditions. This problem may be overcome to some degree by using an on-line parameter identification scheme as seen in [64], but the on-line tuning increases the computational burden in implementation. In addition, as seen in the back EMF based sensorless techniques, these schemes also fail to operate in the low speed range.

3.3.4 Techniques Based on Magnetic Saliencies

Generally, PMAC motors have magnetic saliencies due to their geometric construction as in the case of PMAC motors with buried (or interior) permanent magnets (salient pole PMAC motors) or saturation effects as in the case of PMAC motors with surface-mounted permanent magnets (nonsalient pole PMAC motors). An interior PM motor (IPM) has significantly different inductances between the d and q-axis due to the structure while the inductances in the d and q-axis of a surface-mounted PM motor (SPM) are approximately equal. In most of IPM motors, the motor inductance in the q-axis is greater than the inductance in the d-axis because of the low permeability of the magnet material [65]. The different inductance between the d-axis and q-axis means that the inductance is a function of the rotor position. On the other hand, saliencies due to saturation are not fixed to the rotor position and their locations move in the machine with the magnitudes of the stator currents. Various techniques have been proposed to estimate the rotor position based on the magnetic saliencies.

In order to determine the rotor position, the inductance variation was tracked without utilizing a signal injection method in [65-67]. In [65], an approach to the position sensor elimination of an IPM synchronous motor drive was proposed. The phase inductance dependent on the rotor position was calculated by utilizing the instantaneous voltages and the instantaneous currents in the IPM motor fed by a current-regulated PWM (pulsewidth modulation) converter. Then, the calculated phase inductance was employed to obtain the rotor position estimate with the use of a look-up table relating the phase inductance and the rotor position.

Another approach to real-time position estimation based on inductance variation was introduced to an IPM synchronous motor driven by a voltage source PWM inverter [66, 67]. The algorithm calculated the inductance matrix including rotor position information from the detected current harmonics produced by the switching of the inverter. It estimated the rotor position every PWM period without any signal injection at standstill

and at low speeds. This method relies on the saliency of the IPM motor. The matrix mathematics and vector calculations are complicated.

For using the magnetic saliencies in PMAC motors to detect the position of the rotor, the signal injection methods are categorized into pulse injection [68-70] and sinusoidal injection [71-81]. In order to obtain the rotor position and the rotor speed at low speeds including zero speed, a solution was based on the winding inductance variation with the rotor position in a salient-pole PMSM in [68]. This method injected pilot voltage pulses of rectangular type every 30 samplings in the current control loop to the stator windings and the current response produced by the pilot pulse injection was dependent on the rotor position due to the winding inductance of the salient-pole PMSM. The rotor position and the rotor speed were estimated with the use of the relationship between the current response and the rotor position.

To utilize the magnetic saliencies either due to geometric construction as in the case of a salient-pole PMAC motor or due to saturation effects as in the case of a non-salient pole PMAC motor at low speeds and standstill, a sensorless position estimation technique was based on a test voltage phasor injection to the stator windings in [69, 70]. This method was called the indirect flux detection by on-line reactance measurement (INFORM) method. When discrete test voltages were applied to the motor via an inverter during a short time period, the change of the resulting current space phasor was measured. This process was repeated in various space phasor directions to determine the magnetic anisotrophy. Then, discrete rotor position estimates were obtained by using the magnetic anisotropy. Due to the discrete position detection, a Kalman filter was employed to improve the accuracy of the rotor position in [69]. Although this method presented reliable operating performance in the low speed region including the standstill, it was required to be changed to the other sensorless method such as a back EMF-based technique in a high speed range [69].

However, the excitation current pulses may generate a torque to rotate the motor, which may move the initial rotor position. In addition, it is difficult to estimate the rotor position accurately in these methods due to the problem in detecting the current amplitude accurately.

Sinusoidal signal injection methods to determine the rotor position based on magnetic saliencies are divided into two groups; current injection schemes [71] and voltage

injection techniques [72-81] involving rotating [72-76] and fluctuating excitation methods [77-81]. In [71], a sensorless control technique was described based on injection of a harmonic current vector to obtain the rotor position in an interior PMSM without using mechanical position sensors. The strategy injected a harmonic current vector with small amplitude to the machine. Then, the harmonic injected current vector and the corresponding harmonic voltage vector were filtered to obtain the harmonic reactive power having a relative phase with a phase reference signal. To estimate the rotor position, the relative phase difference, which was proportional to the position estimation error, was removed by utilizing a phase-locked loop (PLL) technique. The proposed technique showed good performance from zero to the rated rotor speed. Also, the method was robust against motor parameters and operating conditions such as a rotor speed and motor load.

For tracking the magnetic saliencies of a PMSM, high frequency rotating voltages were injected to the motor windings to estimate the rotor position in [72-76]. In order to obtain the rotor position, sensorless estimation techniques were based on detecting the magnetic saliency of a salient pole PMAC motor due to its structure which utilized a rotating voltage signal injection with a high frequency [72-74]. Such methods have an excellent performance in the low speed region including zero speed and are not sensitive to motor parameter variations. However, the methods depend on the inductance variation due to the geometry of the motor.

Another rotating voltage injection approach was applied for both salient and non-salient PMSM drives based on making use of the anisotropy of PMSMs [75]. Although in IPM synchronous motors, the same algorithm as shown in [72] was used to estimate the rotor position, the local anisotropy induced by saturation due to the magnet flux was considered in surface-mounted PMSMs and brushless DC motors without salient construction. A form of local magnetic anisotropy is induced in an SPMSM by the presence of the magnet flux. Such a saliency is generally much lower than the inherent saliency of an IPMSM, but allows considering all PMSMs as salient structures. Effects of the saturation produced by the magnet flux are used to detect the position of the rotor at standstill in order to initialize the sensorless position estimation. It works well from zero speed to the rated value. However, it is not sufficient for servo applications. In [76], multiple spatial saliencies in an AC machine were considered to provide estimates of flux angle, rotor position and velocity with wide bandwidth and high accuracy.

These schemes do not require the knowledge of any motor parameters. However, the dynamic performance is restricted in relation to the frequency of the injected signal in the methods because they utilize a rotating high frequency signal. Also, the additional voltage component may generate torque and hence affect the rotor position at standstill.

A high frequency pulsating voltage vector [77-81] in the estimated synchronous frame is injected into an IPM machine [77-79] and an SMPM motor [79-81] for the position estimation. In [77], a technique was applied to a salient pole PMSM that utilized a high frequency fluctuating voltage injection in the estimated rotor flux direction to estimate the rotor position and speed at standstill and high speeds. This utilizes an injected pulsating voltage signal at known frequency to extract information from a spatial saliency in an IPM motor. In the rotor reference frame, the d and q axis of the motor were decoupled from each other to reduce the number of additional functions that were required to produce the position estimate. The methods based on spatial inductance variations have the desired effect that they can operate at zero speed, however, many of these techniques have an upper limit on the operating speed range due to effects of back-EMF at high speeds.

In an IPM drive system, a sensorless method based on the characteristics of the high frequency impedance was proposed to obtain the rotor position and speed at standstill and low speeds [78]. In the paper, a high frequency fluctuating voltage signal injection was applied to amplify the impedance difference containing the information of the rotor position and to maintain a reasonable performance under any load conditions. The scheme extracts the high frequency impedance components related to the rotor position. The scheme contained the ability to start from an arbitrary rotor position and was able to distinguish the north magnetic pole position from the south one.

In [79], a proposed sensorless technique is based on tracking of the saliency of PM synchronous motors (both buried PM motors and surface-mounted PM motors) at low speeds including standstill to estimate the rotor position and speed. A fluctuating high frequency voltage is injected in the stator and the inductive and resistive components of the stator impedance are evaluated to detect the rotor position. Although the rotor position is tracked based on the inductance saliency in buried PM motors, the power losses due to eddy currents in the magnets are monitored and are used to detect the d axis direction for SMPM motors since the inductance saliency is negligible.

A high frequency fluctuating voltage signal injection scheme is applied to an SMPM motor to utilize the high frequency impedance difference due to the magnetic saliency [80, 81]. In the SMPM motor, the stator core around the q axis winding is saturated due to the flux of the permanent magnet. This makes the magnetic saliency in the motor including the rotor position information. In the method, the high frequency fluctuating voltage signal is injected on the d axis in the estimated synchronous reference frame and the q axis component of high frequency current in the estimated synchronous reference frame is used to estimate the rotor position. In this paper, the relationship between the high frequency voltages and high frequency currents is modeled using the voltage equations at the high frequency. Even under heavy load conditions, the proposed technique makes it possible to drive the SMPM motor in the low speed region including standstill.

A key advantage of the methods based on the magnetic saliencies is that the estimation accuracy does not rely on the rotor speed, specifically at zero speed operation. Also, the methods are less sensitive or completely insensitive to the parameter variations of the motor. Yet, the techniques do not work well in the high speed regions due to the effect of back EMF.

3.4 Starting Techniques

A common problem associated with sensorless PMAC motors is the starting procedure. In PMAC motors, conventionally there is no information on the rotor position before starting. Therefore, the starting from an unknown rotor position may be accompanied by a temporary reverse rotation or may cause a starting failure. These are not tolerable in various applications. Thus, when the initial rotor position information is not available, a proper starting procedure must be implemented for safe startup. In the literature, a number of techniques have been developed to start PMAC motors.

Most of the starting techniques proposed for sensorless trapezoidal PMAC motor drives were based on an open loop control [36, 82] or arbitrarily exciting the stator windings and aligning the rotor to a certain position [41]. In [36], synchronous gate signals generated from the computer in an open loop control mode excite the motor phases through the inverter where the frequency of these signals is increased from zero. Then, when the motor back EMF is sufficient to determine the rotor position using the terminal voltages, the open loop mode is changed to the sensorless control mode for the

trapezoidal PMAC motor. Another starting method excites two arbitrary phases for a preset time period [41]. At the time, the current limiter limits the motor line currents. When the rotor rotates to the direction corresponding to the excited phase due to the arbitrary excitation, the commutation command advancing the switching pattern by 120° is provided. Then, the open loop control is immediately transformed to the sensorless drive proposed in the paper.

In sinusoidal PMAC motors, similar starting schemes with an open loop mode were proposed [42, 62]. In [42], a ramp speed command was forced to accelerate the motor from standstill to the speed at which a reliable flux linkage angle was able to be determined. In [62], a specific PWM pattern to the inverter was applied to move the rotor of the motor for about 200 μs. When the rotor was aligned in the direction of the U-phase winding by several applications of the specific PWM pattern, the open loop drive was switched to the sensorless control proposed in the literature.

The open-loop strategies described above have poor dynamic response and the rotor may be in the hunting mode. The techniques can not give position information at standstill. In addition, if the electrical drive system has been switched off, it is not possible to know the actual rotor position in one period with respect to the stator phases. When smooth starting is required as in various applications, an arbitrary switching may not lead to smooth starting in the right direction.

The initial rotor position can be estimated based on utilizing magnetic saliencies due to either geometric construction or saturation effects. In order to estimate the rotor position at standstill, the methods which detect saliencies can be categorized into two groups depending on the fundamental excitation of the machine [65-67] as shown in Chapter 3.3.4 or a separate excitation from the fundamental excitation [68, 70-81, 83-89, 93, 94].

In the separate excitation group, two basic methods to estimate the rotor position at standstill are pulse signal injection [68, 70, 83-87] or sinusoidal carrier signal injection [71-81, 88-94]. In order to determine the initial rotor position involving both the location and the direction of the rotor magnet in an IPM motor, saturation effects of the iron bridges between the rotor magnets were utilized at no load [83]. In the reference, suitable short voltage pulses were applied to the motor winding and the resulting currents were measured to estimate the inductance which gave information on the

location of the d- and q- axis. The measured currents had specific patterns with respect to the rotor position due to the iron saturation. Therefore, the location and the direction of the d-axis were detected by utilizing the specific current patterns. The advantage of the method is that it allows detection of the rotor position without any rotation and that no additional hardware to measure voltages is required. However, the algorithm must be tuned for the motor and drive.

In [84], a sensorless method was proposed to detect the initial rotor position in a wide range of PM motors (isotropic and nonisotropic, brushless DC motors and PM synchronous motors) by utilizing the inductance variation due to the rotor position and the stator currents. In this algorithm, a sequence of voltage pulses was injected to the motor windings at standstill and the peak values of the resulting currents were evaluated to obtain the initial rotor position. In particular, an iterative sequence of voltage pulses was combined with a fuzzy logic processing of the current responses to improve the accuracy of the estimated position. This method is able to remove the temporary reverse rotation of the motor at start-up and prevent starting failures. Also, knowledge of the motor parameters is not required in the algorithm.

For a non-salient PM synchronous motor, a technique was based on the saturation effect of the stator iron to obtain the rotor position at standstill in [85]. To saturate the stator iron partially, short voltage pulses were injected to the stator windings at standstill in the method. Also, the change in current of each phase was measured during each pulse and the rate of change of the stator winding current was utilized to distinguish between a north magnet pole and a south magnet pole, which was a function of the inductance variation, the iron saturation, and the flux due to the magnet position. This scheme is robust due to the use of a ratio of differences of current values in the position estimation. The method does not require the knowledge of any of the motor parameters. In addition, the calculations require no trigonometric or inverse functions

In [86], an initial rotor position estimation technique was based on the winding inductance variation with the rotor position in a salient-pole brushless PM motor. In the paper, two types of pilot voltage pulses supplied from an inverter were applied to the motor windings where the pilot voltages had rectangular DC voltage pulses with different duty-cycles. Then, the resultant current peaks were measured by current sensors to be utilized in the rotor position estimation at standstill. However, the method

may cause temporary reverse rotation of the motor from starting at standstill since the armature current due to the applied pilot DC voltage pulses generates a small torque.

In order to obtain the rotor position at standstill in a brushless DC motor, the saturation effect of the stator iron was detected by using short current pulses in [87]. The sign and the amplitude of the current waveform are detected while two phases are excited. After a short time, the current is reversed, and the sign and the amplitude are again determined. If the current difference sign is positive, the PM flux has the same sign as the flux created by the positive current. If the difference sign is negative, the PM flux has the same sign as the current produced by the negative current. The process is repeated for other phases. The information obtained is used to determine the rotor position. However, the excitation current pulses may generate a torque to rotate the motor, which may move the initial rotor position. In addition, the method depends on the accuracy of the measurements.

In order to estimate the initial rotor position, the sinusoidal carrier injection methods based on the magnetic saliencies are divided into two categories; current injection techniques [71, 88] and voltage injection methods [72-81, 89-94]. Here, voltage injection studies are also categorized into rotating [72-76, 89-92] and fluctuating excitation methods [77-81, 93, 94]. A sensorless method for a salient-pole brushless DC motor was proposed in [88]. In the method, the initial position angle at a standstill was estimated by utilizing the voltages induced by injecting sinusoidal currents with small amplitude to the motor windings. In addition, the polarity detection was based on the flux saturation effects. This method was able to estimate the initial rotor position without the vibration and the rotation of the rotor shaft.

The rotating high frequency voltage injection methods are applied to the motor winding to estimate the initial rotor position by using the magnetic saliencies in [72-76, 89-92]. In [89], a method utilized the magnetic saliency and the orientation of the current vector locus to obtain the initial rotor position in a salient pole PMSM without rotor rotation. When balanced 3-phase sinusoidal AC voltages were applied to the armature of the IPM motor by a PWM inverter at standstill, the locus of the armature current vector became an oval on the d-q plane due to the magnetic saliency of the motor. The major diameter of the current vector oval gave information on the rotor magnet direction. In addition, the high frequency AC voltage signal was applied to make the generated torque of the motor small, hence avoiding the motor rotation due to

the injected signal. However, the test results were obtained with an off-line estimation system.

A high frequency rotating voltage injection method was applied for sensorless Direct Torque Control (DTC) of an Interior Permanent Magnet Synchronous Motor (IPMSM) drive at very low speeds and at standstill as reported in [90-92]. In order to obtain the rotor position and speed estimation of the IPMSM at the extremely low speed regions in [90-92], a carrier excitation signal was superimposed on the d-component of the stator voltage in the estimated rotor reference frame. Then, a current response was detected in the q-direction of the estimated rotor reference frame. The q-component measured current was band-pass filtered to obtain the high frequency q-component of detected current. Next, the high frequency current was demodulated and filtered by a low-pass filter (LPF) to obtain a signal, which is proportional to the position estimation error. Finally, a PI regulator, which was cascaded with an integrator, was used to force the error to zero and to obtain the position estimation on a phase-locked loop (PLL). It was shown that the high frequency injection method is able to provide a reliable solution at very low speeds. However, its performance decreases dramatically as the speed increases. Therefore, the other forms of observers such as a sliding mode observer as reported in [92] have to be utilized at medium to high speeds with a smooth changeover algorithm for the direct torque controlled sensorless position detection technique.

A high frequency pulsating voltage vector [77-81, 93, 94] in the estimated synchronous frame is injected into an IPM machine [77-79, 93, 94] and an SMPM motor [80, 81] for the initial position estimation. A sensorless initial rotor position detection scheme was proposed based on a high frequency pulsating voltage injection in an IPM motor drive [78]. When the high frequency pulsating signal was injected in the d-axis of the IPM motor, the injected signal was distorted due to the hysteresis phenomenon and then the distorted waveform contained even-order harmonics. In particular, the second-order harmonics were utilized effectively to detect the north magnetic pole position in the method. This algorithm had fast dynamics due to the use of the high frequency injection signal.

In an IPM synchronous motor, a rotating or pulsating voltage carrier vector was injected to estimate the initial rotor position including the polarity of the rotor magnet at standstill in [93]. In the paper, the IPM synchronous motor was modelled taking into account magnetic saturation for both signal injection types. In addition, the paper

proposed three observers based on tracking spatial and saturation saliencies. Two spatial saliency tracking observers using rotating and pulsating high-frequency voltage signal injection were employed for the IPM synchronous machine. However, an observer to track the saturation saliency using rotating voltage high-frequency carrier injection was able to be applied to both the IPM synchronous motor (salient pole) and the surface-mounted PM synchronous motor (nonsalient pole). In [93], robust and fast initial rotor position and polarity estimation without shaft rotation was guaranteed by the proposed tracking estimators.

In order to estimate the rotor position and to distinguish the polarity of the rotor magnet at standstill, a technique was based on injecting a carrier-frequency signal using either a rotating voltage vector in the stationary reference frame or an oscillating voltage vector in the estimated rotor reference frame for an IPM synchronous motor in [94]. In the reference, the saturation effect of the d-axis flux linkage was modelled in the d-axis rotor reference frame by a Taylor series to track the north pole of the rotor magnet. A heterodyning process was also utilized to extract the magnetic polarity and the position information. The rotor position was estimated by using a Luenberger style observer in the paper. However, an accurate saturation model was required to improve the convergence speed of the polarity estimation.

When injected signals are involved to detect the rotor position, it is important to bear in mind that they will always produce a torque component that might be unwanted. However, if the current in the q axis is kept small, the unwanted torque is also kept small.

3.5 Conclusions

The sensorless control strategy for trapezoidal PMAC motors is simpler than the strategies used for sinusoidal PMAC motors. In the control of three-phase brushless DC motors (BLDC motors) with trapezoidal back EMF voltages (with a flat top of 120 degrees electrical), only two of the three winding phases are excited at any moment. Consequently, the back EMF induced in the unexcited winding can be used to produce a switching sequence to drive power devices in the inverter to provide current commutation. Usually, the power devices are commutated every 60 degrees sequentially to synchronize the excitation currents with the back EMF voltages according to the rotor angle. However, all phase windings need to be excited at any instant in PM synchronous

motors (PMSMs or sinusoidal PMAC motors) with sinusoidal back EMF voltages. Therefore, the sinusoidal PMAC motors require sinusoidal phase currents synchronized with the back EMF voltages to produce a constant electromagnetic torque, which need continuous rotor position data, which is complex to obtain and is expensive to implement.

This chapter provided a comprehensive literature review of sensorless position estimation methods for PMAC motors to obtain the rotor position. In trapezoidal PMAC motors, the rotor position was primarily determined using the back EMF waveform, using the third harmonic or detecting the conducting states of freewheeling diodes of the inverter in the unexcited phase. In particular, the back EMF approaches have been most commonly employed to determine the switching instants. However, all these schemes have limitations at very low speeds including starting from standstill due to the magnitude of back EMF being too small to be sensed. Therefore, such techniques need special starting methods to overcome this limitation, which was also surveyed.

In order to obtain the rotor position data, motor circuit parameters and measurements of terminal voltages and winding currents have been utilized in various position estimation methods based on state observers, Kalman filters and the estimated flux linkages. However, such techniques are complicated and require high resolution, fast and expensive processors. In addition, the accuracy of these techniques heavily depends on the accuracy of the measurements of the currents or terminal voltages, and they are sensitive to major parameter variations. In addition, they have limited performance at low speeds due to integration drift.

The magnetic saliencies due to geometric construction and saturation effects have been utilized to estimate the rotor position in a number of position detection methods in interior PM motors (salient pole PMAC motors) and surface-mounted PM motors (non-salient pole PMAC motors). These are primarily based on the inductance variations in the motor. Although some methods have not utilized signal injection to track the inductance variation which is related to the rotor position, various sensorless methods have employed signal injection schemes involving pulses or sinusoidal signals to detect the magnetic saliencies of salient or non-salient pole PMAC motors. It was shown that these techniques can estimate the rotor position even at low speeds including starting from standstill, and they are less sensitive to the motor parameter variations. However, they are affected by the load due to saturation at higher loads. In addition, they are

affected by the magnetic coupling between d- and q-axis. Furthermore, at high speeds, they have a limited performance due to the back EMF.

In summary, a number of techniques have been developed to estimate the rotor position without using a position sensor for PMAC motors. However, most of the developed sensorless methods have been employed for conventional PMAC motors, and not for the fault-tolerant PMAC motor drives with magnetic, electrical and thermal isolation between the motor phases. Although one paper was identified that investigated the position estimation techniques in a fault-tolerant motor drive, it has limitations; it fails at low speeds due to integration drift, is sensitive to the motor parameter variations, and has not been applied to the fault-tolerant PMAC motor drive with redundancy utilized in this research.

Therefore, it can be concluded that the previous techniques are not directly applicable to the fault-tolerant PMAC motor drive with redundancy that is considered in the thesis. In addition, most of the previous methods have not considered faults that may occur in a motor drive and cannot provide redundant rotor position information. This is detrimental to improving the reliability of the motor drive. Therefore, this thesis aims to develop a sensorless position estimation technique to estimate the rotor position to increase the reliability and to offer redundancy for the rotor position information in a fault-tolerant PMAC motor drive.

4. Mathematical Modeling and Simulation of the Motor Drive

4.1 Introduction

In Chapter 2, the fault-tolerant PMAC motor drive with redundancy utilized in this study and its basic control structure were briefly explained to provide the fundamentals of the motor drive system. The motor drive contained two identical motor modules on a common rotor and three H-bridge inverters powered from a separate dc supply per motor module. Unlike conventional PMAC motors, each motor module has fault-tolerant features due to its modified design to offer electrical, magnetic and thermal isolation between phases to prevent propagation of failures in phases in the case of a fault.

One of the objectives of this chapter is to develop a mathematical model to be able to simulate and study the behaviour of the fault-tolerant three-phase surface-mounted sinusoidal PMAC motor drive, which also has redundancy. The modelling is divided into two main parts: the fault-tolerant three-phase surface-mounted sinusoidal PMAC motors and the current control methodology. The abc stator reference frame is considered in the motor model and each fault-tolerant PMAC motor is modelled by the voltage equations, the electromagnetic torque equations and the motion equations. It can be noted here that the voltage equations given in this chapter will be also employed in the sensorless position estimation methods that will be explained in Chapter 5.

The chapter aims to develop a computer simulation model to study the steady state and the dynamic performance of the entire fault-tolerant PMAC motor drive with redundancy. In the simulations, the Simulink programming environment is used to develop the drive simulation. In order to validate the effectiveness of the developed simulation models, various simulation results are demonstrated under a range of operating conditions including starting from standstill.

4.2 Modeling of the Fault-Tolerant Three-Phase PMAC Motors with Redundancy

As stated earlier, the fault-tolerant PMAC motor with redundancy utilized in this research consists of two identical fault-tolerant three-phase surface-mounted sinusoidal PMAC motors on a common shaft. To obtain the mathematical model, several assumptions were made:

1. Saturation is neglected although it can be taken into account by parameter changes.
2. The back EMF voltages are assumed as ideal sinusoidal waveforms.
3. The mutual inductances are equal to zero since the mutual inductances between phases are negligibly small due to magnetic isolation between phases of the fault-tolerant PMAC motor drive with concentrated windings.
4. The self inductance of each phase winding is independent of rotor position.
5. Eddy current and hysteresis losses are neglected.

The electrical equivalent circuit considered for the fault-tolerant motor drive is given in Figure 4.1. Each phase winding in the motor is modeled by a series electrical circuit including a resistance, a self inductance and a back EMF voltage. Therefore, the voltage equations for the motor can be presented in the abc reference frame as

$$\begin{bmatrix} v_a \\ v_b \\ v_c \\ v_u \\ v_v \\ v_w \end{bmatrix} = \begin{bmatrix} R & 0 & 0 & 0 & 0 & 0 \\ 0 & R & 0 & 0 & 0 & 0 \\ 0 & 0 & R & 0 & 0 & 0 \\ 0 & 0 & 0 & R & 0 & 0 \\ 0 & 0 & 0 & 0 & R & 0 \\ 0 & 0 & 0 & 0 & 0 & R \end{bmatrix} \begin{bmatrix} i_a \\ i_b \\ i_c \\ i_u \\ i_v \\ i_w \end{bmatrix} + \begin{bmatrix} L & 0 & 0 & 0 & 0 & 0 \\ 0 & L & 0 & 0 & 0 & 0 \\ 0 & 0 & L & 0 & 0 & 0 \\ 0 & 0 & 0 & L & 0 & 0 \\ 0 & 0 & 0 & 0 & L & 0 \\ 0 & 0 & 0 & 0 & 0 & L \end{bmatrix} \frac{d}{dt} \begin{bmatrix} i_a \\ i_b \\ i_c \\ i_u \\ i_v \\ i_w \end{bmatrix} + \begin{bmatrix} e_a \\ e_b \\ e_c \\ e_u \\ e_v \\ e_w \end{bmatrix} \tag{4.1}$$

where L represents the constant value of the self inductances of the phases, R represents the phase resistances, v_a, v_b, v_c, v_u, v_v and v_w are the phase voltages, i_a, i_b, i_c, i_u, i_v and i_w are the phase currents and e_a, e_b, e_c, e_u, e_v and e_w represent the back EMF voltages of each phase. Note that the subscripts a, b and c are for the motor module 1 and u, v and w are for the module 2. Note that the phase back EMF voltages

induced in the stator coils are due to permanent magnet fluxes crossing the air gap that are the rates of change of flux linkages due to permanent magnets mounted on the rotor.

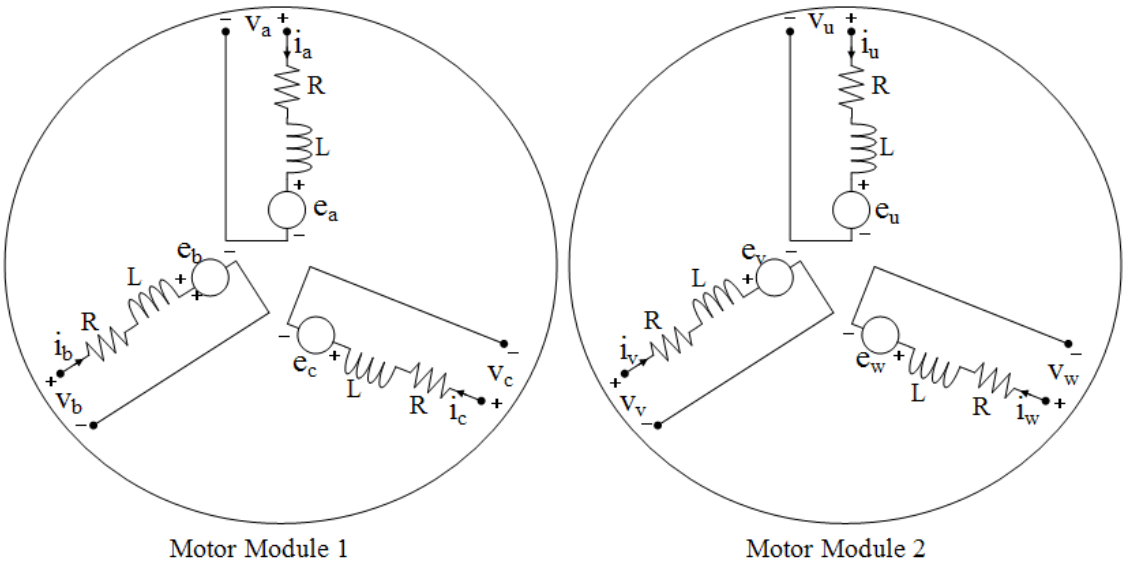

Figure 4.1 The equivalent circuit of the fault-tolerant three-phase surface-mounted sinusoidal PMAC motor with redundancy

To be utilized in the simulation study, the voltage equations given above can be rearranged as

$$\frac{d}{dt}\begin{bmatrix} i_a \\ i_b \\ i_c \\ i_u \\ i_v \\ i_w \end{bmatrix} = \frac{1}{L}\left\{\begin{bmatrix} v_a \\ v_b \\ v_c \\ v_u \\ v_v \\ v_w \end{bmatrix} - \begin{bmatrix} e_a \\ e_b \\ e_c \\ e_u \\ e_v \\ e_w \end{bmatrix} - \begin{bmatrix} R & 0 & 0 & 0 & 0 & 0 \\ 0 & R & 0 & 0 & 0 & 0 \\ 0 & 0 & R & 0 & 0 & 0 \\ 0 & 0 & 0 & R & 0 & 0 \\ 0 & 0 & 0 & 0 & R & 0 \\ 0 & 0 & 0 & 0 & 0 & R \end{bmatrix}\begin{bmatrix} i_a \\ i_b \\ i_c \\ i_u \\ i_v \\ i_w \end{bmatrix}\right\} \tag{4.2}$$

In the fault-tolerant PM motor drive considered in this research, the back EMF voltages have sinusoidal waveforms and their magnitude is directly proportional to the speed of the rotor. The phase back EMF waveforms are out of phase with the adjacent phases by $2\pi/3$ radians in each motor module, but they are in phase between the corresponding phases of the two motor modules. Consequently, the phase back EMF voltages in the stator windings can be written as below.

$$\begin{bmatrix} e_a \\ e_b \\ e_c \\ e_u \\ e_v \\ e_w \end{bmatrix} = k_e \omega_r \begin{bmatrix} \sin(\theta) \\ \sin(\theta - \frac{2\pi}{3}) \\ \sin(\theta - \frac{4\pi}{3}) \\ \sin(\theta) \\ \sin(\theta - \frac{2\pi}{3}) \\ \sin(\theta - \frac{4\pi}{3}) \end{bmatrix} = k_e \omega_r \begin{bmatrix} e_1(\theta) \\ e_2(\theta) \\ e_3(\theta) \\ e_4(\theta) \\ e_5(\theta) \\ e_6(\theta) \end{bmatrix} \tag{4.3}$$

Here, k_e is the back EMF constant, ω_r is the mechanical angular speed of the rotor, and $e_1(\theta)$, $e_2(\theta)$, $e_3(\theta)$, $e_4(\theta)$, $e_5(\theta)$ and $e_6(\theta)$ are defined as the phase back EMF functions for corresponding phases in the motor modules 1 and 2. The back EMF functions are sinusoidal with unity magnitudes.

The mechanical rotor speed in equation (4.3) is given by

$$\omega_r = \frac{d\theta_r}{dt} \tag{4.4}$$

where θ_r is the mechanical rotor position in rad and it is related to the electrical rotor angle θ as

$$\theta_r = \frac{\theta}{p} \tag{4.5}$$

where p is the number of pole pairs.

Combining the equations (4.4), (4.5) and (4.3), the phase back EMF voltages can be given by

$$\begin{bmatrix} e_a \\ e_b \\ e_c \\ e_u \\ e_v \\ e_w \end{bmatrix} = \frac{k_e}{p} \cdot \frac{d\theta}{dt} \begin{bmatrix} e_1(\theta) \\ e_2(\theta) \\ e_3(\theta) \\ e_4(\theta) \\ e_5(\theta) \\ e_6(\theta) \end{bmatrix} \tag{4.6}$$

Finally by substituting (4.6) into (4.1), the phase voltage equations of the motor can be given as below, which is also utilized in the proposed sensorless position estimation algorithms as will be explained in Chapter 5.

$$\begin{bmatrix} v_a \\ v_b \\ v_c \\ v_u \\ v_v \\ v_w \end{bmatrix} = \begin{bmatrix} R & 0 & 0 & 0 & 0 & 0 \\ 0 & R & 0 & 0 & 0 & 0 \\ 0 & 0 & R & 0 & 0 & 0 \\ 0 & 0 & 0 & R & 0 & 0 \\ 0 & 0 & 0 & 0 & R & 0 \\ 0 & 0 & 0 & 0 & 0 & R \end{bmatrix} \begin{bmatrix} i_a \\ i_b \\ i_c \\ i_u \\ i_v \\ i_w \end{bmatrix} + \begin{bmatrix} L & 0 & 0 & 0 & 0 & 0 \\ 0 & L & 0 & 0 & 0 & 0 \\ 0 & 0 & L & 0 & 0 & 0 \\ 0 & 0 & 0 & L & 0 & 0 \\ 0 & 0 & 0 & 0 & L & 0 \\ 0 & 0 & 0 & 0 & 0 & L \end{bmatrix} \frac{d}{dt} \begin{bmatrix} i_a \\ i_b \\ i_c \\ i_u \\ i_v \\ i_w \end{bmatrix} + \frac{k_e}{p} \cdot \frac{d\theta}{dt} \begin{bmatrix} e_1(\theta) \\ e_2(\theta) \\ e_3(\theta) \\ e_4(\theta) \\ e_5(\theta) \\ e_6(\theta) \end{bmatrix} \tag{4.7}$$

The equation of motion for the motor drive can be given by

$$T_e - T_l = J \frac{d\omega_r}{dt} + B\omega_r \tag{4.8}$$

where T_e is the net electromagnetic torque of the PM motor drive, T_l is the load torque, J is the inertia of the motor and connected load, and B is the damping coefficient of the motor and mechanical load. In the simulation study, it is assumed that the damping coefficient is negligibly small and hence is assumed to be zero.

The above equation is usually rearranged in a state-space form that is suitable for the computer simulation.

$$\frac{d\omega_r}{dt} = \frac{1}{J}\left(T_e - T_l\right) \tag{4.9}$$

The total electromagnetic torque of the fault-tolerant motor drive is given as [93]

$$\begin{aligned} T_e &= T_{e1} + T_{e2} = T_{ea} + T_{eb} + T_{ec} + T_{eu} + T_{ev} + T_{ew} \\ &= \frac{1}{\omega_r}(e_a i_a + e_b i_b + e_c i_c + e_u i_u + e_v i_v + e_w i_w) \end{aligned} \tag{4.10}$$

where T_e is the total electromagnetic torque, T_{e1}, T_{e2} are the electromagnetic torques generated by the motor modules 1 and 2, and T_{ea}, T_{eb}, T_{ec}, T_{eu}, T_{ev} and T_{ew} are the electromagnetic torques generated by each phase.

It should be noted that the electromagnetic torque value calculated from (4.10) can be significantly inaccurate specifically near zero speed or very low speed regions since the electromagnetic torque is inversely proportional to the rotor speed. Therefore, to avoid large errors, the electromagnetic torque is calculated by

$$T_e = k_e\left\{e_1(\theta)\cdot i_a + e_2(\theta)\cdot i_b + e_3(\theta)\cdot i_c + e_4(\theta)\cdot i_u + e_5(\theta)\cdot i_v + e_6(\theta)\cdot i_w\right\} \tag{4.11}$$

where the rotor speed is not included.

4.3 Simulation of the Fault-Tolerant Motor Drive

To study the performance of the fault-tolerant three-phase PMAC motor drive with redundancy under steady state and dynamic operating conditions, Simulink™ was used as a simulation tool. With the graphical user interface (GUI) of Simulink, the motor drive was modelled with block diagrams containing separate tasks.

4.3.1 Simulink Model for the Steady State Operation

Figure 4.2 presents a Simulink model to simulate the steady state performance of the motor drive which consists of two identical three-phase motor modules. The input of the motor drive system is the torque command (I_m) which is equal to the amplitude of the current command. The output of the drive system is the total electromagnetic torque which is obtained by summing the per phase electromagnetic torques. In the simulation, the mechanical rotor position is obtained by integration of the mechanical rotor speed utilizing an integrator in Block C.

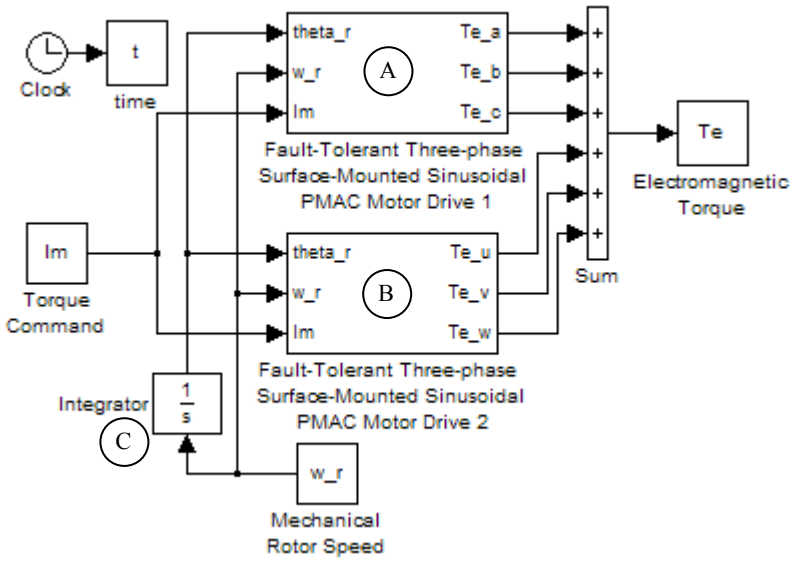

Figure 4.2 A Simulink model of the torque control of the fault-tolerant motor drive with redundancy for steady-state operation

Figure 4.3a shows the complete Simulink block diagram for one motor module, which consists of the back EMF generator, the hysteresis current controllers and the reference current generators. Note that the generated back EMFs are also utilized to estimate the electromagnetic torques.

Each single phase drive in the simulation model consists of four sub-components involving a sinusoidal reference current generator, a hysteresis current regulated H-bridge inverter, a series electrical circuit including a phase resistance, a phase self inductance and a phase back EMF voltage and an electromagnetic torque estimator as illustrated in a schematic block diagram in Figure 4.3b. The sinusoidal reference current generator in Block E generates a reference sinusoidal phase current utilizing the current command and the rotor position as described in equation (2.1).

The hysteresis current controller (Block F in the figure) forces the actual phase current to follow the reference phase current within the hysteresis bandwidth determined by the hysteresis comparator. This is done by controlling the inverter switches as described earlier in Section 2.4.1. In normal conditions, the output of the hysteresis current regulated H-inverter is the phase voltage that swings between the positive dc input supply voltage (V_{dc}) and the negative dc input voltage ($-V_{dc}$). However, if the actual phase current is zero under specific conditions such as a winding open-circuit failure, the phase voltage is equal to the phase back EMF voltage.

The phase voltage, the output of Block F, is applied to the phase winding, and the corresponding phase current is generated in Block G by integrating the derivative of phase current utilizing an integrator. The initial value of the current is defined in the integrator block.

The instantaneous phase current, the phase back EMF voltage, and the mechanical rotor speed are used to estimate the electromagnetic torque of a single phase in Block H. However, when the mechanical rotor speed is zero, the initial phase electromagnetic torques of the entire motor drive are assumed to be equal to

$$\begin{bmatrix} T_{ea} \\ T_{eb} \\ T_{ec} \\ T_{eu} \\ T_{ev} \\ T_{ew} \end{bmatrix} = \begin{bmatrix} 0 \\ -i_b k_e \\ i_c k_e \\ 0 \\ 0 \\ 0 \end{bmatrix} \tag{4.12}$$

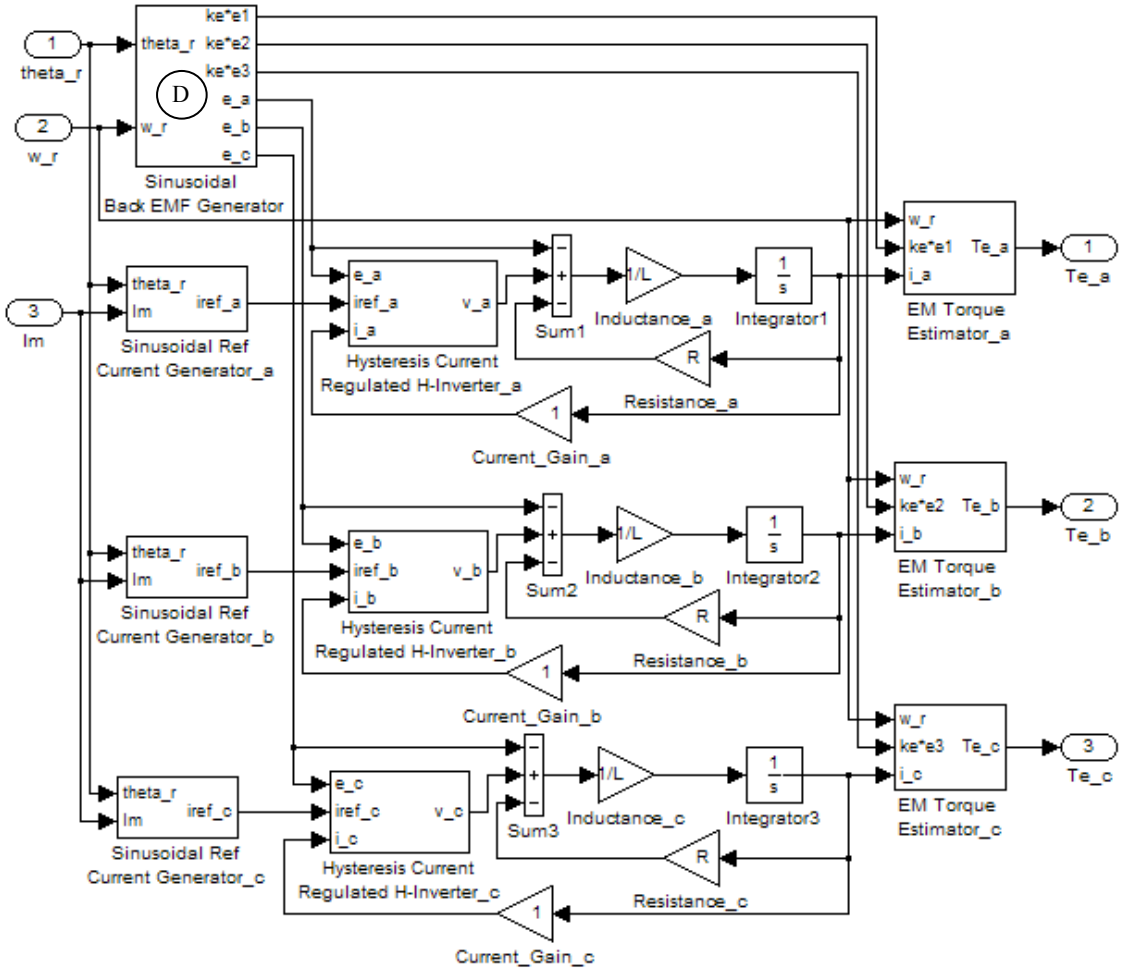

(a)

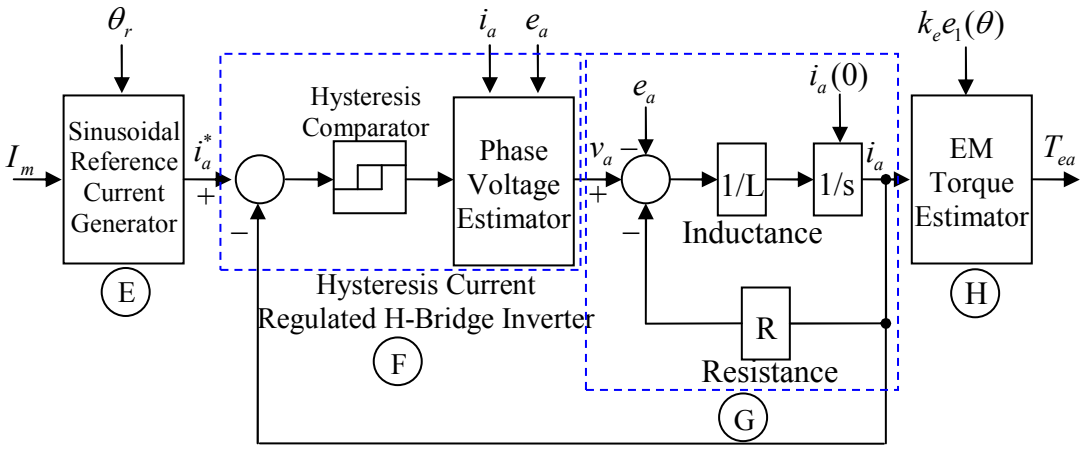

(b)

Figure 4.3 (a) A Simulink model of the fault-tolerant three-phase surface-mounted sinusoidal PMAC motor drive 1, (b) a schematic block diagram of one phase of the drive.

4.3.2 Simulation Model for the Dynamic State Operations

Figure 4.4 shows a schematic block diagram and a Simulink block model of the entire motor drive that is used to study the performance of the drive under dynamic operating conditions. The Blocks I and J in Figure 4.4a contain the dual three-phase fault-tolerant PM motor drive modules as described in Section 4.3.1. This simulation model incorporates the equation of motion and an integrator to estimate the rotor position under dynamic conditions. As illustrated before, the electromagnetic torque command is defined by the amplitude of the current command.

The equation (4.9) given earlier is implemented in Block K. As shown in this block, the total electromagnetic torque is applied to the rotor connected to a load, which rotates at mechanical speed ω_r. The mechanical rotor position can be obtained by integration of the mechanical rotor speed and its initial value can be set to a constant value. As given previously in equation (4.5), the electrical rotor position is obtained by the product of the mechanical rotor position and the number of pole pairs of the motor.

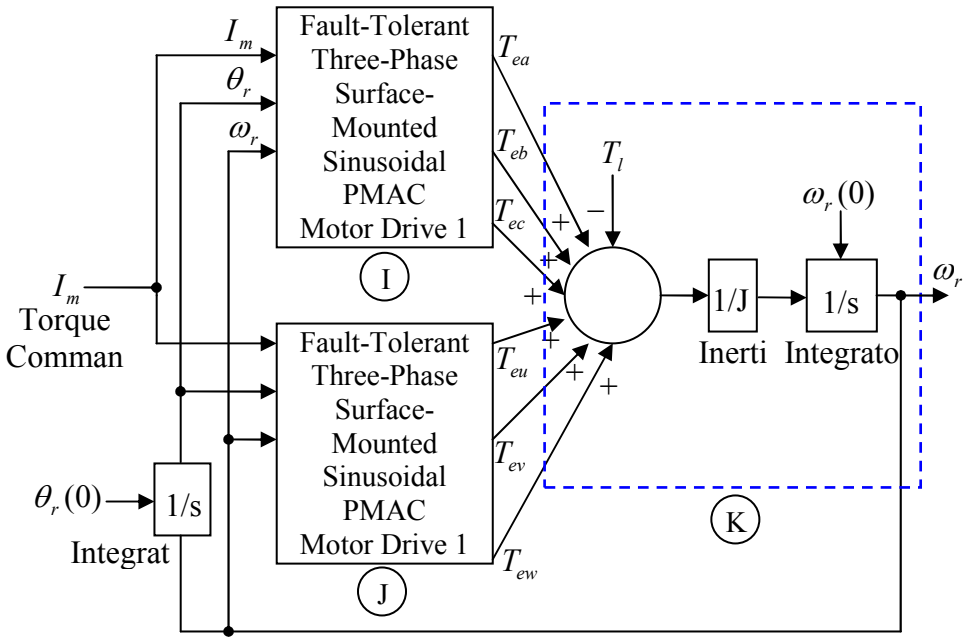

(a)

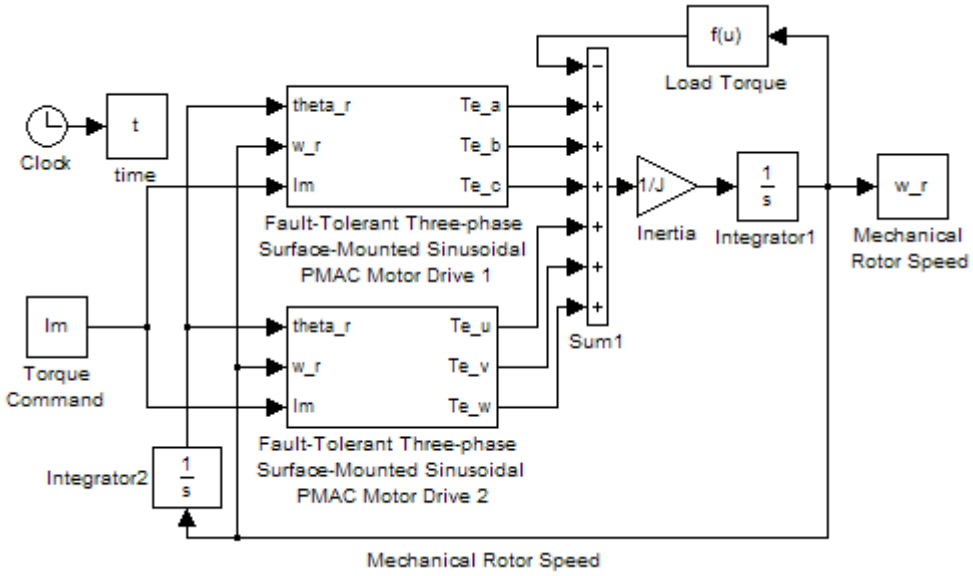

(b)

Figure 4.4 The dynamic model of the entire drive (a) schematic block diagram, (b) Simulink model

4.4 Simulation Results

In this section, various simulation results obtained under both steady-state and dynamic operating conditions are presented to confirm the validity of the developed simulation model. In the simulation results for the steady state operation, the phase A current, the

phase A voltage, the phase A electromagnetic torque and the total electromagnetic torque in the motor module 1 are illustrated. The mechanical rotor speed and the electrical rotor position are included only during the dynamic state operation.

The parameters of the motor modules are given in Table 4.1. In the simulation results presented, the simulation time step was set to 10 μs and ode4 (Runge-Kutta) solver was utilized in the integration process.

Table 4.1 Parameters of the motor modules used in the simulation studies

Parameters	Value
Moment of inertia (J)	0.0004 kgm^2
Number of pole pairs, (p)	2
Winding resistance, (R)	0.87 Ω
Winding inductance, (L)	2.1 mH
Back EMF constant, (k_e)	0.093 V/rad/s

4.4.1 Steady State Results

Figure 4.5 shows a set of simulation results obtained under steady-state low speed operation of the motor drive. In this operating mode, the DC input voltage (V_{dc}) of the H-bridge inverter was 20V, the hysteresis band (Δh) was 0.6A, the torque command (I_m) was 3.5A, the mechanical rotor speed (ω_r) was 31.4rad/s and there was no phase advance or delay.

In Figure 4.5, the instantaneous waveforms of the phase current (i_a), phase voltage (v_a), phase electromagnetic torque (T_{ea}) obtained in phase A of the fault-tolerant motor module 1, the electromagnetic torque (T_{e1}) of the fault-tolerant motor module 1 are illustrated from top to bottom. A sinusoidal current waveform with the band of 0.6A was obtained in this simulation result. Note that the torque produced from phase A in the motor module 1 has a near sinusoidal waveform and the total electromagnetic torque obtained from the motor module 1 is relatively constant (with small torque ripples) since it includes the torques of all three phases in the motor module 1.

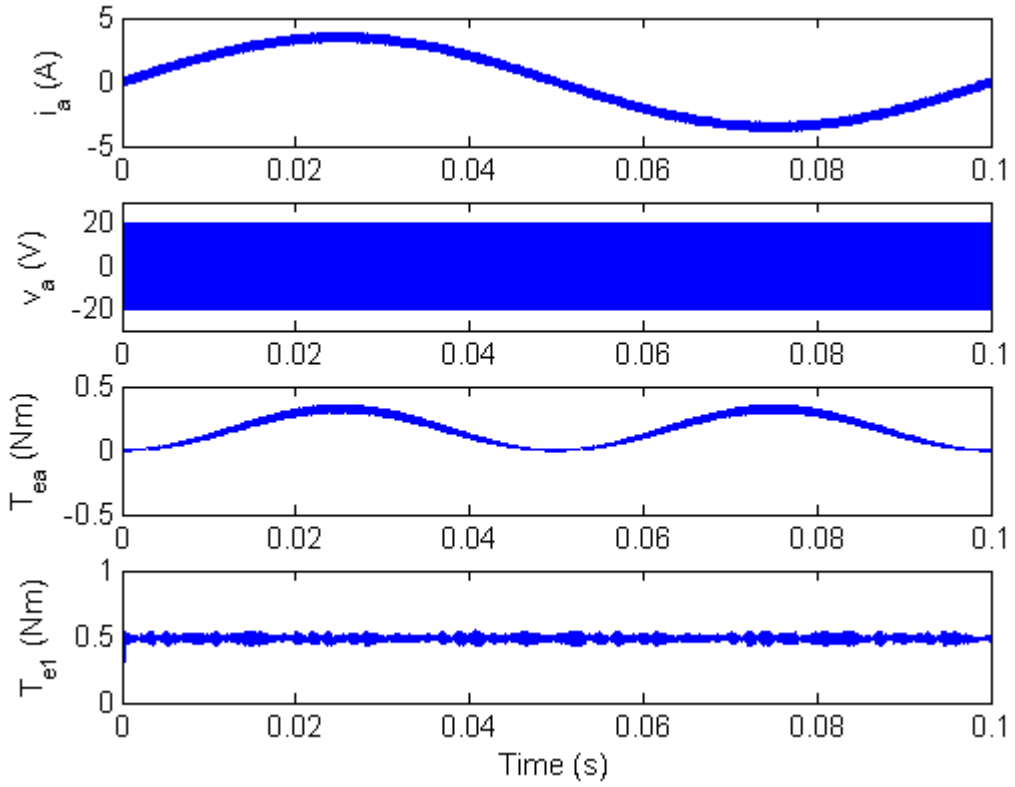

Figure 4.5 Simulation results of the motor drive under a steady-state mechanical rotor speed of 31.4rad/s with no phase advance or delay angle.

In Figure 4.6, a second set of simulation results is provided to demonstrate constant high-speed operation in the simulated motor drive. In this test, the rotor speed was 219.8 rad/s, and all of the other parameters were kept same as the previous test. Note that the top graph in the figure includes a dashed red line which indicates the sinusoidal reference phase current. It can be highlighted here that since the amplitude of the back-EMF voltage is proportional to the rotor speed in the PMAC motor, the effective voltage across the motor phase winding, which is the difference between the DC input voltage of the inverter and the back EMF of a corresponding phase, becomes insufficient at high speeds. At such speeds, the phase current is limited by the effective voltage and hence cannot follow the reference current. Therefore, no current control is achieved within these regions. As shown in the results, the phase current ripple increases which results in larger torque ripple.

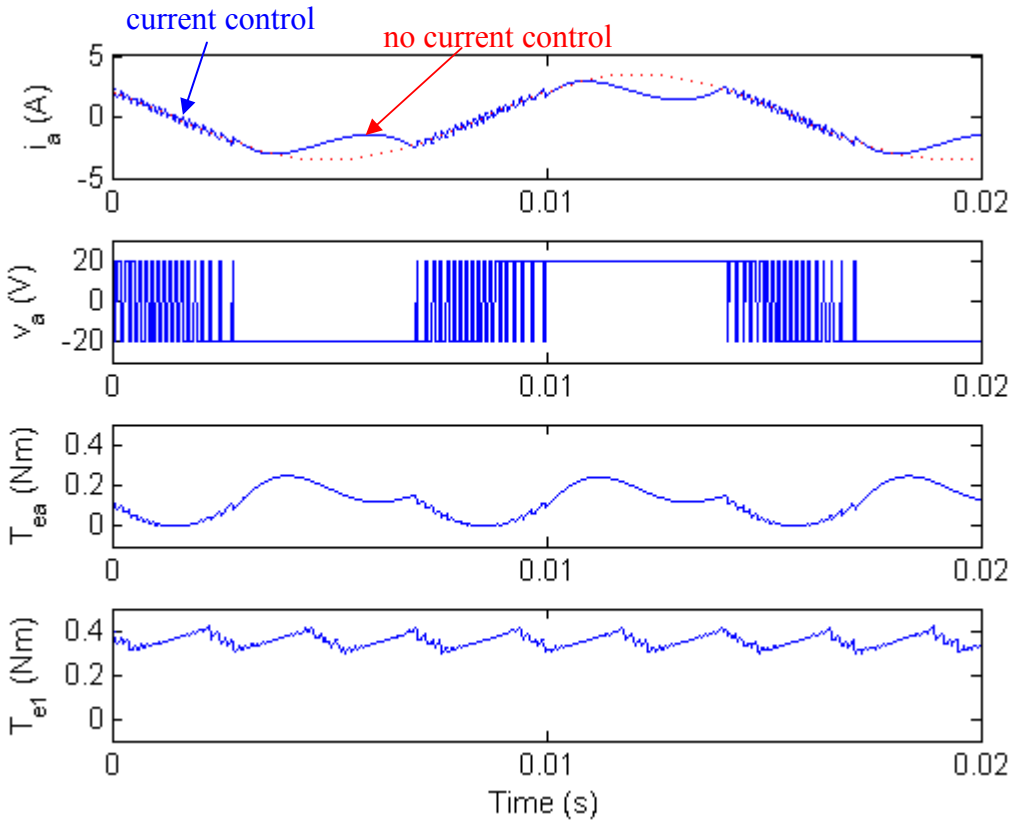

Figure 4.6 Simulation results of the fault-tolerant three-phase surface-mounted sinusoidal PMAC motor drive with redundancy under a steady-state constant mechanical rotor speed of 219.8 rad/s with no phase advance or delay angle

Figure 4.7 is given to demonstrate the operation of the motor under a phase advance angle of $\pi/4$ rad. As it can be seen in the figure, this mode of operation reduces the current distortion as well as the torque ripple.

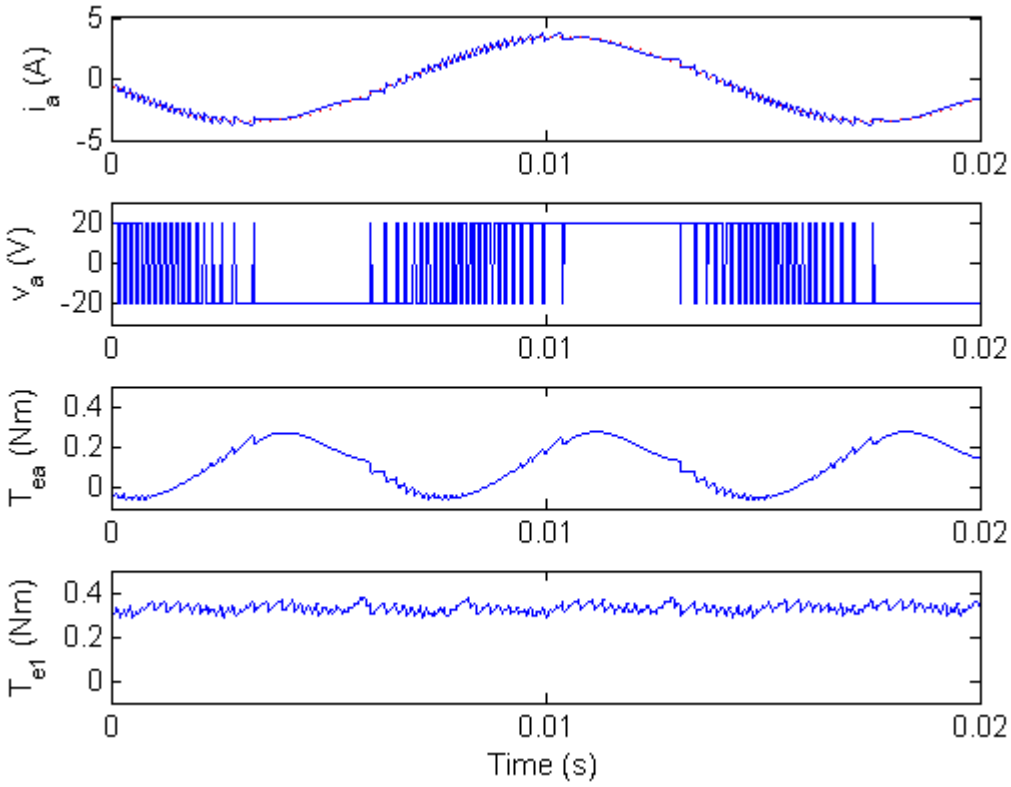

Figure 4.7 Simulation results of the motor drive under a steady-state constant mechanical rotor speed of 219.8 rad/s and at the phase advance angle of $\pi/4$ rad.

4.4.2 Dynamic State Results

A set of simulation results is given here to demonstrate the dynamic performance of the simulated motor drive under torque control. In this test, the motor started from standstill up to a constant speed of 221 rad/s. The torque command was 3.5 A, the DC voltage was 20 V, the hysteresis band was 0.6 A and the load torque was modelled as $0.003 \times \omega_r$ Nm. In Figure 4.8, the phase currents (i_a , i_b , and i_c), the total electromagnetic torque (T_{e1}) of the motor module 1 (the green line) and the phase-A electromagnetic torque (T_{ea}) (the blue line) are given. The mechanical rotor speed (ω_r), the electrical rotor position angle (θ) are also presented. As can be seen in the figure, the total electromagnetic torque generated in the motor drive 1 is initially high, which is reduced as the motor accelerates to a steady-state speed of 221 rad/s. Note that torque ripple also increases as the motor accelerates that is due to the loss of current control.

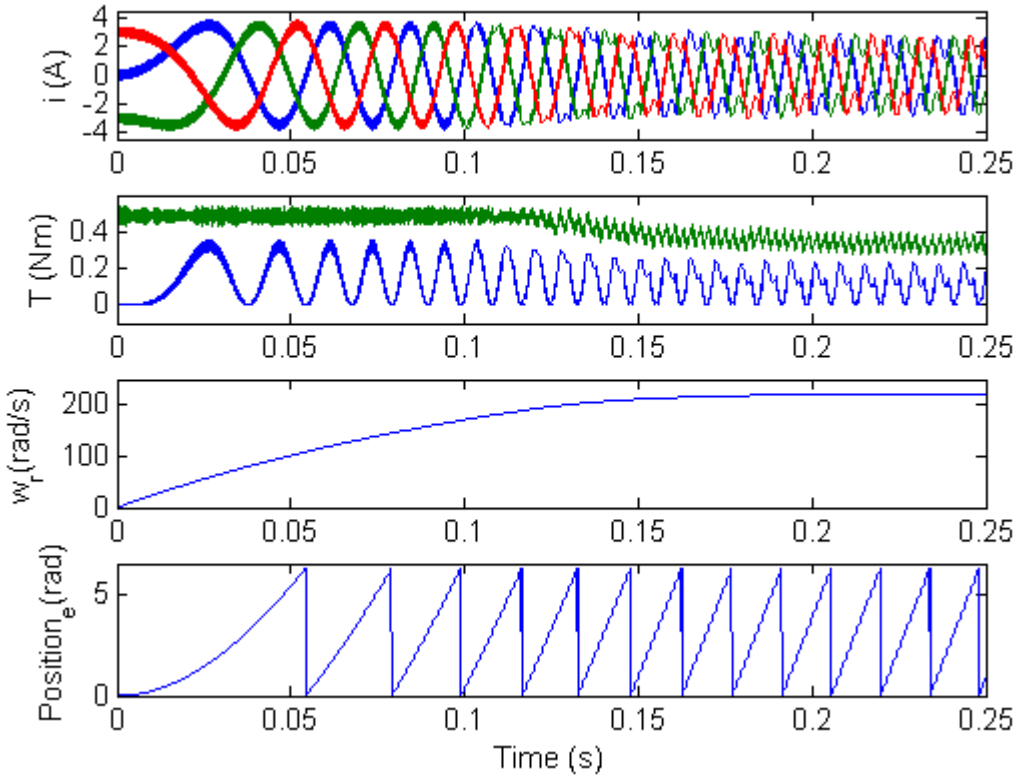

Figure 4.8 Simulation results under dynamic operation while the motor starts from standstill.

4.5 Conclusions

In order to examine the performance of the fault-tolerant PMAC motor drive with redundancy that will be utilized in the position estimation scheme, the entire simulation model is given in this chapter. Each fault-tolerant three-phase sinusoidal PMAC motor was modelled by using the voltage, the electromagnetic torque and the motion equations. The model was formulated entirely in the abc reference frame for direct comparison of the simulation and the experimental results.

The operating conditions in the simulation study include steady-state operation at low and high speeds, and dynamic operation while starting from standstill with load. The simulation results obtained under these conditions demonstrated the typical characteristics of PMAC motors. Although the experimental results were not provided in this chapter, the simulation results demonstrated a close agreement with the real-time off-line test results obtained from the prototype motor drive which will be described in Chapter 6.

As stated previously, the voltage equations utilized in this chapter provides the basis of the sensorless position estimation methods that will be explained in the successive chapter. In addition, the developed Simulink models will be utilized to develop the simulation studies of the proposed sensorless position estimation methods.

5. Principles and Simulation of Fault-Tolerant Sensorless Position Estimation Methods

5.1 Introduction

As was reported in Chapter 3, a large number of sensorless position estimation techniques have been developed for conventional PMAC motors. Most of the developed methods did not consider failures in the motor drive including the machine windings, the inverter or the sensors. The previous position estimation techniques also usually employ star or delta-connected motor drives and hence are not suitable for motor drives with electrically isolated phase windings.

In this chapter, two different fault-tolerant sensorless position estimation schemes are proposed to estimate the rotor position indirectly by using simultaneous measurements of phase currents and phase voltages at a fixed sampling frequency. However, it can be noted that the fixed sampling rate of the proposed position estimators should be at least six times faster than the switching frequency of the H-bridge inverter since the phase voltage has six possible values in each PWM cycle of the inverter when all three-phases are excited with currents in the machine as indicated in [25]. In addition, since the accuracy of the position estimators significantly depends on the sampling rate, the higher sampling frequency results in the better accuracy in the rotor position estimation.

The schemes presented here are based on the incremental flux linkage algorithm that prevents integration drift in the process of flux linkage estimation as developed in [25]. However, the conventional flux linkage incremental technique reported in [25] can produce a single rotor position estimate only by using measurements from all three phases of a conventional three-phase PMAC motor drive. Therefore, it can fail to provide accurate rotor position information under faults in the drive. This chapter presents two modified incremental flux linkage approaches which are capable of achieving multiple rotor position estimates that can be utilized even under faults in the motor drive system.

In the following sections, the proposed fault-tolerant three-phase sensorless position estimation method and the developed fault-tolerant two-phase sensorless position

estimation method are presented. The Simulink-based model is also given. In order to verify the effectiveness of the developed fault-tolerant sensorless position estimation schemes both under normal and faulty operating conditions, a number of simulation results are also presented.

5.2 Principles of the Fault-Tolerant Three-Phase Position Estimation Method

As it will be demonstrated later, a single rotor position estimate can be obtained using the three phase currents and phase voltages in each fault-tolerant PMAC motor drive by adopting the conventional incremental flux linkage algorithm proposed in [25]. Unlike the conventional flux linkage incremental technique applied for a conventional PMAC motor with magnetic and electrical coupling between phases, the winding phase currents are isolated and the mutual inductances in the windings are negligible in each fault-tolerant PMAC motor module. In addition, the motor drive considered here (with two motor modules) can provide two separate rotor position estimates. In normal conditions (no fault), the two position estimates are averaged to obtain a final rotor position estimate for the motor drive. Under faults, however, only the rotor position estimate from the healthy motor drive can be utilized.

5.2.1 Rotor Position Estimation Based on Flux Linkage Increment

Using the equation (4.7), if the sampling frequency is high enough, the change (or increment) of the estimated rotor position for each motor phase can be derived in discrete form as a function of the incremental flux linkage and the other motor parameters.

$$\begin{bmatrix}\Delta\theta_a\\ \Delta\theta_b\\ \Delta\theta_c\\ \Delta\theta_u\\ \Delta\theta_v\\ \Delta\theta_w\end{bmatrix}=\frac{p}{k_e}\begin{bmatrix}\frac{(v_a-Ri_a)\cdot\Delta t-L\Delta i_a}{e_1(\theta)}\\ \frac{(v_b-Ri_b)\cdot\Delta t-L\Delta i_b}{e_2(\theta)}\\ \frac{(v_c-Ri_c)\cdot\Delta t-L\Delta i_c}{e_3(\theta)}\\ \frac{(v_u-Ri_u)\cdot\Delta t-L\Delta i_u}{e_4(\theta)}\\ \frac{(v_v-Ri_v)\cdot\Delta t-L\Delta i_v}{e_5(\theta)}\\ \frac{(v_w-Ri_w)\cdot\Delta t-L\Delta i_w}{e_6(\theta)}\end{bmatrix}=\frac{p}{k_e}\begin{bmatrix}\frac{\Delta\psi_a}{e_1(\theta)}\\ \frac{\Delta\psi_b}{e_2(\theta)}\\ \frac{\Delta\psi_c}{e_3(\theta)}\\ \frac{\Delta\psi_u}{e_4(\theta)}\\ \frac{\Delta\psi_v}{e_5(\theta)}\\ \frac{\Delta\psi_w}{e_6(\theta)}\end{bmatrix} \tag{5.1}$$

Where $\Delta\theta_a$, $\Delta\theta_b$, $\Delta\theta_c$, $\Delta\theta_u$, $\Delta\theta_v$ and $\Delta\theta_w$ are the estimated electrical rotor position increments of the corresponding phases, $\Delta\psi_a$, $\Delta\psi_b$, $\Delta\psi_c$, $\Delta\psi_u$, $\Delta\psi_v$, and $\Delta\psi_w$ are the flux linkage increments, i_a, i_b, i_c, i_u, i_v and i_w are the sampled phase currents and v_a, v_b, v_c, v_u, v_v and v_w are the sampled phase voltages. The phase current increments between two samples are shown by Δi_a, Δi_b, Δi_c, Δi_u, Δi_v and Δi_w. The flux linkage increments shown in the above equation can be calculated using the sampling time Δt and the incremental current Δi as

$$\begin{bmatrix}\Delta\psi_a\\ \Delta\psi_b\\ \Delta\psi_c\\ \Delta\psi_u\\ \Delta\psi_v\\ \Delta\psi_w\end{bmatrix}=\begin{bmatrix}(v_a-Ri_a)\cdot\Delta t-L\Delta i_a\\ (v_b-Ri_b)\cdot\Delta t-L\Delta i_b\\ (v_c-Ri_c)\cdot\Delta t-L\Delta i_c\\ (v_u-Ri_u)\cdot\Delta t-L\Delta i_u\\ (v_v-Ri_v)\cdot\Delta t-L\Delta i_v\\ (v_w-Ri_w)\cdot\Delta t-L\Delta i_w\end{bmatrix} \tag{5.2}$$

Since the two motor modules are connected to a common shaft, the rotor position increments estimated from each phase should generate identical values. However, in practice, the estimated rotor position increments are affected by a number of factors such as inaccurate measurements, parameter variations, and non-ideal motor windings and structure.

As it can be seen in (5.1), the estimated rotor position increment in each phase is proportional to the incremental flux linkage of the corresponding phase divided by the unity back-EMF function of that phase. The unity back-EMF function of each phase, which is seen in the denominators of the right hand side in (5.1), becomes zero twice

every electrical cycle since it is a basically sinusoidal waveform with respect to the rotor position. Therefore, the estimated rotor position increment obtained in each phase can become infinitely large at these rotor positions, hence resulting in significant position errors.

In order to overcome this, equation (5.1) can be modified. To achieve this, both sides of the equation are multiplied by $e_1(\theta)e_2(\theta)$, $e_2(\theta)e_3(\theta)$, $e_3(\theta)e_1(\theta)$, $e_4(\theta)e_5(\theta)$, $e_5(\theta)e_6(\theta)$ and $e_6(\theta)e_4(\theta)$. Then, the three resultant equations in each motor drive are summed. Assuming that the rotor position increments of the three phases of each motor module have the same value, a single rotor position increment for each module can be obtained as given below

$$\begin{bmatrix} \Delta\theta_1 \\ \Delta\theta_2 \end{bmatrix} = \frac{p}{k_e} \begin{bmatrix} \dfrac{\Delta\psi_a e_2(\theta) + \Delta\psi_b e_3(\theta) + \Delta\psi_c e_1(\theta)}{e_1(\theta)e_2(\theta) + e_2(\theta)e_3(\theta) + e_3(\theta)e_1(\theta)} \\ \dfrac{\Delta\psi_u e_5(\theta) + \Delta\psi_v e_6(\theta) + \Delta\psi_w e_4(\theta)}{e_4(\theta)e_5(\theta) + e_5(\theta)e_6(\theta) + e_6(\theta)e_4(\theta)} \end{bmatrix} \tag{5.3}$$

where $\Delta\theta_1$ and $\Delta\theta_2$ are the rotor position increments in the drive modules 1 and 2, respectively.

As it can be observed in the above equations, due to the presence of three back-EMF functions in the denominators of the right side of (5.3) and due to the sum of products of two back EMF functions, the estimated rotor position increment can not be infinitely large. Therefore, it can be concluded that this approach provides more reliable position estimation increments.

Under normal operating conditions (no faults in the drive), if it is assumed that the previous electrical rotor position value for each module is known, the rotor position increment in each module estimated by using the equation (5.3) can be utilised to predict the new electrical rotor position for the corresponding module. This can be done using a simple integration process that utilizes the estimated rotor position increment and the rotor position estimation value obtained at the previous sampling time, as shown in the equation below.

$$\begin{bmatrix} \theta_1^*(k) \\ \theta_2^*(k) \end{bmatrix} = \begin{bmatrix} \theta_1(k-1) + \Delta\theta_1 \\ \theta_2(k-1) + \Delta\theta_2 \end{bmatrix} \tag{5.4}$$

Here $\theta_1^*(k)$ and $\theta_2^*(k)$ are the predicted electrical rotor position values of the motor modules 1 and 2, k and $(k-1)$ are the integers representing the k-th and $(k-1)$-th sampling instants, and $\theta_1(k-1)$ and $\theta_2(k-1)$ are the previous electrical rotor position estimates obtained at the $(k-1)$-th instant in each motor module.

The Modified Phase-Locked Loop (PLL) Technique Utilizing Three Phases

It should be noted that in an ideal motor drive system, the predicted rotor position values obtained with (5.4) should be accurate. In a practical system, however, the rotor position increment for each phase estimated by the equation (5.3) will have errors that are due to inaccurate measurements, parameter variations, quantization errors, time delays and/or finite sampling frequency. Although such errors are small they can accumulate and become significantly large during the integration process. To compensate for such errors, a modified phase-locked loop (PLL) technique can be employed to force the predicted rotor position for each module to be locked to the phase of the flux linkage increments of each module, which is explained in detail in [25].

The modified PLL technique utilized in the study uses the fact that the back EMF voltage of each phase is proportional to the rate of change of flux linkage of that phase which is defined as the flux linkage increment so that the flux linkage increments should have sinusoidal waveforms. Thus, for every phase, the unit back EMF function corresponding to the predicted rotor position should be in phase with the flux linkage increment.

In this PLL, vectors consisting of the flux linkage increments and the back EMF functions in each module are used as inputs to the phase detector of each module as shown in Figure 5.1. The phase detector for each module performs a vector product on the inputs to produce an output proportional to the phase difference between the flux linkage increments and the back EMF functions utilizing the predicted rotor position as demonstrated in the equation below.

$$\begin{aligned}
&\begin{bmatrix} \|\vec{e}\times\Delta\vec{\psi}\|_1 \\ \|\vec{e}\times\Delta\vec{\psi}\|_2 \end{bmatrix} = \begin{bmatrix} \Delta\psi_a e_2(\theta_1^*) + \Delta\psi_b e_3(\theta_1^*) + \Delta\psi_c e_1(\theta_1^*) - \Delta\psi_a e_3(\theta_1^*) - \Delta\psi_b e_1(\theta_1^*) - \Delta\psi_c e_2(\theta_1^*) \\ \Delta\psi_u e_5(\theta_2^*) + \Delta\psi_v e_6(\theta_2^*) + \Delta\psi_w e_4(\theta_2^*) - \Delta\psi_u e_6(\theta_2^*) - \Delta\psi_v e_4(\theta_2^*) - \Delta\psi_w e_5(\theta_2^*) \end{bmatrix} \\
&= \frac{3\sqrt{3}}{2}|\Delta\psi| \begin{bmatrix} \sin(\theta_{f1} - \theta_1^*) \\ \sin(\theta_{f2} - \theta_2^*) \end{bmatrix} \approx K \begin{bmatrix} \theta_{f1} - \theta_1^* \\ \theta_{f2} - \theta_2^* \end{bmatrix} \\
&= K \begin{bmatrix} \delta\theta_1 \\ \delta\theta_2 \end{bmatrix},
\end{aligned} \tag{5.5}$$

Here the flux linkage increments for each phase can be given as $\begin{bmatrix} \Delta\psi_a \\ \Delta\psi_b \\ \Delta\psi_c \\ \Delta\psi_u \\ \Delta\psi_v \\ \Delta\psi_w \end{bmatrix} = |\Delta\psi| \begin{bmatrix} e_1(\theta_{f1}) \\ e_2(\theta_{f1}) \\ e_3(\theta_{f1}) \\ e_4(\theta_{f2}) \\ e_5(\theta_{f2}) \\ e_6(\theta_{f2}) \end{bmatrix}$.

The left hand side of (5.5) represents the vector product of the back EMF function vector and the flux linkage increment vector. The other symbols in the equation (5.5) are: $|\Delta\psi|$ is the amplitude of the flux linkage increments, θ_{f1} and θ_{f2} are the phase angles of the flux linkage increments, $\delta\theta_1$ and $\delta\theta_2$ are the phase differences between the phase angles of the flux linkage increments and the predicted rotor positions, and K is the gain of the phase detectors with the value of $(3\sqrt{3}/2)\cdot|\Delta\psi|$. Note that the amplitudes of the flux linkage increments are assumed to have the same value, $|\Delta\psi|$.

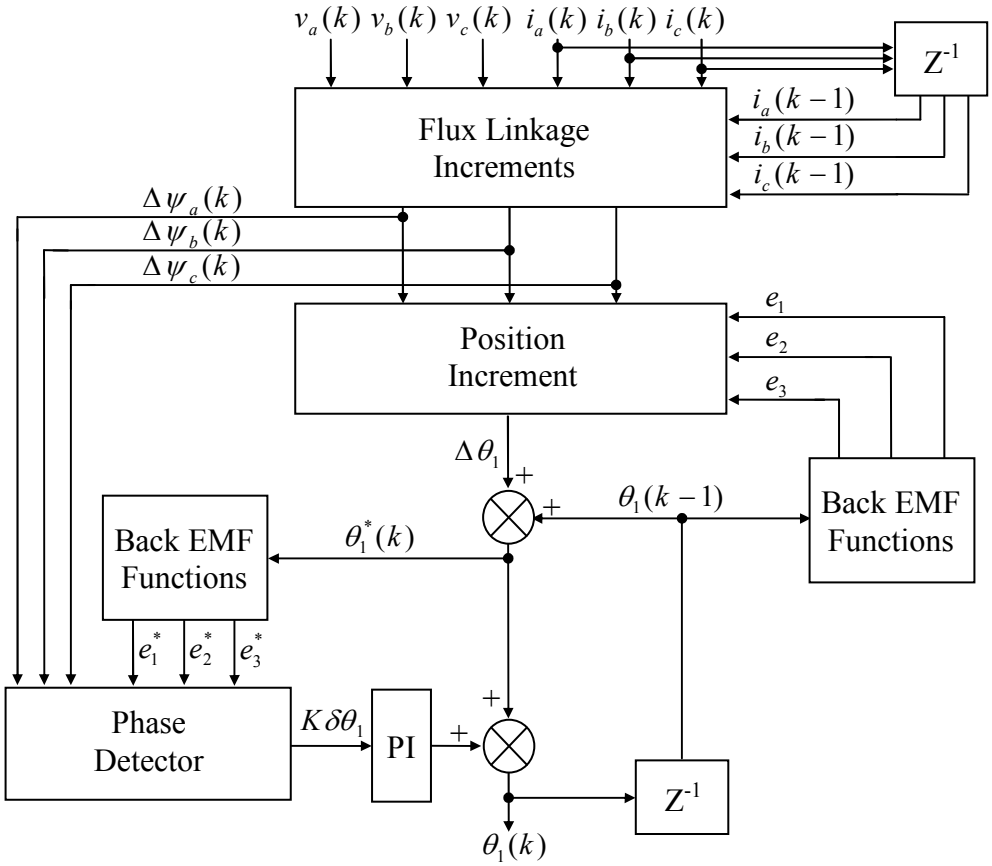

Figure 5.1 Block diagram of the fault-tolerant three-phase sensorless rotor position estimation method for the motor drive module 1

In order to effectively reduce the fluctuations of the estimated rotor position caused by the PLL and improve the stability of the position estimation, the phase detector output of each motor module is then fed into a PI controller forcing the errors to zero (as shown in Figure 5.1), which is added into the PLL as developed in [25]. The output of the PI controller is then added to the predicted rotor position value to obtain a rotor position estimate for each motor module as,

$$\begin{bmatrix}\theta_1(k)\\ \theta_2(k)\end{bmatrix}=\begin{bmatrix}\theta_1^*(k)+K_pK\delta\theta_1(k)+K_i\sum_{n=0}^{k}K\delta\theta_1(n)\\ \theta_2^*(k)+K_pK\delta\theta_2(k)+K_i\sum_{n=0}^{k}K\delta\theta_2(n)\end{bmatrix} \tag{5.6}$$

Here $\theta_1(k)$ and $\theta_2(k)$ are the rotor position estimates of the motor drive modules 1 and 2, K_p and K_i are the proportional and the integral gains of the PI regulators respectively.

5.2.2 A Single Final Rotor Position Estimate

Under normal conditions, a single final rotor position estimate $\theta(k)$ can be obtained by averaging the two available rotor position estimates (one for each motor module).

$$\theta(k)=\frac{\theta_1(k)+\theta_2(k)}{2} \tag{5.7}$$

It can be seen that, under any faulty conditions, only a rotor position estimate obtained from a healthy motor drive can be utilized as the final rotor position estimate. Table 5.1 summarizes the single position estimates in the fault-tolerant motor drive under no fault and faulty conditions.

Table 5.1 Summary of the available rotor position estimates with and without faults

Operating State	**Available Rotor Position Estimates**		**A Single Final Rotor Position Estimate** $\theta(k)$
	Module 1	**Module 2**	
No fault	θ_1	θ_2	$\frac{\theta_1+\theta_2}{2}$
Single Phase Fault or Multiple Phase Fault in Motor Module 1	–	θ_2	θ_2

5.3 Principles of the Fault-Tolerant Two-Phase Sensorless Position Estimation Method

In order to estimate the rotor position indirectly in the fault-tolerant PMAC motor drive with redundancy, the phase currents and the phase voltages of each phase of a motor module need to be measured. This can produce three rotor position estimates for each motor drive. In normal conditions, a single more accurate rotor position can be obtained by averaging all six rotor position estimates obtained in the motor drive containing two motor modules. However, in the case of a fault, position estimates obtained from a pair of two healthy phases in each motor module should be used to obtain the final rotor position estimate. Therefore, it can be seen that this method can increase the reliability of the motor drive significantly as it provides redundant rotor position estimates which is critical under faulty conditions.

5.3.1 The Modified Flux Linkage Incremental Algorithm

As it is explained in Section 5.2, the proposed position estimation method for the fault-tolerant motor drive can provide limited redundant rotor position estimates under faulty conditions. Although a single motor drive module may have only one phase faulty, the rotor position estimation in this module cannot be reliable if the faulty phase is utilized in the estimation method. However, as explained previously the two-phase based position estimation method proposed in this research increases the reliability of the estimation by providing redundant rotor position estimates. In the following paragraphs some of the practical issues that are related to the estimation accuracy will be discussed.

To overcome the zero-crossing problems of the back-EMF functions in the equation (5.1), an alternative approach is proposed in this research to estimate six rotor position increments. This is done by multiplying both sides of the equation (5.1) by $e_1^2(\theta)$, $e_2^2(\theta)$, $e_3^2(\theta)$, $e_4^2(\theta)$, $e_5^2(\theta)$ and $e_6^2(\theta)$ respectively. The resulting equation can be arranged as in (5.8) which indicates the estimated position increments using the voltage-current information from two phases.

$$\begin{bmatrix} \Delta\theta_{ab} \\ \Delta\theta_{bc} \\ \Delta\theta_{ca} \\ \Delta\theta_{uv} \\ \Delta\theta_{vw} \\ \Delta\theta_{wu} \end{bmatrix} = \frac{p}{k_e} \begin{bmatrix} \dfrac{\Delta\psi_a e_1 + \Delta\psi_b e_2}{e_1^2 + e_2^2} \\ \dfrac{\Delta\psi_b e_2 + \Delta\psi_c e_3}{e_2^2 + e_3^2} \\ \dfrac{\Delta\psi_c e_3 + \Delta\psi_a e_1}{e_3^2 + e_1^2} \\ \dfrac{\Delta\psi_u e_4 + \Delta\psi_v e_5}{e_4^2 + e_5^2} \\ \dfrac{\Delta\psi_v e_5 + \Delta\psi_w e_6}{e_5^2 + e_6^2} \\ \dfrac{\Delta\psi_w e_6 + \Delta\psi_u e_4}{e_6^2 + e_4^2} \end{bmatrix} \tag{5.8}$$

Since the back EMF functions are assumed to be sinusoidal functions and since there is a 120^o electrical phase difference between any two phases of the motor modules, the back EMF squared terms in the denominators of the equation (5.8) are always greater than 0.5. This avoids errors around the zero-crossings of the sinusoidal back EMF functions.

Similarly to equation (5.4) in Section 5.2.1, the predicted rotor position for a pair of phases can be given by using the previous rotor position estimate and the estimated rotor position increment.

$$\begin{bmatrix} \theta^*_{ab}(k) \\ \theta^*_{bc}(k) \\ \theta^*_{ca}(k) \\ \theta^*_{uv}(k) \\ \theta^*_{vw}(k) \\ \theta^*_{wu}(k) \end{bmatrix} = \begin{bmatrix} \theta_{ab}(k-1) + \Delta\theta_{ab} \\ \theta_{bc}(k-1) + \Delta\theta_{bc} \\ \theta_{ca}(k-1) + \Delta\theta_{ca} \\ \theta_{uv}(k-1) + \Delta\theta_{uv} \\ \theta_{vw}(k-1) + \Delta\theta_{vw} \\ \theta_{wu}(k-1) + \Delta\theta_{wu} \end{bmatrix} \tag{5.9}$$

Here, $\theta^*_{ab}(k)$, $\theta^*_{bc}(k)$, $\theta^*_{ca}(k)$, $\theta^*_{uv}(k)$, $\theta^*_{vw}(k)$ and $\theta^*_{wu}(k)$ are the predicted rotor position values at the sampling instant k and $\theta_{ab}(k-1)$, $\theta_{bc}(k-1)$, $\theta_{ca}(k-1)$, $\theta_{uv}(k-1)$, $\theta_{vw}(k-1)$ and $\theta_{wu}(k-1)$ are the rotor position estimates at the previous sampling instant $(k-1)$.

As it is mentioned earlier, the rotor position estimation may be in error due to inaccurate measurements, parameter variations, finite sampling frequencies, time delays and quantization errors. Therefore, a modified phase-locked loop (PLL) technique (based on the conventional three phase method, [25]) was adopted that allows the

predicted rotor positions to track the phase of the flux linkage increments of the corresponding phases.

The mathematical expressions related to the above technique are given in the equation (5.10) in the form of a vector product utilizing the flux linkage increments and the back-EMF functions. The result produces an output in each phase detector which is proportional to the phase difference between the phase angle of the flux linkage increments and the predicted rotor position.

$$\begin{bmatrix} \left\|\vec{e}\times\Delta\vec{\psi}\right\|_{ab} \\ \left\|\vec{e}\times\Delta\vec{\psi}\right\|_{bc} \\ \left\|\vec{e}\times\Delta\vec{\psi}\right\|_{ca} \\ \left\|\vec{e}\times\Delta\vec{\psi}\right\|_{uv} \\ \left\|\vec{e}\times\Delta\vec{\psi}\right\|_{vw} \\ \left\|\vec{e}\times\Delta\vec{\psi}\right\|_{wu} \end{bmatrix} = \begin{bmatrix} e_1(\theta^*_{ab})\Delta\psi_b - e_2(\theta^*_{ab})\Delta\psi_a \\ e_2(\theta^*_{bc})\Delta\psi_c - e_3(\theta^*_{bc})\Delta\psi_b \\ e_3(\theta^*_{ca})\Delta\psi_a - e_1(\theta^*_{ca})\Delta\psi_c \\ e_4(\theta^*_{uv})\Delta\psi_v - e_5(\theta^*_{uv})\Delta\psi_u \\ e_5(\theta^*_{vw})\Delta\psi_w - e_6(\theta^*_{vw})\Delta\psi_v \\ e_6(\theta^*_{wu})\Delta\psi_u - e_4(\theta^*_{wu})\Delta\psi_w \end{bmatrix} = \frac{\sqrt{3}}{2}\left|\Delta\psi\right| \begin{bmatrix} \sin(\theta_{f1}-\theta^*_{ab}) \\ \sin(\theta_{f1}-\theta^*_{bc}) \\ \sin(\theta_{f1}-\theta^*_{ca}) \\ \sin(\theta_{f2}-\theta^*_{uv}) \\ \sin(\theta_{f2}-\theta^*_{vw}) \\ \sin(\theta_{f2}-\theta^*_{wu}) \end{bmatrix}$$

$$\approx K \begin{bmatrix} \theta_{f1}-\theta^*_{ab} \\ \theta_{f1}-\theta^*_{bc} \\ \theta_{f1}-\theta^*_{ca} \\ \theta_{f2}-\theta^*_{uv} \\ \theta_{f2}-\theta^*_{vw} \\ \theta_{f2}-\theta^*_{wu} \end{bmatrix} = K \begin{bmatrix} \delta\theta_{ab} \\ \delta\theta_{bc} \\ \delta\theta_{ca} \\ \delta\theta_{uv} \\ \delta\theta_{vw} \\ \delta\theta_{wu} \end{bmatrix}, \quad where \begin{bmatrix} \Delta\psi_a \\ \Delta\psi_b \\ \Delta\psi_c \\ \Delta\psi_u \\ \Delta\psi_v \\ \Delta\psi_w \end{bmatrix} = \left|\Delta\psi\right| \begin{bmatrix} e_1(\theta_{f1}) \\ e_2(\theta_{f1}) \\ e_3(\theta_{f1}) \\ e_4(\theta_{f2}) \\ e_5(\theta_{f2}) \\ e_6(\theta_{f2}) \end{bmatrix} \tag{5.10}$$

Here $\delta\theta_{ab}$, $\delta\theta_{bc}$, $\delta\theta_{ca}$, $\delta\theta_{uv}$, $\delta\theta_{vw}$ and $\delta\theta_{wu}$ are the phase differences between the flux linkage increments and the back EMF functions with respect to the predicted rotor position for each pair of phases and K is the gain of the phase detectors that is given by $(\sqrt{3}/2)\cdot\left|\Delta\psi\right|$.

Then, the output of each phase detector is fed into a PI regulator whose output is added to the predicted rotor position as

$$\begin{bmatrix} \theta_{ab}(k) \\ \theta_{bc}(k) \\ \theta_{ca}(k) \\ \theta_{uv}(k) \\ \theta_{vw}(k) \\ \theta_{wu}(k) \end{bmatrix} = \begin{bmatrix} \theta^*_{ab}(k) + K_p K \delta\theta_{ab}(k) + K_i \sum_{n=0}^{k} K \delta\theta_{ab}(n) \\ \theta^*_{bc}(k) + K_p K \delta\theta_{bc}(k) + K_i \sum_{n=0}^{k} K \delta\theta_{bc}(n) \\ \theta^*_{ca}(k) + K_p K \delta\theta_{ca}(k) + K_i \sum_{n=0}^{k} K \delta\theta_{ca}(n) \\ \theta^*_{uv}(k) + K_p K \delta\theta_{uv}(k) + K_i \sum_{n=0}^{k} K \delta\theta_{uv}(n) \\ \theta^*_{vw}(k) + K_p K \delta\theta_{vw}(k) + K_i \sum_{n=0}^{k} K \delta\theta_{vw}(n) \\ \theta^*_{wu}(k) + K_p K \delta\theta_{wu}(k) + K_i \sum_{n=0}^{k} K \delta\theta_{wu}(n) \end{bmatrix} \tag{5.11}$$

where K_p and K_i are the proportional and the integral gains of the PI regulators respectively.

Fig. 5.2 shows the principal block diagram of the proposed rotor position estimation method for a pair of phases, A and B of the motor module 1.

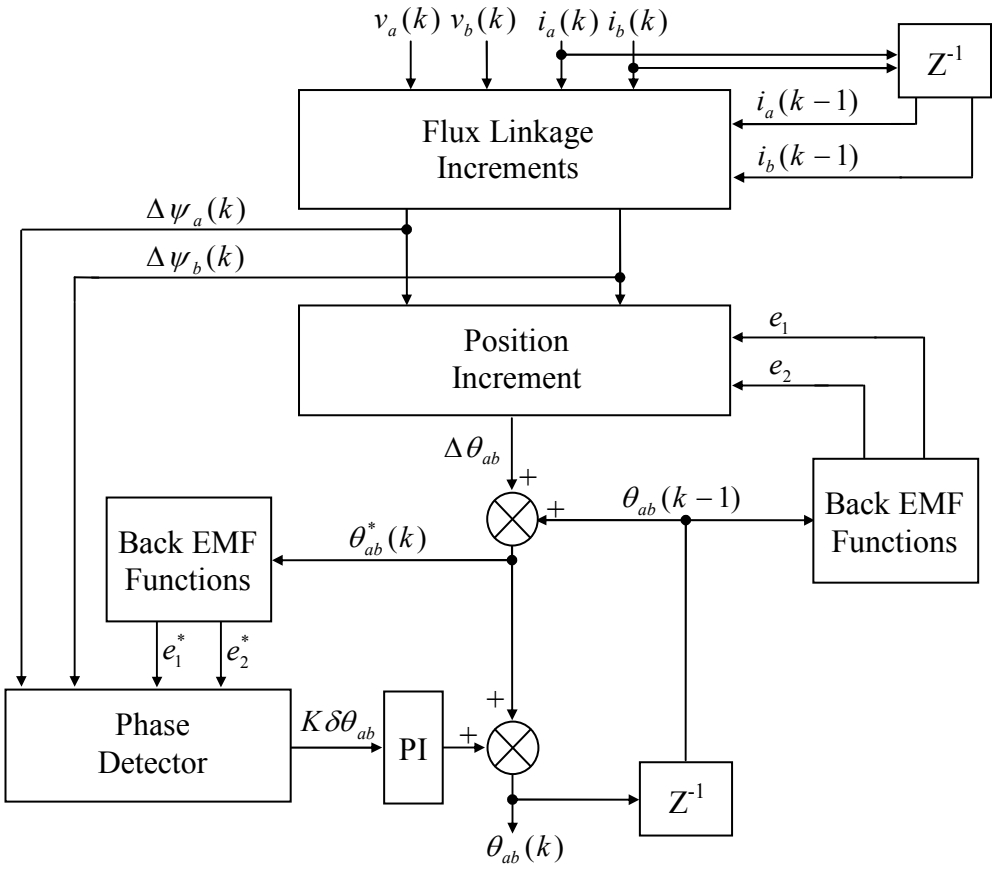

Figure 5.2 The block diagram of the position estimation method given for a pair of phases.

5.3.2 Estimation of a Final Rotor Position

As it was stated before under normal conditions, all six rotor position estimates are averaged to obtain a single final rotor position estimate for the motor drive.

Under a fault in a phase however, the final rotor position is estimated using the average position estimate of the healthy phases of the motor. Table 5.2 summarises the number of rotor position estimates available in the entire fault-tolerant PMAC motor drive with redundancy under both healthy and faulty conditions. The table shows that the rotor position estimation is possible even under a single phase fault in each motor module.

Table 5.2 Summary of the available rotor position estimates with and without faults in the motor drive

Operating State of the Motor Drive	**Available Rotor Position Estimates**		**The Single Final Rotor Position Estimate** $\theta(k)$
	Module 1	**Module 2**	
No Fault	$\theta_{ab},\theta_{bc},\theta_{ca}$	$\theta_{uv},\theta_{vw},\theta_{wu}$	$\frac{\theta_{ab}+\theta_{bc}+\theta_{ca}+\theta_{uv}+\theta_{vw}+\theta_{wu}}{6}$
Single Phase Fault (Phase A of Module 1)	$-\ \theta_{bc}\ -$	$\theta_{uv},\theta_{vw},\theta_{wu}$	$\frac{\theta_{bc}+\theta_{uv}+\theta_{vw}+\theta_{wu}}{4}$
Single Phase Fault in Each Module (Phases A and U of Modules 1 and 2)	$-\ \theta_{bc}\ -$	$-\ \theta_{vw}\ -$	$\frac{\theta_{bc}+\theta_{vw}}{2}$
Two Phase or Three Phase Fault in a Module (Phases A-B, Phases B-C, Phases C-A or Phases A-B-C)	$-\ -\ -$	$\theta_{uv},\theta_{vw},\theta_{wu}$	$\frac{\theta_{uv}+\theta_{vw}+\theta_{wu}}{3}$

As indicated in the table, if the drive is healthy, the method proposed here is analogous to six indirect position sensors (θ_{ab}, θ_{bc}, θ_{ca}, θ_{uv}, θ_{vw} and θ_{wu}). If one phase (say phase A of Module 1) has a fault, however, then only four rotor position estimates are available (θ_{bc}, θ_{uv}, θ_{vw} and θ_{wu}). In the case of a single-phase fault (say phases A and U) in both modules, only two position estimates (θ_{bc} and θ_{vw}) are available. Finally, if two phases or all three phases in one motor module have faults, three rotor position estimates are available from the healthy motor module which can be utilised for the position estimation. By averaging the rotor position estimates obtained from all

available healthy pairs of phases, this estimation method can produce the most accurate rotor position data available.

5.4 Computer Simulation of the Fault-Tolerant Sensorless Position Estimation Methods

In this research, Simulink block models were developed to simulate the fault-tolerant rotor position estimation methods that were explained previously in Sections 5.2 and 5.3. Figure 5.3 (a) illustrates the Simulink block model for the fault-tolerant three-phase sensorless position estimation scheme in a motor module, and Figure 5.3 (b) provides the model for the fault-tolerant two-phase sensorless position estimation method using a pair of phases (phase A and B in the motor drive 1).

It should be noted here that the models given in Figure 5.3 are incorporated both into the Simulink model presented in Figure 4.2 for the steady-state analysis, and the model in Figure 4.4 (b) for the dynamic studies. The zero-order hold blocks (ZOH) in the Simulink models simulates the measured (sampled) voltage and current in a phase.

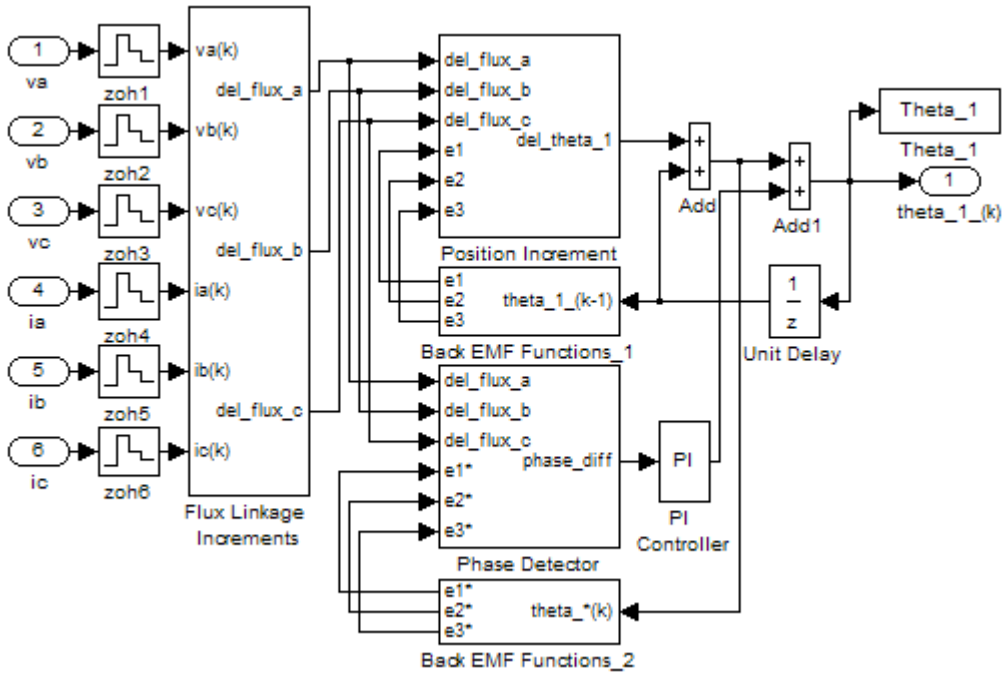

(a)

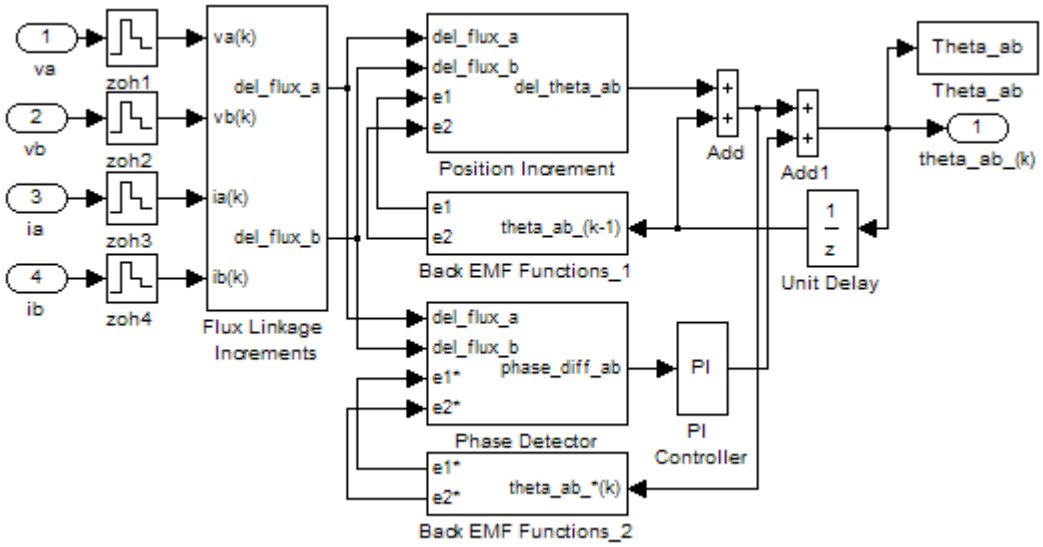

(b)

Figure 5.3 Simulink models of (a) the fault-tolerant three-phase sensorless position estimation method for the fault-tolerant PMAC motor drive 1 and (b) the fault-tolerant two-phase sensorless position estimation method (for a pair of phases A and B of the motor module 1).

5.5 Simulation Results

In order to study and demonstrate the effectiveness of the proposed position estimation techniques, a number of simulation runs were carried out under both normal and faulty operating conditions. The operating conditions were also classified under two groups: steady-state and dynamic operation. The steady-state operations involved tests under a low and a high speed, parameter variations and measurement inaccuracies. The dynamic operation investigated the performance of the drive while it is starting from standstill and under step load changes. In the faulty operating conditions, a one phase winding open-circuit fault, a single current measurement (sensor) fault and a single voltage measurement (sensor) fault were examined.

During the simulation studies, the current command amplitude was set to 3.5 A, the hysteresis bandwidth was set to 0.6 A and the DC link power supply voltage was 20 V. The motor parameters used in the simulation were previously given in Table 4.1. In the PI controller of the PLL system, the proportional gain was 60 and the integral gain was set to zero for the two-phase based estimation scheme. For the three-phase position estimation scheme, however, the proportional gain was 1 and the integral gain was zero in the PI regulator. These gains were chosen by trial and error to give reasonable performance. The sampling time of the simulation was 10 μs .

In the simulation result figures given below, i_a , i_b and i_c are the actual sampled phase currents, and v_a , v_b and v_c are the actual sampled phase voltages. In addition, θ_{act} represents the actual electrical rotor position in the module 1, and θ_{ab} , θ_{bc} and θ_{ca} indicate the two-phase electrical rotor position estimates, and ε_{ab} , ε_{bc} and ε_{ca} are the corresponding position estimation errors. Furthermore, θ_{2ph} and ε_{2ph} are the average two-phase rotor position estimate and the averaged electrical position estimation error in the motor drive module 1 respectively. In the results of the three-phase sensorless position estimation, θ_{3ph} and ε_{3ph} represent the estimated electrical rotor position and the position estimation error in the motor drive module 1 respectively. In all of the results, the unit for the position information is radians.

In this thesis, the performance of the position estimators will be characterized by their position error (in rads). It is important to consider what an acceptable level of position

error is. According to [25], the rotor position estimation errors were limited to 3 to 4% (or 0.19 to 0.25 rads) in a conventional surface-mounted PM synchronous motor with sinusoidal back-EMF voltages and these were considered reasonable. Also, in a comparative study between a standard Luenberger observer and a sliding-mode observer used to estimate the rotor position of a PM synchronous motor [95], the position estimation errors in the steady-state operation were less than 15° (or about 0.26 rads). Based on these papers, the acceptable position estimation errors for sensorless control will be assumed to be of the order of 0.25 rads in this thesis.

5.5.1 Steady State Operation and Position Estimation

In order to examine the steady-state performance of the proposed sensorless position estimation methods, various simulation results were obtained under low and high speed operation.

Figure 5.4 shows the simulation results obtained at a constant rotor speed of 31.4 rad/s (300 rpm). The figure presents the actual phase currents, the actual phase voltages and the actual electrical rotor position. The electrical rotor position estimates and the position estimation errors were obtained for both the two-phase sensorless position estimation method and the three-phase sensorless position estimation method.

The RMS position estimation error results are summarised in Table 5.3. As indicated in the figure, the three two-phase rotor position estimates of one of the motor modules had similar RMS values, and were averaged to obtain a better accuracy. As averaging N number of data ideally should change the RMS error by a factor of $1/\sqrt{N}$ (or 58% for 3 data as the RMS error is $\approx 1/\sqrt{3}$). In practice however a value of about 70% was obtained as shown in Table 5.3. In addition, it can be expected in the two-phase position estimation technique that higher RMS position estimation errors will be produced under faulty conditions as it will not be able to average the estimated position values. Note that the RMS position estimation errors shown in this section need to be utilized for examining or comparing the accuracies of the position estimation methods only. The actual position estimates are utilized in the control of the machine(s).

In addition, it was concluded from that although both position estimation methods had small error levels, the three-phase position estimator had better accuracy than the two-phase position estimator where the RMS position estimation errors were 0.036 and

0.043 rads respectively. Theoretically, both position estimation methods have automatic correction capabilities in two stages using the modified PLL technique and the rotor position prediction process including the internal closed-loop function. However, the position prediction step of the three-phase position estimation technique adopting the conventional flux-linkage incremental algorithm proposed in [25] has an extra auto-correction term shown in the denominators of the equation (5.3) unlike the two-phase position estimator in equation (5.8). This may result in better accuracy in the rotor position estimation.

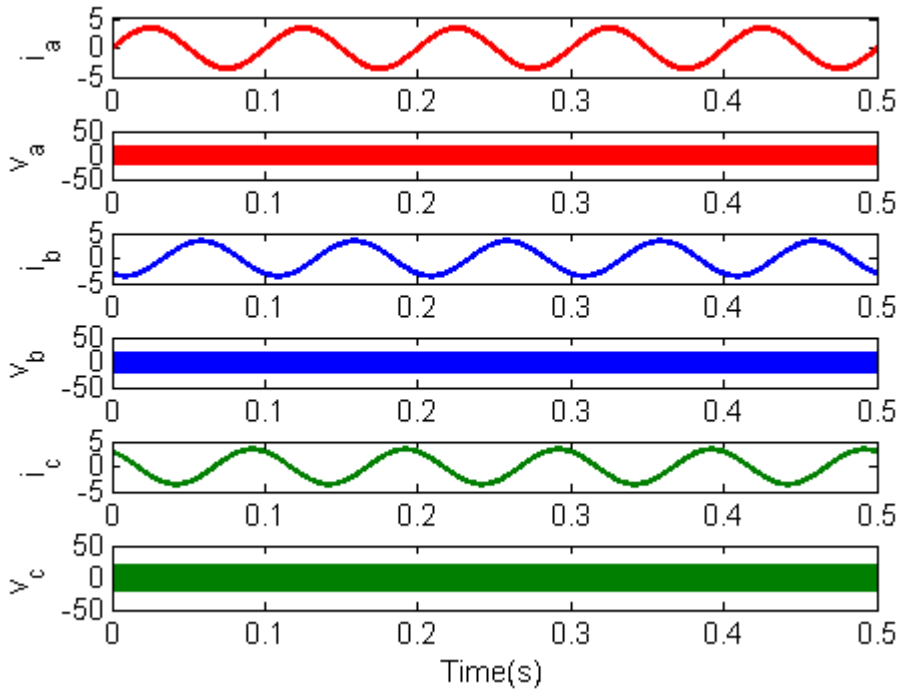

(a)

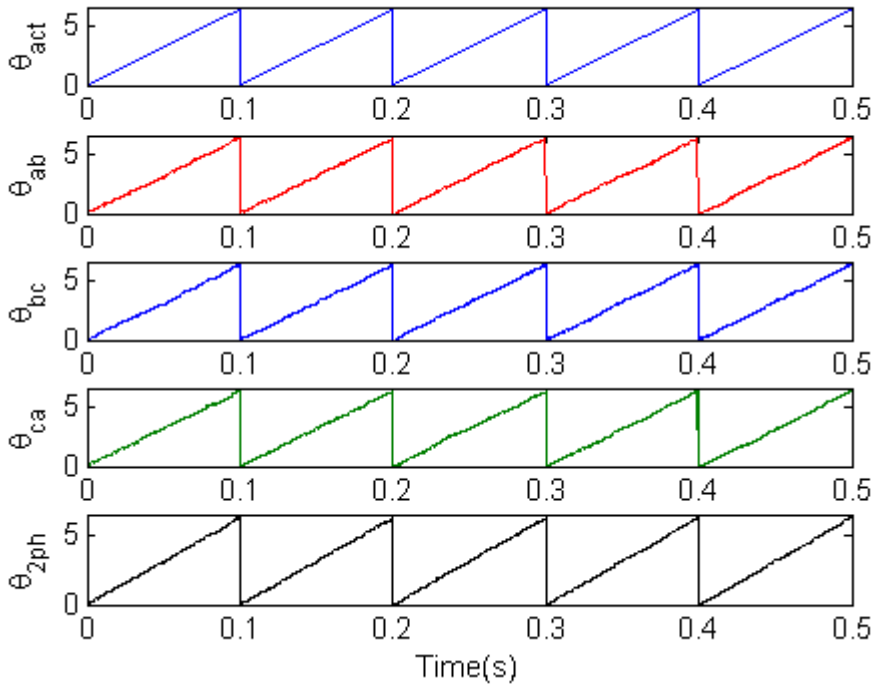

(b)

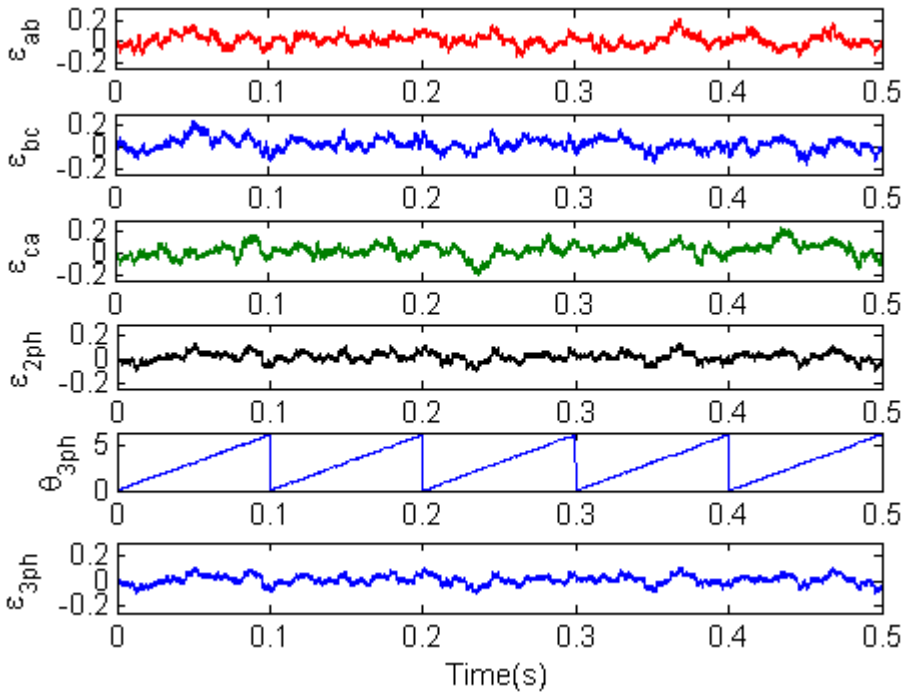

(c)

Figure 5.4 Steady state performance of the fault-tolerant PMAC motor drive 1 at low speed operation (300 rpm). From top to bottom: (a) phase currents and voltages (b) actual and estimated rotor positions, (c) 3ph position estimate and estimation errors.

Table 5.3 RMS position estimation error under steady-state operation

		RMS Position Estimation Error (rad)	
		Two-Phase Method	Three-Phase Method
Low-Speed	Phase a-b	0.0551	
	Phase b-c	0.0594	
	Phase c-a	0.0657	
	Total	0.0434	0.0362
High-Speed	Total	0.0098	0.008

The second set of simulation results (Figure 5.5) is obtained at a steady-state speed of 219.8 rad/s (2,100 rpm) while keeping all other parameters the same as in the previous case. Figure 5.5 illustrates the actual phase currents, the actual phase voltages, the actual electrical rotor position, the electrical rotor position estimates obtained using the two position estimation techniques. The position estimation errors are also given in the figure and Table 5.3. Like the low speed test, the accuracy of the three-phase position estimation method is better than the two-phase position estimator.

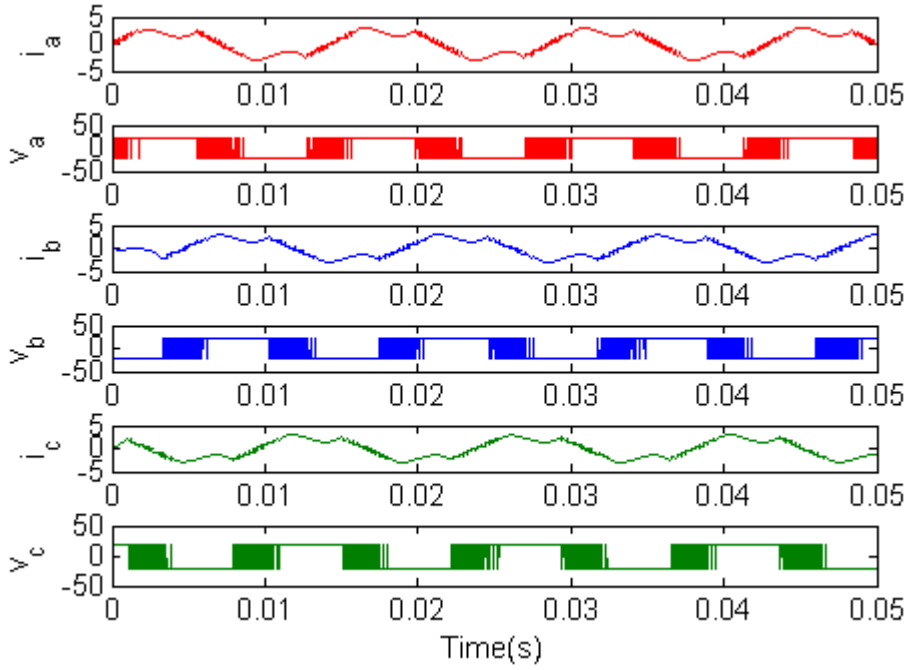

(a)

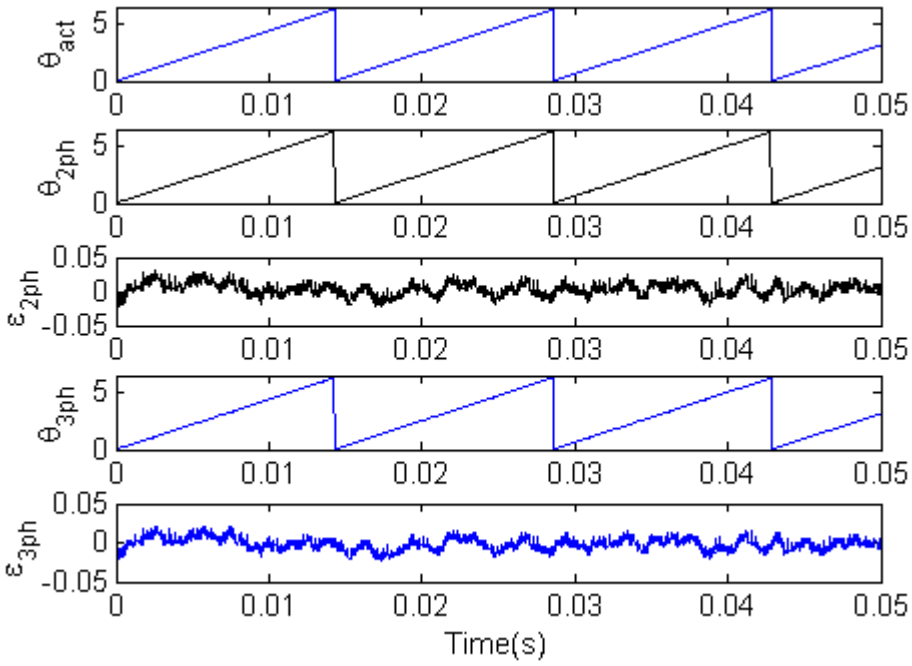

(b)

Figure 5.5 Steady-state performance of the motor drive 1 at a high speed operation of 2100 rpm. (a) phase currents and voltages, (b) actual and estimated rotor positions and errors.

As presented in Table 5.3, both methods can produce much more accurate rotor position information at higher speeds than at low speeds. The RMS position estimation

errors in the high speed test are about 0.008 to 0.01 rads. Although the proposed position estimation methods utilize the auto-correction abilities to compensate for errors generated by motor parameter variations or measurement errors and avoid the integration process in the flux-linkage estimation to reduce the integration drift due to the use of the flux-linkage increments, both techniques still require an integration function in the position prediction process. As well, since the flux-linkage increments utilized in the rotor position increments of both proposed methods are proportional to the rotor speed of the motor and hence are small in the area of low speeds, the rotor position estimation is affected by this speed factor like all the other back-EMF based sensorless techniques as seen in the literature in Chapter 3. This will cause larger errors at low speeds.

A set of simulation results are also given in Figure 5.6 to examine the effect of a wrong initial rotor position in the rotor position estimators for both proposed position estimation schemes. As it can be seen in the figure, the initial position error (2.5 radians) can be compensated within the first electrical cycle due to the automatic correction functions adopted in the position estimation algorithms.

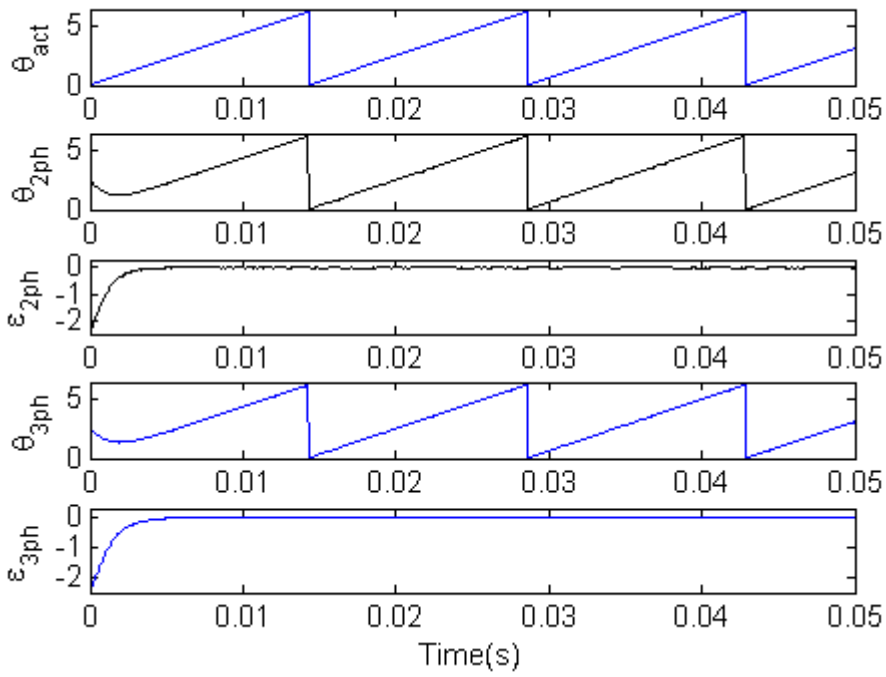

Figure 5.6 Steady-state performance of the motor drive 1 at an operating speed of 2100 rpm (high speed) with an incorrect initial position.

In order to investigate the robustness of the two position estimation schemes against parameter variations and measurement inaccuracies, a series of simulation studies were also performed. In these tests, the original simulation parameters were kept the same as in the previous tests. However, while the rotor position was estimated, the motor parameters and the gains of the current and the voltage sensors were altered from their original values. These alterations also included sensor offsets.

Figure 5.7 shows the simulation results examining the effect of the parameter variations on the accuracy of the position estimation. The motor parameters in question include a variation ($\pm 30\%$) of the phase resistances, the phase inductances and the back EMF constants. The RMS position error results are summarised in Table 5.4. The figures given here present the position estimation errors obtained in the motor drive 1 for two different position estimation methods: two-phase method (blue) and three-phase method (purple). The results demonstrate that both position estimation methods operate well under the parameter changes. However, the variations of the back EMF constants resulted in the highest position estimation errors in both methods. As well, the three-phase position estimator was affected more seriously than the two-phase position estimation method in the back-EMF constant variation. The resistances and the inductances are present in the numerators in equations (5.1) and (5.8) utilized in the rotor position increments of both proposed techniques. On the other hand, the back-EMF constants are in the denominators in both equations and hence their variations may affect more seriously the rotor position estimation than the other parameters. In particular, the reduction of the back-EMF constants resulted in higher position estimation errors since small values in the denominators affected the values in equations (5.1) and (5.8) more.

The resistance variations produced the smallest position estimation errors in the motor parameter variations. The main reason is that as the voltage differences between the phase voltages and the voltage drops due to the phase resistances are multiplied by the sampling interval with a very small value with 10 μs as seen in the equations (5.1) and (5.8), this produces a much smaller change in the estimated rotor position increments than the other parameters.

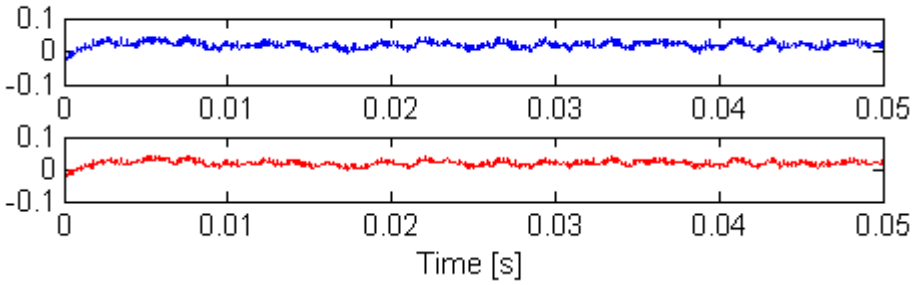

(a) +30 % resistances ($1.3 \times R$)

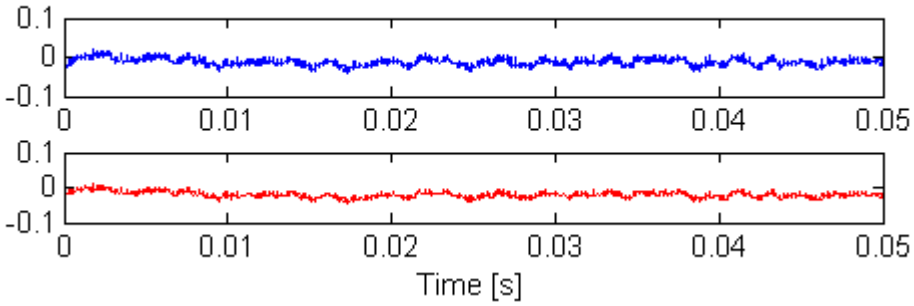

(b) -30 % resistances ($0.7 \times R$)

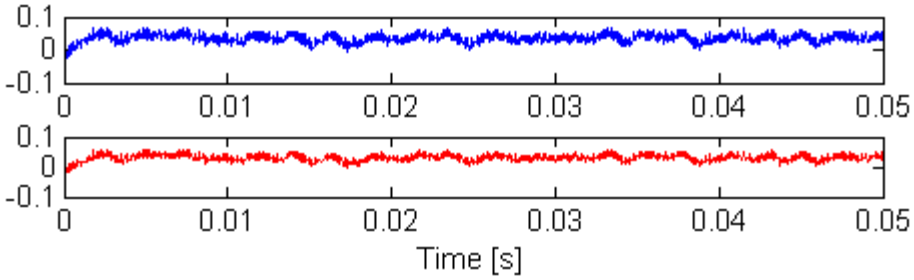

(c) +30 % inductances ($1.3 \times L$)

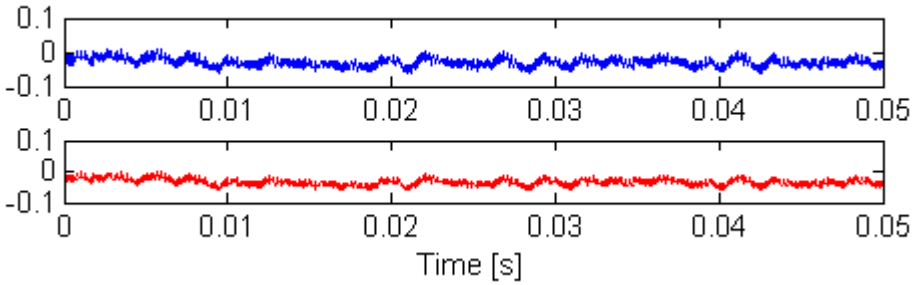

(d) -30 % inductances ($0.7 \times L$)

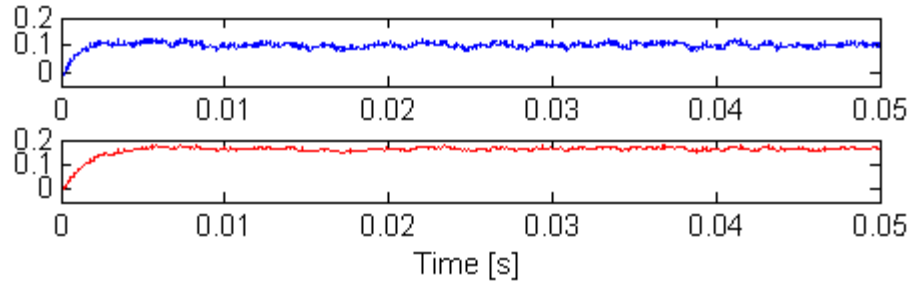

(e) +30 % back EMF constants ($1.3 \times k_e$)

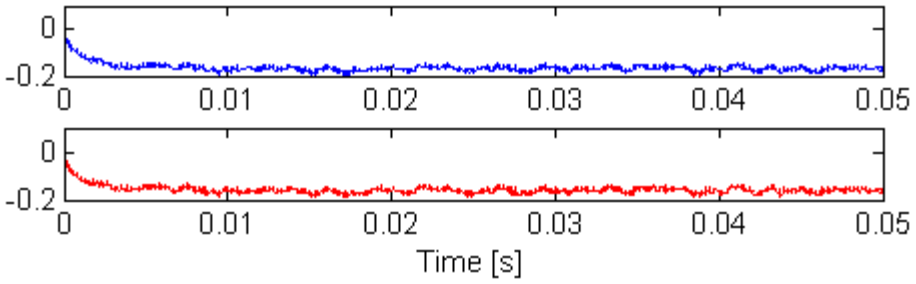

(f) -30 % back EMF constants ($0.7 \times k_e$)

Figure 5.7 The position errors in the motor drive 1 at a speed of 2100 rpm and under the parameter variations: Blue trace (ε_{2ph}), Purple trace (ε_{3ph}).

Table 5.4 RMS position estimation error under parameter variations

	RMS Position Estimation Error (rad)	
	Two-Phase Method	Three-Phase Method
No Parameter Errors	0.0098	0.008
Resistance: +30%/-30%	0.0216/0.0156	0.0203/0.0221
Inductance: +30%/-30%	0.0369/0.0316	0.0318/0.0354
Back-EMF Constant: +30%/-30%	0.0992/0.166	0.161/0.159

Additional simulation studies were also carried out to study the robustness of the position estimators in the case of measurement errors (Figure 5.8 and Table 5.5). In these tests, the gains of the voltage and the current sensors were varied approximately $\pm 10\%$ with regards to the correct values. The offsets of the current sensors were set to be values of ± 0.3 A ($\pm 9\%$ of the 3.5A current command) and the voltage sensor

offsets of ± 2 V ($\pm 10\%$ of the DC link voltage) respectively. The results demonstrate that the variations in the gains of the sensors produce larger estimation errors than the offsets in both algorithms. In particular, the position estimators are most sensitive to voltage gain errors. The current offset variations in both methods resulted in the least position estimation errors. The three-phase position estimation method has better performance than the two-phase method except the cases of the voltage sensor and the current sensor gain variations.

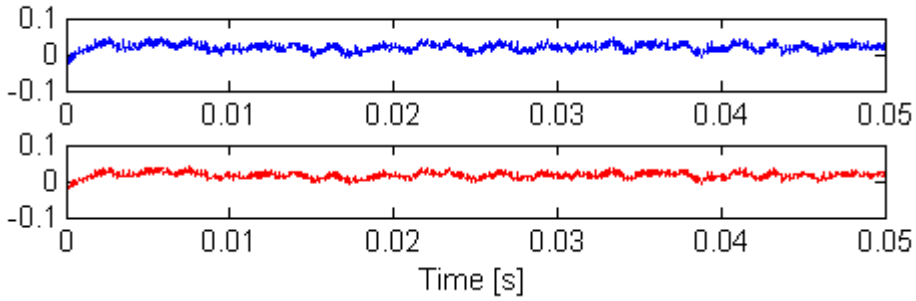

(a) +10 % current sensor gains ($1.1 \times k_i$)

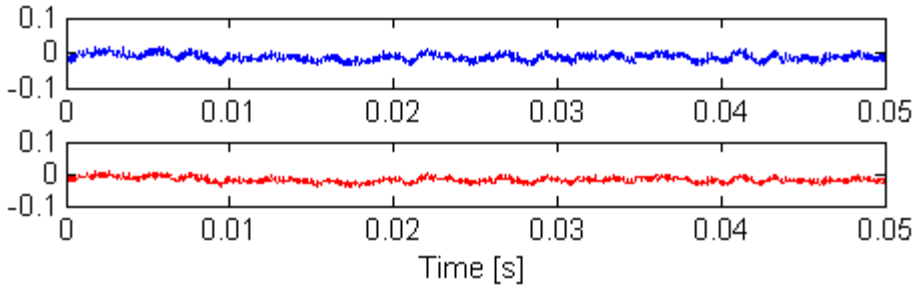

(b) -10 % current sensor gains ($0.9 \times k_i$)

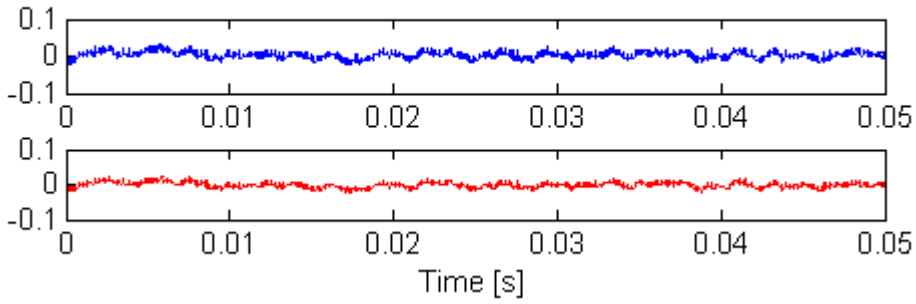

(c) 0.3A current sensor offsets

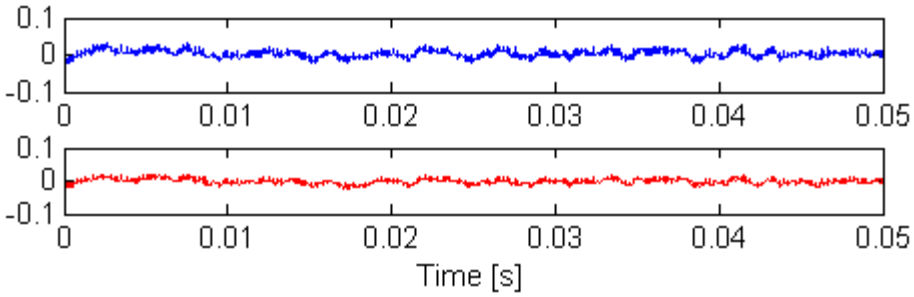

(d) -0.3A current sensor offsets

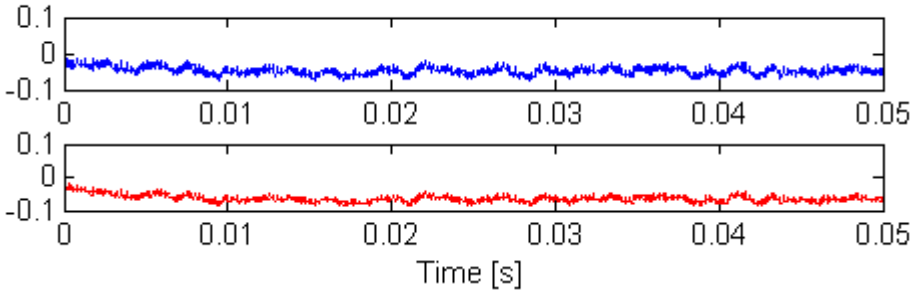

(e) +10 % voltage sensor gains ($1.1 \times k_v$)

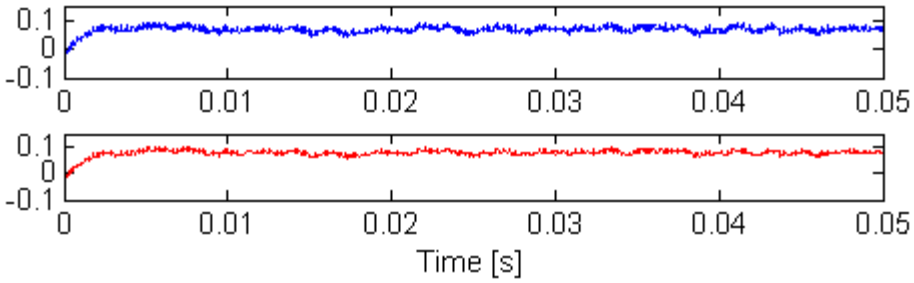

(f) -10 % voltage sensor gains ($0.9 \times k_v$)

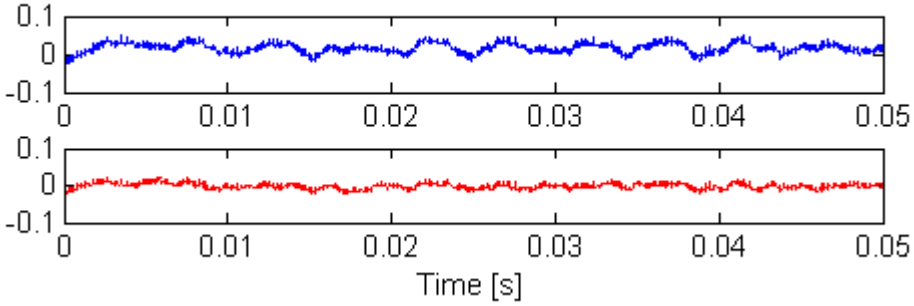

(g) +2V voltage sensor offsets

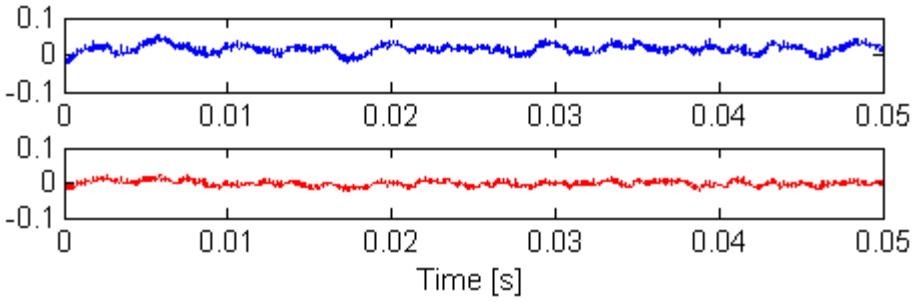

(h) -2V voltage sensor offsets

Figure 5.8 The position errors in the motor drive 1 at a speed of 2100 rpm and under the measurement errors: Blue trace (ε_{2ph}), Purple trace (ε_{3ph}).

Table 5.5 RMS position estimation error under inaccurate measurements

		RMS Position Estimation Error (rad)	
		Two-Phase Method	Three-Phase Method
No Measurement Errors		0.0098	0.008
Current Sensor	Gain: +10%/-10%	0.0215/0.0161	0.0177/0.0204
	Offset: +0.3A/-0.3A	0.0098/0.0101	0.008/0.008
Voltage Sensor	Gain: +10%/-10%	0.0491/0.0681	0.0648/0.0785
	Offset: +2V/-2V	0.0207/0.0198	0.008/0.008

5.5.2 Simulation Studies to Investigate the Dynamic Operation

Several simulation tests were carried out to explore the dynamic performance of the position estimators, including starting from standstill, step load changes, and starting with an incorrect rotor position value.

In the starting test in Figure 5.9, the motor system was simulated accelerating from 0 to 221 rad/s (2,111 rpm) under a load torque of $0.003 \times \omega_r$ Nm. The set of results given in Figure 5.9 includes the actual phase currents, the actual phase voltages, the actual rotor position, the rotor position estimates and the position estimation errors for the proposed position estimators. The results show a moderate initial position estimation error which reduces as the motor speed increases.

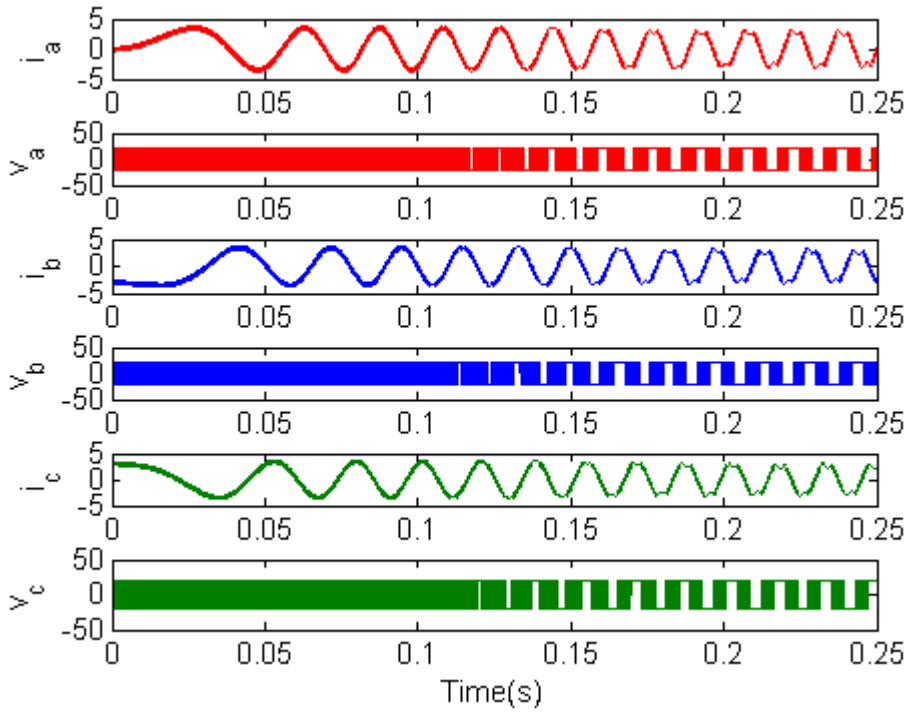
i_a
v_a
i_b
v_b
i_c
v_c
5
0
-5
50
0
-50
0
0.05
0.1
0.15
0.2
0.25
Time(s)

(a)

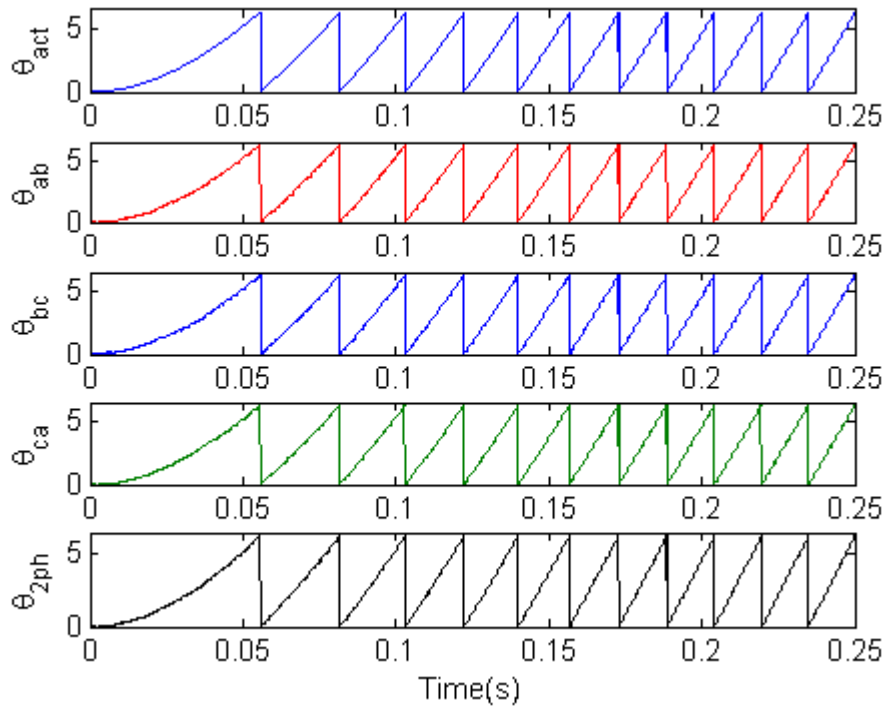
θact
θab
θbc
θca
θ2ph
5
0
0
0.05
0.1
0.15
0.2
0.25
Time(s)

(b)

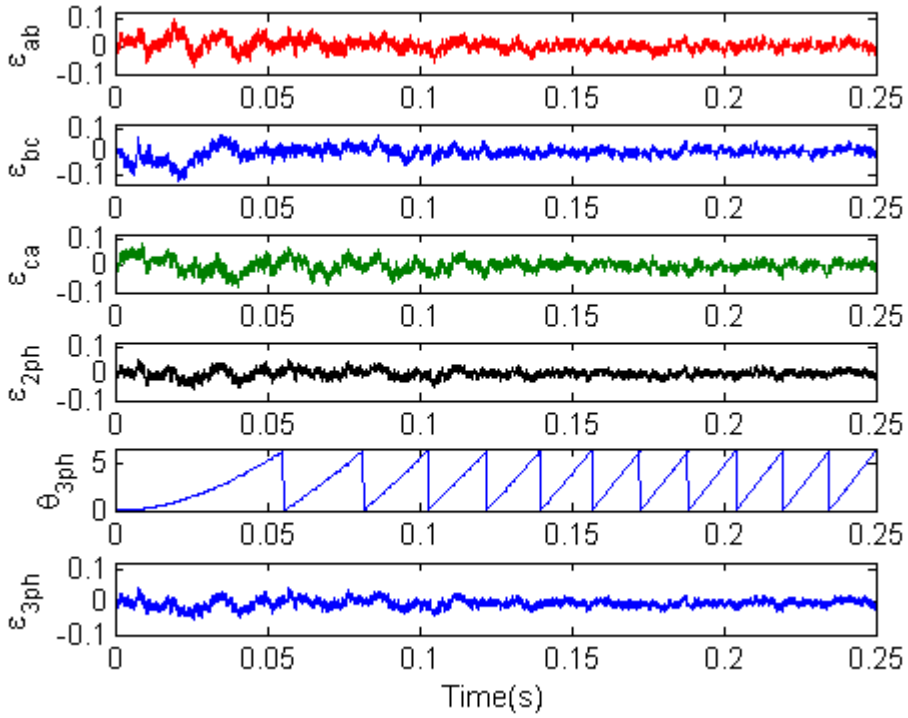

(c)

Figure 5.9 Starting performance of the motor drive 1. (a) phase currents and voltages (b) actual and estimated rotor positions, (c) 3ph position estimate and estimation errors.

The effect of the wrong initial rotor position values on estimating the position is studied in Figure 5.10. The original initial electrical rotor position of the motor system was 0 rad, which is changed to 2 radians in this test. The results show that in both estimators, the estimated rotor position values converge to the actual rotor position values with the small RMS errors less than 0.01 rads within the first electrical cycle.

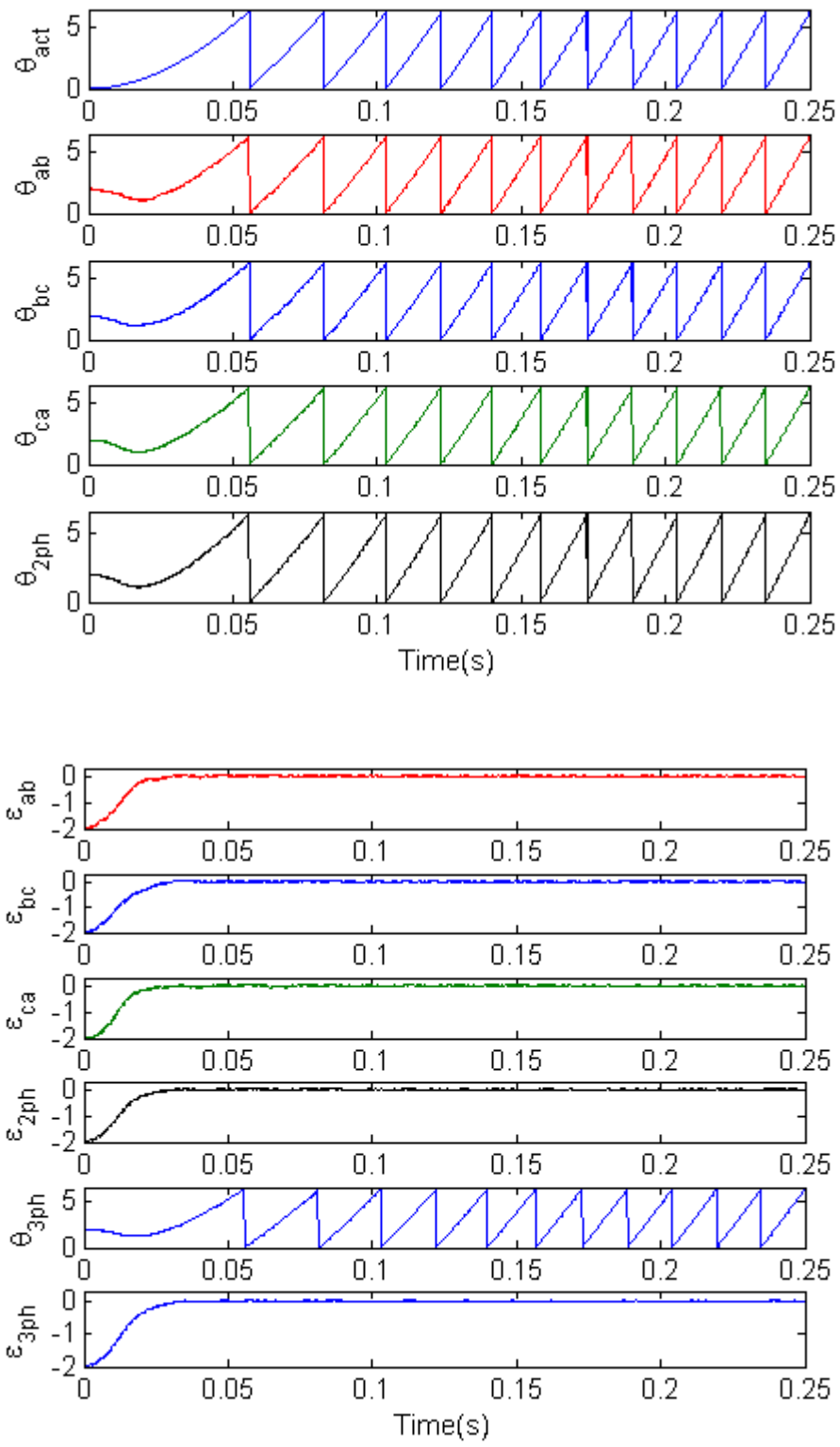

Figure 5.10 Starting performance of the motor drive 1 with an incorrect initial position.

In the step load test, while the motor system was rotating at a constant steady-state speed of 221 rad/s under a load torque of $0.003 \times \omega_r$ Nm (0.66 Nm), the torque load

was changed to $1+0.003\times\omega_r$ Nm (1.66 Nm) at the time instant of 0.25 sec, which caused the motor to decelerate. Then, the load torque is reduced back to $0.003\times\omega_r$ Nm at 0.45 sec, which caused the motor to accelerate again. The results are given in Figure 5.11.

As it can be seen in the figure, the phase currents are visibly distorted both before and after the application of the step load change. This is due to the fact that the back EMF voltages induced in the phase windings are too high to cause a sufficiently large effective voltage across the winding phases, which prevents the regulation of the load current. Conversely, the effective winding voltage is increased at low motor speed (higher load) due to the low back-EMF, which thus demonstrates a well-regulated load current (around 0.3-0.5 sec).

The dynamic simulation results demonstrate that both position estimation methods have excellent performance under the step load changes for typical practical loading conditions. However, as the motor speed decreases with the increasing step load, the position error increases slightly.

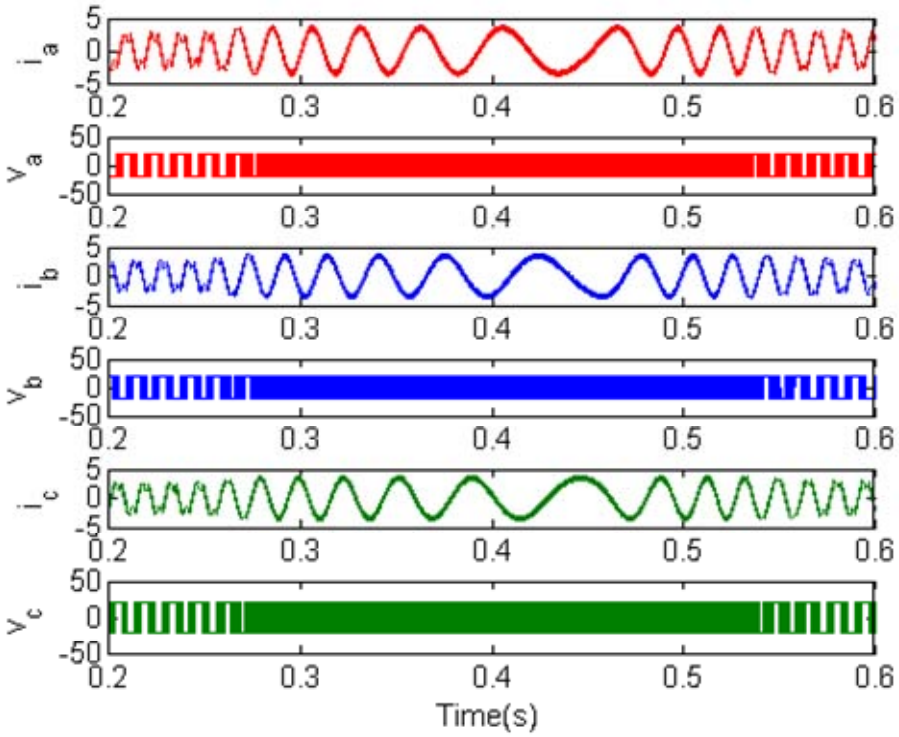

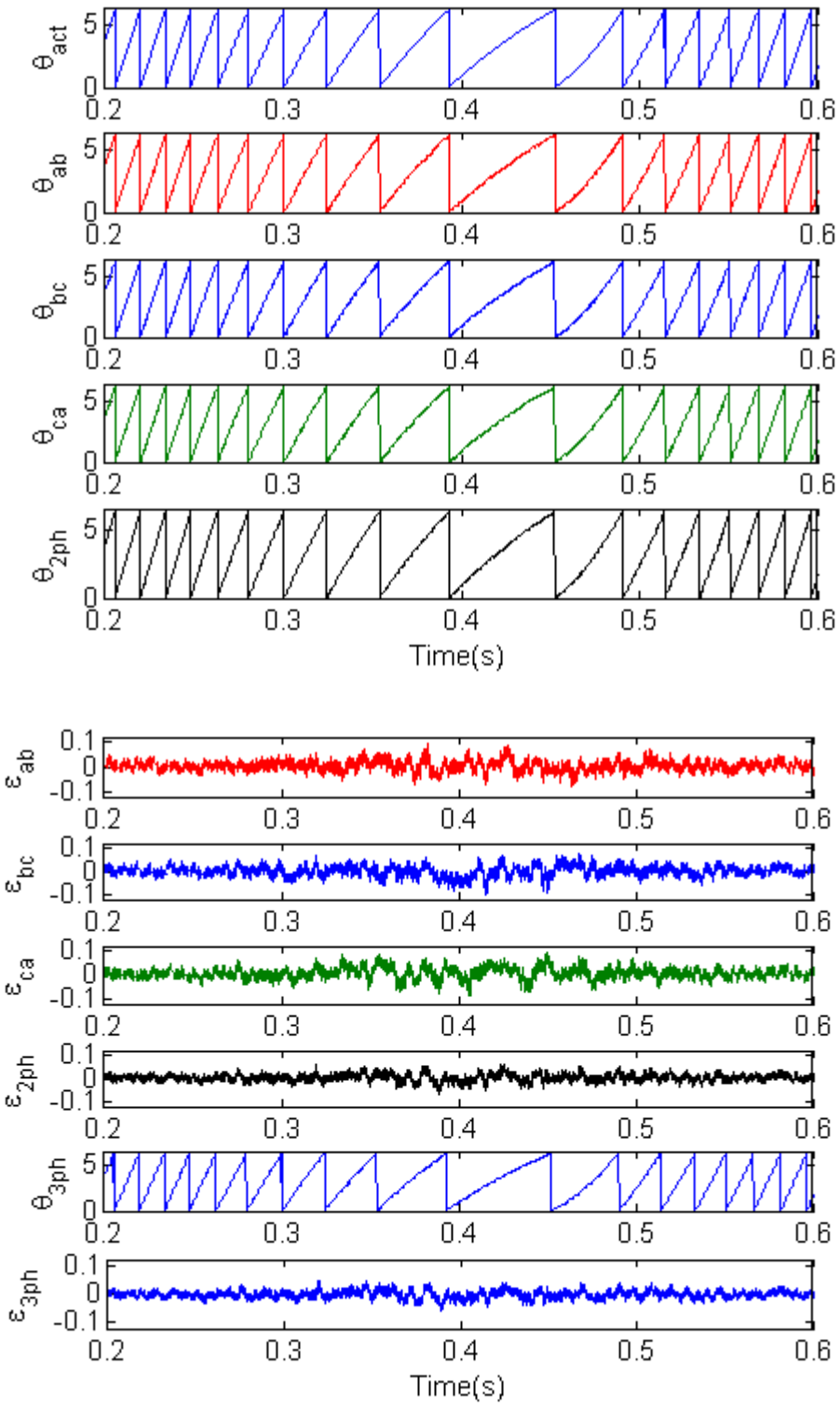

Figure 5.11 Dynamic operation performance of the motor drive 1 under step load changes.

5.5.3 Operation Under Faults

In this section, several simulation results are presented to investigate the performance of the position estimation methods under various faults such as a winding phase open-circuit fault, a current sensor failure and a voltage sensor fault.

Phase Winding Open-Circuit Failure

Figure 5.12 presents a set of simulation results obtained under an open-circuit fault in stator winding phase C of the motor drive 1, while the motor is running at a steady-state speed of 1,968 rpm. The open-circuit fault was introduced at the instant 0.25s. As it is shown in the phase terminal voltage figure, until the instant of fault, the voltage across the subject phase illustrate the switching DC voltage levels. The current in the phase C is also present as in the other two phases. After the introduction of the fault however the current becomes zero, and the terminal voltage shows the back EMF voltage as expected. As it can be seen in the figure, the position estimators perform well under the open-circuit fault.

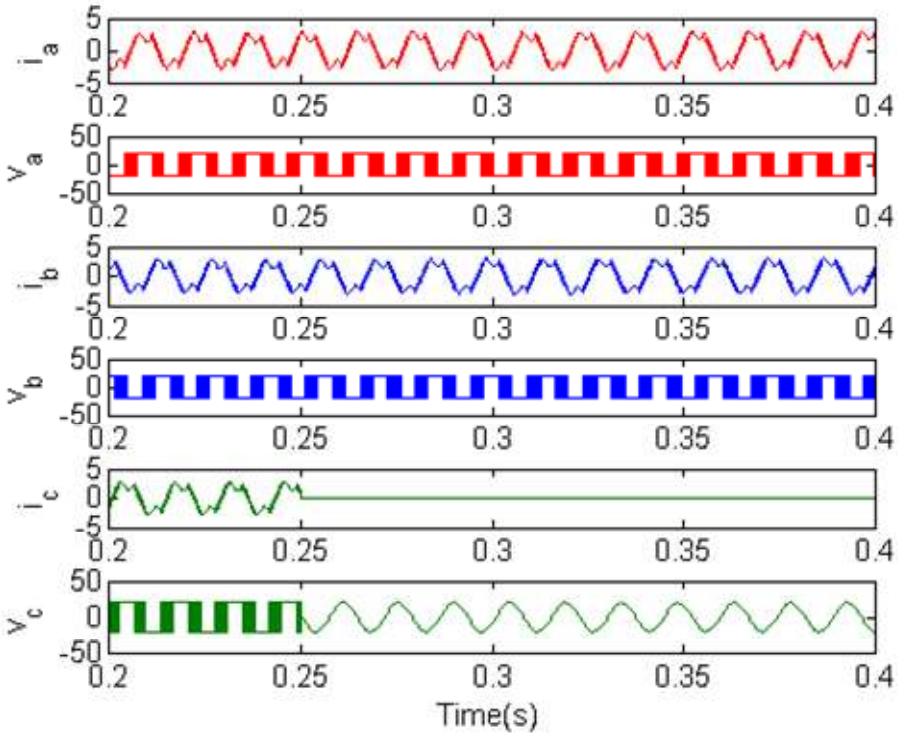

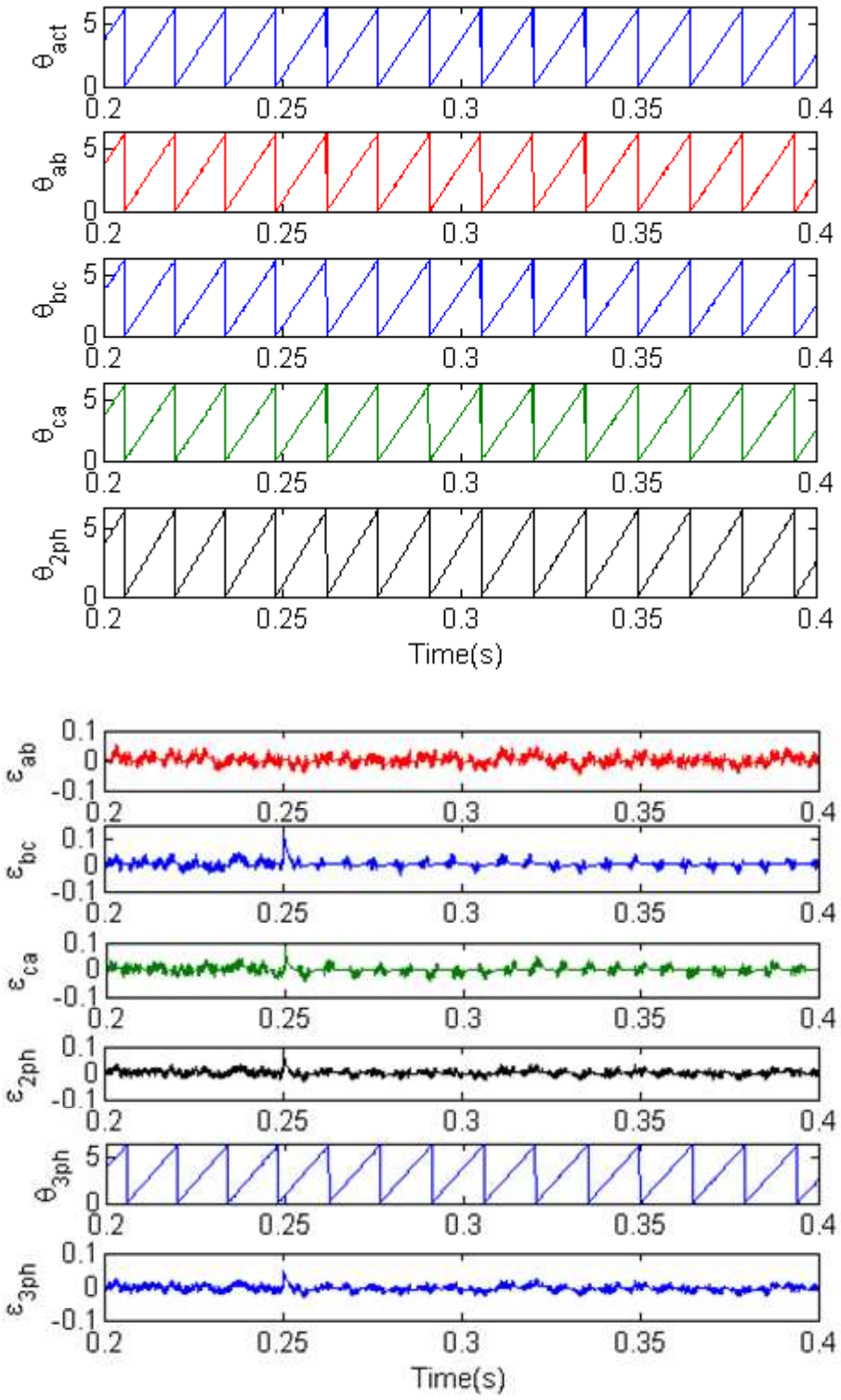

Figure 5.12 Characteristic waveforms of the motor drive 1 under an open-winding fault in the phase C.

Single Current and Voltage Sensor Fault

The simulation results given in Figure 5.13 and Table 5.6, examine the performance of the proposed position estimation methods in the presence of a current sensor or a

voltage sensor failure. These sensors are utilized to measure the winding current or terminal voltage of a phase. The gain in each sensor was set to 10 times greater than the original sensor gain to simulate the sensor failure. As it can be seen in the simulation results, even under a single sensor failure, the two-phase based position estimation technique can estimate rotor position values with small RMS position estimation errors of 0.013 rads utilizing only a healthy pair consisting of phases B and C. It can be reported that using the adoption of the modified PLL, the predicted rotor position is locked into the phase of the flux linkage increment. Hence, the two-phase method cannot lose the auto-correction ability, which is essential in the position error correction and self-starting. This ensures that the estimated rotor position can be used to implement a closed-loop control in real time.

However, the three-phase based position estimation scheme failed to achieve reasonable accurate rotor position estimates. Similarly, the two-phase position estimation method could not obtain correct rotor position information using two faulty pairs involving A-B and C-A, where the phase A measurement had fault.

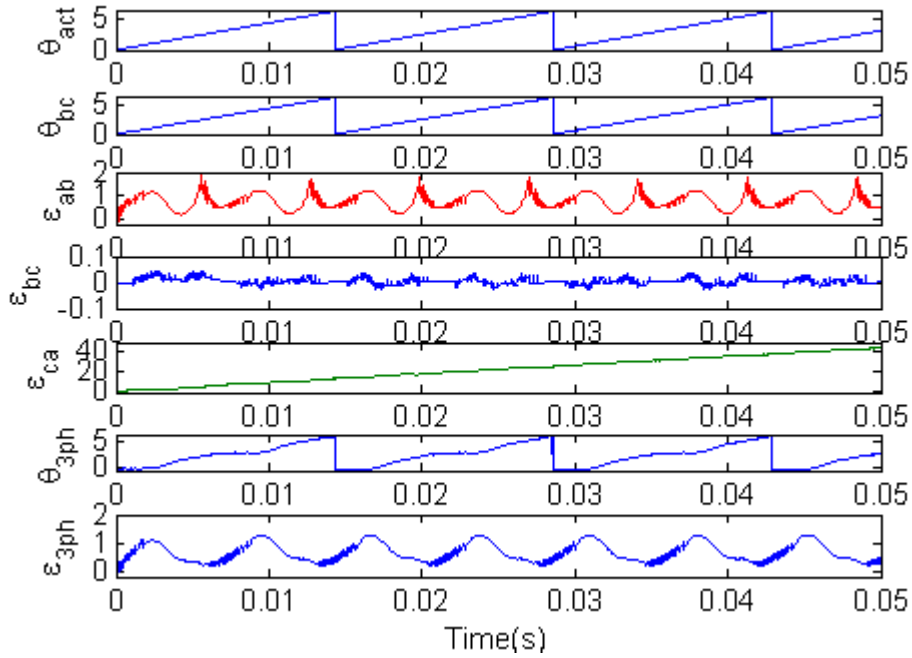

(a) a current sensor fault in phase A

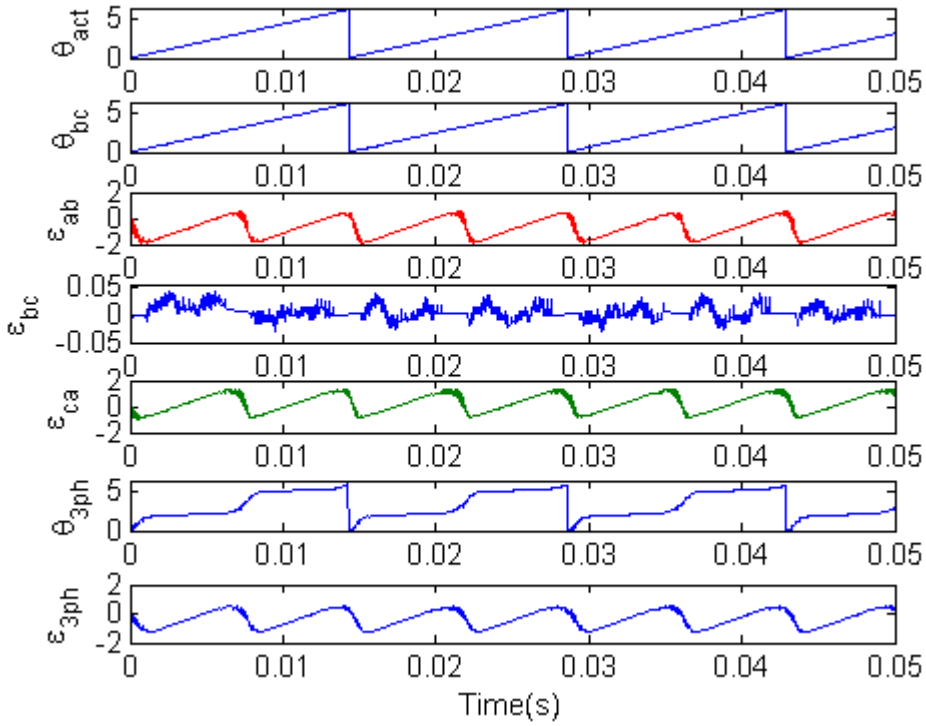

(b) a voltage sensor fault in phase A

Figure 5.13 Performance of the position estimators in the motor drive 1 under (a) a current sensor fault (with 10 times greater gain) in phase A, (b) a voltage sensor fault (with 10 times greater than the original gain) in phase A.

Table 5.6 RMS position estimation errors under a current or a voltage sensor fault in Phase A (introducing a gain that is 10 times greater compared to its original value)

		RMS Position Estimation Error (rad)	
		Two-Phase Method	Three-Phase Method
Current Sensor Fault in Phase A	Phase a-b: before/after	0.0131/0.836	
	Phase b-c: before/after	0.0126/0.0126	
	Phase c-a: before/after	0.0124/large	
	Total: before/after	0.0098/large	0.008/0.743
Voltage Sensor Fault in Phase A	Phase a-b: before/after	0.0131/1	
	Phase b-c: before/after	0.0126/0.0126	
	Phase c-a: before/after	0.0124/0.722	
	Total: before/after	0.0098/0.482	0.008/0.666

Note that only three faults (winding-open circuit fault, current sensor fault and voltage sensor fault) were demonstrated in this research. The other faults such as inverter faults (power device short-circuit, power device open-circuit and DC link capacitor failure), winding faults (due to winding short-circuit at the terminals, turn-to-turn short-circuit in a phase winding, phase-to-phase short-circuit, phase-to-ground short-circuit, and winding open-circuit), current or voltage sensor failures, faults in the controller, and power supply faults, can be considered in the study.

However, to be able to study such faults, it is necessary to detect them by using a fault detection method and remove these faults in order to avoid the propagation of the fault to the other healthy phases using various remedial post-fault strategies. Then, the rotor position estimators can utilize remaining healthy phases to estimate the rotor position. However the fault detecting methods and the remedial strategies for the fault-tolerant motor drives were beyond the scope of this thesis as they were covered in [14].

5.6 Conclusions

In order to obtain the rotor position information indirectly in the fault-tolerant three-phase surface-mounted sinusoidal PMAC motor drive with redundancy, a three-phase position estimation method and a two-phase position estimation method was developed.

The position estimation methods are based on the flux linkage increments which utilize the measurements of the phase currents and the voltages of the motor drive.

As the name suggests, the three-phase estimation method utilizes the measured data from all three phases in each motor module to obtain a single rotor position estimate producing a total of two rotor position estimates. However, the two-phase position estimation method utilizes the measurements from a pair of phases resulting in a total of three rotor position estimates in each motor module. This results in a total of six rotor positions in a motor drive containing two three-phase motor modules.

In the position estimation methods proposed the position estimates are averaged to obtain a final rotor position estimate. In the case of a fault however, only the healthy phase(s) are used to calculate the final position.

In order to validate the effectiveness of the position estimation methods, studies were also carried out both under normal and faulty operating conditions using phase voltages and currents obtained from simulations. In the simulation study the Simulink models of the motor drive developed in the previous chapter were utilized. The simulation studies included both dynamic and steady-state operation of the motor drive.

As a result of this study, the characteristic features of the proposed fault-tolerant sensorless position estimation techniques can be listed as:

- Both position estimation methods show acceptable steady-state performance at high and low speeds. However, it was observed that the position estimation error is significantly larger at low speed than at high speed.
- The position estimators demonstrated good dynamic performance under starting from standstill and step load changes, and produced similar position accuracies. As expected during the starting process the position estimation errors were larger initially but improved at higher speeds.
- The methods were also tested for motor parameters changes and it was found that errors in the back EMF constant affects the position error more significantly than errors in the resistance and the inductance of the windings.
- The robustness against measurement errors were also examined including gain errors and offset errors in the current and voltage sensors. It was found

that the voltage sensor gain errors resulted in the largest position estimation errors, but the estimation errors were again acceptable.

- In both methods, the rotor position estimators displayed good performance even starting with an incorrect initial rotor position (2 rad), and the estimation error reduces to an acceptable level within a few electrical cycles.
- As stated previously, both methods can provide multiple rotor position estimates in a dual-module drive hence increase the reliability.
- Although both position estimation techniques operate reliably, the two-phase position estimation method has a greater degree of fault-tolerance than the three-phase position estimation method.

6. Analysis of the Position Estimators using the Real Time Off-Line Data

6.1 Introduction

As shown in Chapter 5, in order to examine the performance of the proposed sensorless methods for the fault-tolerant PMAC motor drive with redundancy, computer simulation studies were done using Simulink and the results demonstrated the effectiveness of the methods under normal and faulty conditions. However, due to measurement and motor model inaccuracies, it is crucial to test the proposed methods under real operating conditions.

Therefore tests were done using the actual hardware where extensive real time data was captured for processing in the position estimators. The operating conditions in the real time tests include steady-state operation at low and high speeds, starting from standstill, step load changes, parameter variations, measurement errors, starting with incorrect initial rotor position data, an open-circuited fault in a single phase winding and a failure of one of the current or voltage sensors.

In the tests, the fault-tolerant PMAC motor drive system developed in [14] is utilized. The experimental setup was identical to the simulated drive: two fault-tolerant PMAC motor drives on a common shaft, H-bridge type inverter per phase and a common DC power supply, three current measurement circuits and a DSP-based (Digital Signal Processor) motor controller for each motor module. An incremental encoder was also mounted on the rotor shaft to provide the actual rotor position which is utilized for current commutation in the motor drive. The position sensor data is also measured during the tests to compare with the estimated values. To provide a load for the motor drive system, a DC generator was mounted on the shaft of the motor and a power resistor and a switch were used to electrically load the motor under test.

During the tests, one of the motor modules was operated under the torque control mode described in [14]. Off-line real data was obtained by a LabVIEW-based data acquisition system. The off-line real data captured includes the phase currents, the phase voltages and the pulse signals generated by the incremental encoder.

As stated previously, the rotor position estimates are obtained using the position estimation methods that require the measured phase currents and phase voltages. The custom-written LabVIEW software also performed the off-line position estimation calculation in this study.

In this chapter, the experimental setup is explained briefly, including the data acquisition system. Various test results are then given to verify the effectiveness of the developed sensorless position estimation methods for the fault-tolerant PMAC motor drive under normal and faulty conditions.

6.2 The System Hardware of the Motor Drive

The photo of the test setup is given in Figure 6.1 and its schematic block diagram is presented in Figure 2.1. The setup includes two fault-tolerant PMAC motor drive modules on a common shaft. An incremental encoder HEDS-5640 with 500 PPR (pulses per revolution) is used to measure the rotor position. The encoder produces square-wave signals from channels A and B (90° out of phase) with another signal as an index pulse. The encoder outputs are connected to the DSP-based motor controllers via the encoder interface modules. The DC generator is connected to a variable power resistor of resistance 12.4Ω and current rating 10A through a switch.

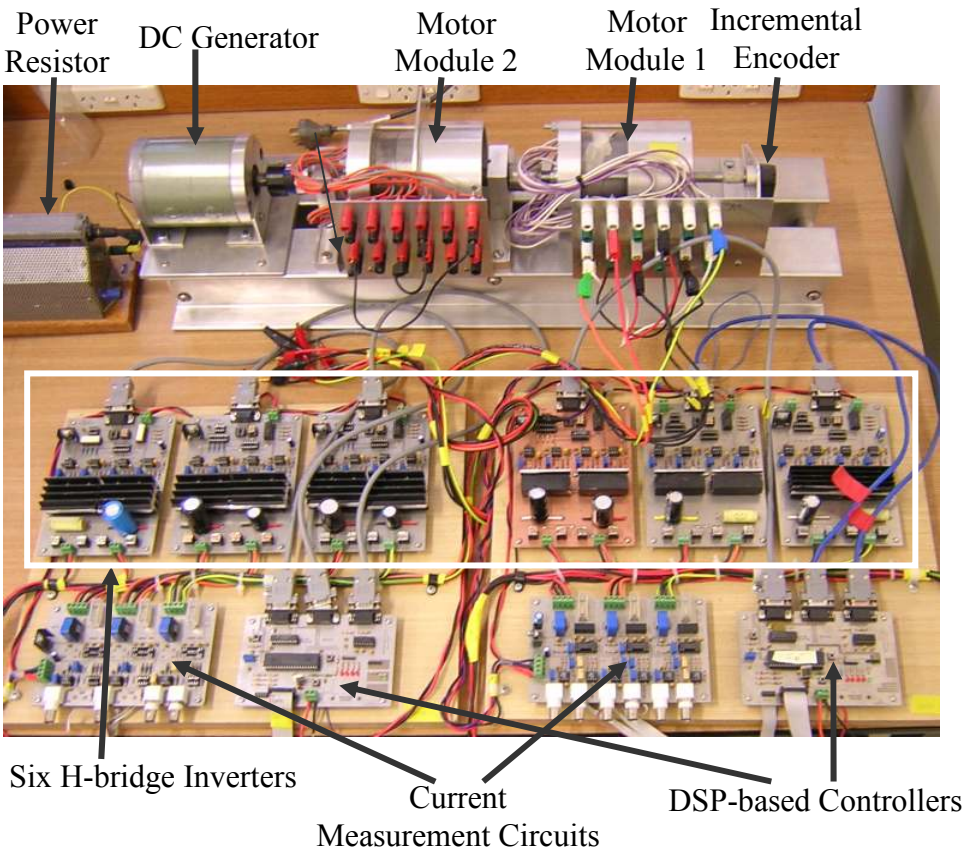

Figure 6.1 A photo of the fault-tolerant motor drive hardware

Table 6.1 shows some key parameters of the fault-tolerant PMAC motor modules in the test setup, which are utilized in the rotor position estimators.

Table 6.1 The motor parameters of the motor modules

Parameters	**Values**
Phase Resistance (R)	0.87 Ω
Phase Self Inductance (L)	2.1 mH
Back EMF Constance (k_e)	0.093 V/rad/s
Number of Pole Pairs (p)	2

As shown before, the three H-bridge type inverters are connected to a common dc input source. Each H-bridge inverter utilizes four N-channel MOSFETs (IRF540, International Rectifier) with integrated freewheeling diodes. Two types of gate drivers

(IR2121 and IR 2125) are also used in each inverter, which obtain the control signals via a four channel opto-coupler (TIL919).

The phase currents are measured by Hall-effect type current transducers, LTS 15-NP (LEM) that contain signal conditioning circuits to increase the measurement bandwidth and accuracy. The current transducers have a bandwidth of 100 kHz with a measurement accuracy of ± 0.7 % [96].

Two Microchip dsPIC30F4011 DSC controllers which are DSP-based controllers are used in the real-time motor controllers. The dsPIC30F4011 has a 16-bit modified Harvard architecture, the maximum CPU operation speed of 30MIPS, 2K data memory, 48K flash memory, and various real-time control peripheral interfaces including a 10-bit 9-channel A/D (Analog-to-Digital) converter with the maximum sampling rate of 1 MSPS, a QEI (Quadrature Encoder Interface) module, a PWM module, various DIO (Digital Input and Output) ports and two UART communication modules [97].

6.3 Data Acquisition and Data Processing

The schematic diagram shown in Figure 6.2 illustrates the measured quantities in the experimental setup. As stated previously, only one of the fault-tolerant PMAC motor modules is operated under a torque control mode and the quantities are measured simultaneously.

As shown in the figure, in order to perform the torque control of the motor drive system, the amplitude of the current command (I_m) utilized as a torque command is applied to the sinusoidal reference current generators. The sinewave generators utilize the actual mechanical rotor position (θ_r) obtained from the encoder mounted on the shaft. Each reference phase current (i_a^*, i_b^* and i_c^*) is compared with the corresponding actual phase current measured utilizing the current transducer of the current measurement circuit. Then the hysteresis current controllers produce suitable switching signals to drive the H-bridge inverter to allow the actual phase current to follow the reference phase current within the hysteresis band (Δh). The H-bridge inverters in the drive are operated by the bipolar voltage switching scheme.

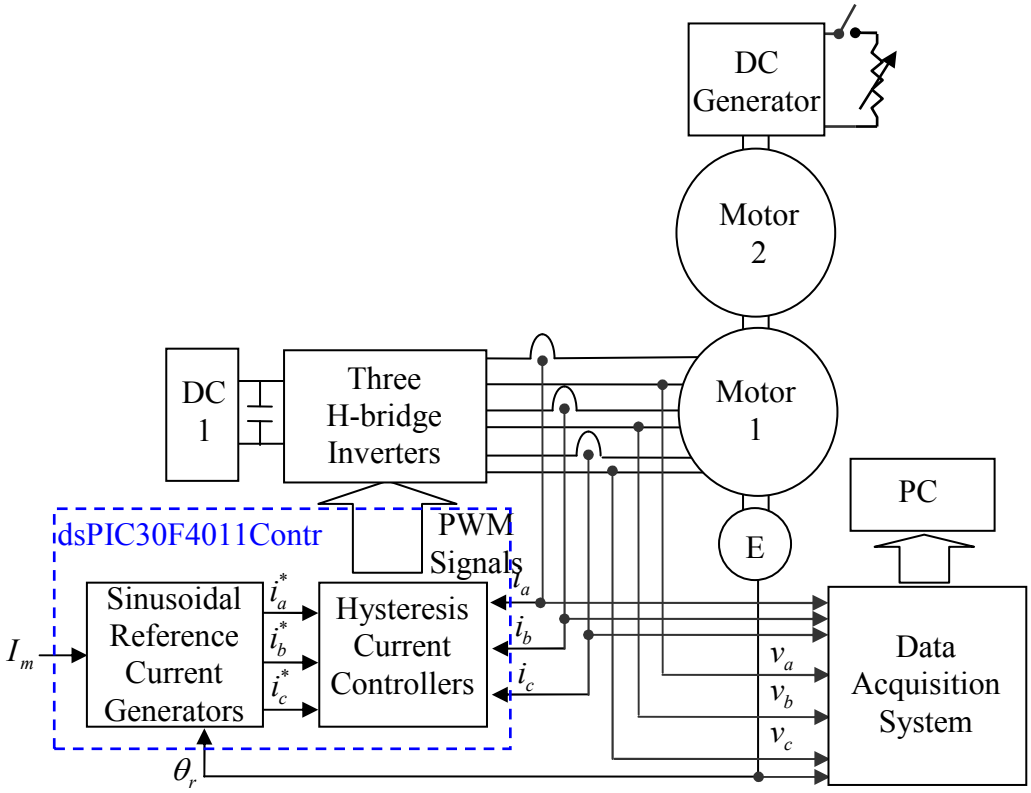

Figure 6.2 The principal block diagram of the torque control of the fault-tolerant three-phase PMAC motor drive and the data acquisition system

6.3.1 Data Acquisition System

In order to obtain the phase currents, the phase voltages and the position information (encoder pulse signals) in the motor drive, a LabVIEW-based data acquisition system is constructed which consists of both hardware and software components. The hardware components for the data acquisition includes two A/D boards (NI PCI 6110E), one DIO board (NI PCI 6534) and a PC (see Figure 6.3). The boards utilized in this study have the RTSI™ (Real-Time System Integration bus) lines connected together to synchronize the acquired data. Each A/D board can offer four different 12-bit analog input channels which can simultaneously sample at a maximum speed of 5 MS/s [98]. The DIO board is a high-speed, 32-bit, parallel, digital I/O interface to perform pattern I/O and high speed data transfer at speeds up to 80 Mbytes/s using onboard memory and is able to provide 32 individually configurable DIO lines [99, 100].

Figure 6. 3 The photo of the data acquisition system

Figure 6.4 shows the block diagram and the front panel of the developed data acquisition system VIs (Virtual Instruments). As shown in the block diagram, the graphical source code of the developed program configures the two PCI 6110E boards and the PCI 6534 to sample all the required quantities simultaneously. The sampled data is stored in a data file whose path can be set on the front panel. The time steps are also stored in μs in the data file. As seen in Figure 6.4 (b), the number of scans (samples) and the scan rate (sampling frequency) are defined by the user. In addition, the front panel presents the captured data to check its correctness.

In the hardware, 7 A/D channels are used to measure the three phase currents using three Hall-effect current transducers, the three phase voltages using the differential probes (Model 70095, Yokogawa) and the pulse train of Channel A of the encoder.

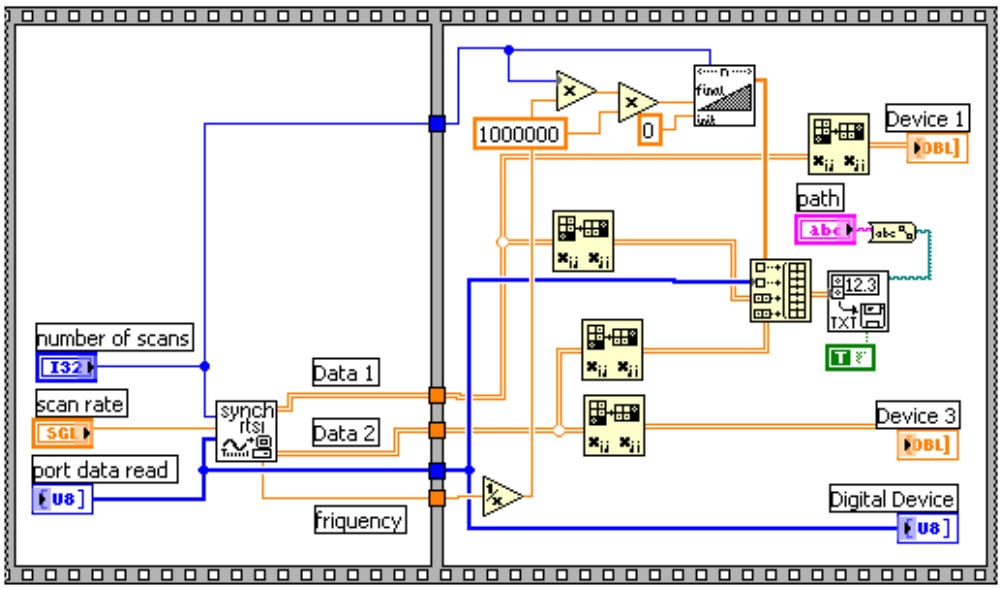

(a)

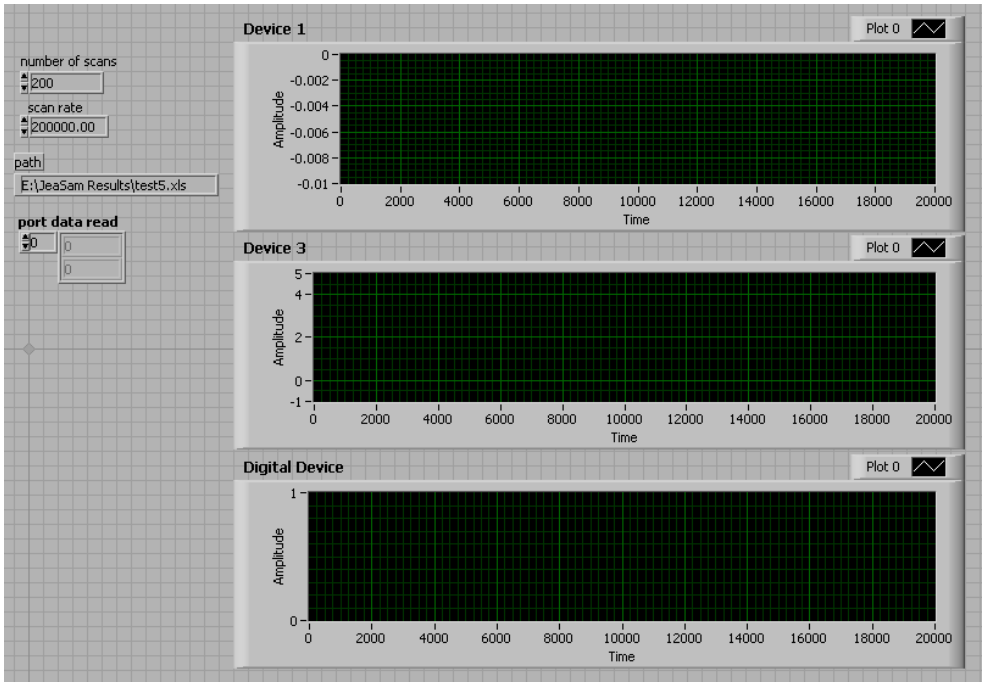

(b)

Figure 6.4 (a) The block diagram and (b) the front panel of the LabVIEW-based data acquisition system used for the real time data capturing.

6.3.2 Principles of the Real-Time Data Processing for Position Estimation

Figure 6.5 illustrates two block diagrams and the front panel of the custom-written LabVIEW files. In this study, the captured and saved data file is read and the dc offset is

removed (Figure 6.5 (a)). Then the data is multiplied by the correct gains to obtain the actual values of the phase currents and the voltages to be utilized in the position estimators. In addition, the unit of the time information is also converted from microseconds to milliseconds.

Figure 6.5 (b) illustrates the block diagram of the two-phase and the three-phase position estimators and the estimator for the actual electrical rotor position based on the encoder signal. The block diagram has five parts as highlighted by the dashed boxes in the figure. Part 1 calculates the three-phase flux linkages as expressed in Section 5.2 utilizing the phase currents, phase voltages, sampling time (10 us) and using the motor parameters. The section also utilizes the initial phase currents.

In Part 2 the two-phase position estimation method is implemented as given in Section 5.2. This part utilizes the phase flux linkage increments obtained in Part 1. The three rotor position estimates using the three pairs of phases are also calculated in this part. Similarly, the three-phase position estimation method proposed in Section 5.3 is implemented to obtain a single rotor position estimate in Part 3 where the proportional gain was set to 1 in the PLL.

To obtain the actual rotor position, Part 4 counts the rising edges of the Channel A encoder signal. The initial position value was obtained from the actual winding current waveform in phase A since this current is controlled to be in phase with the back EMF of the same phase by the real time controllers [14].

Finally, Part 5 calculates the position estimation errors that are used to determine the accuracy of the position estimators.

The front panel in Figure 5 (c) controls the path of the captured data file and displays the analysis results obtained from the real off-line data. The data graphed by this panel can also be transformed to Matlab for plotting.

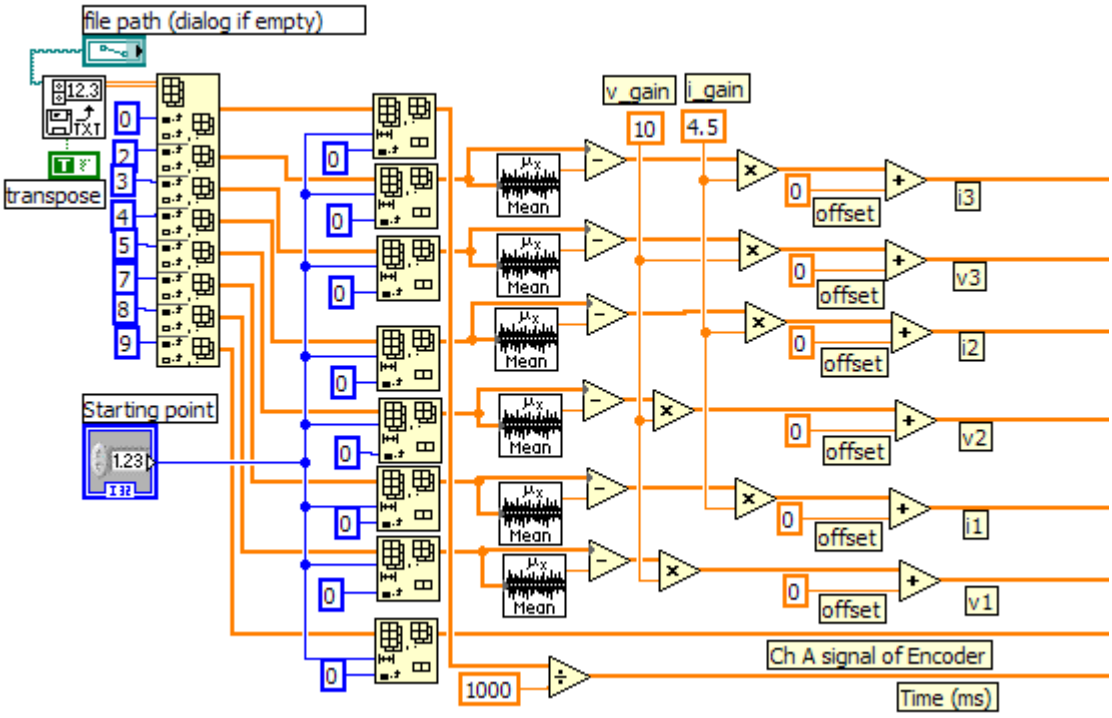
file path (dialog if empty)
transpose
Starting point
v_gain
i_gain
10
4.5
Mean
offset
i3
v3
i2
v2
i1
v1
1000
Ch A signal of Encoder
Time (ms)

(a)

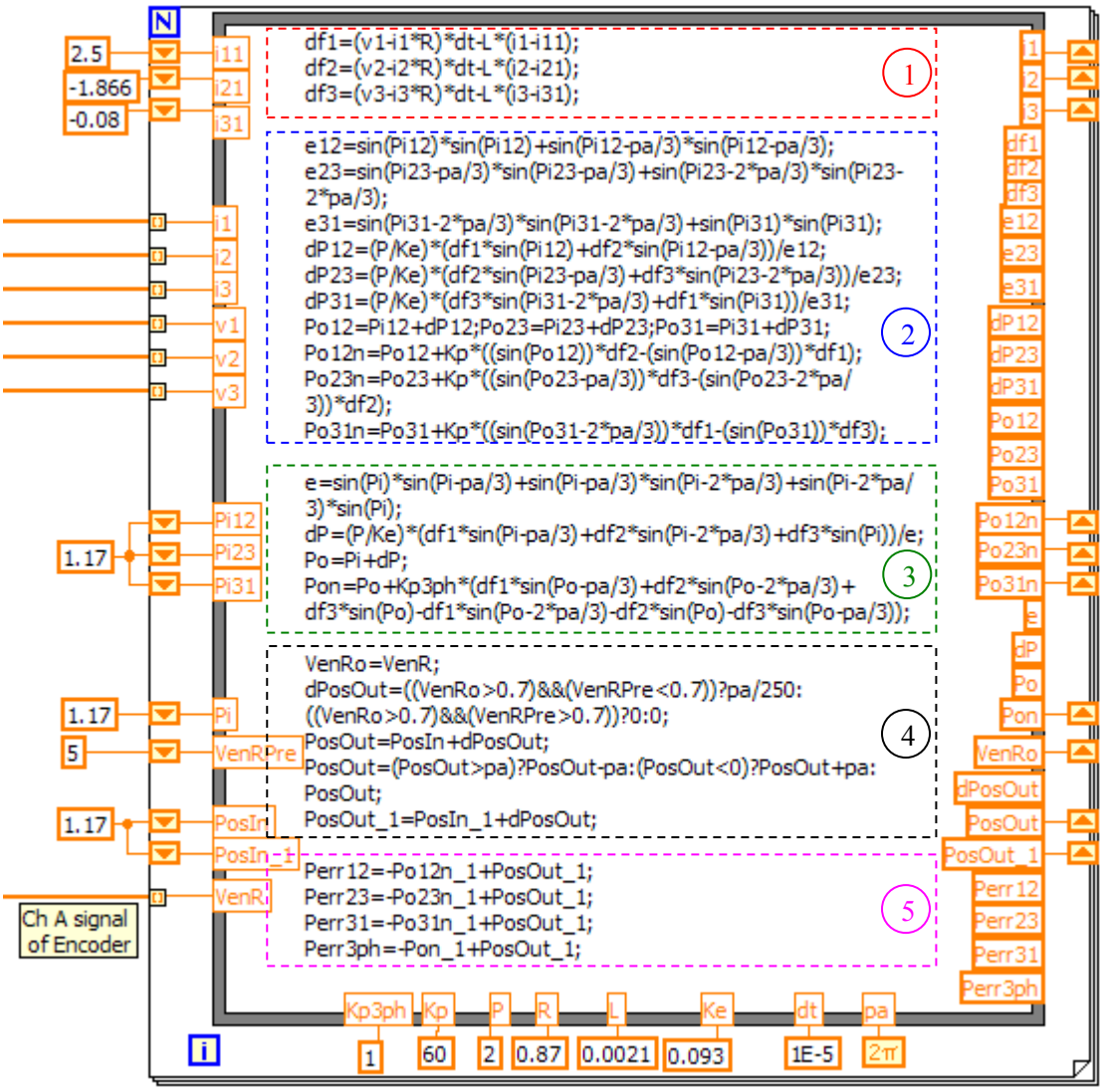
df1=(v1-i1*R)*dt-L*(i1-i11);
df2=(v2-i2*R)*dt-L*(i2-i21);
df3=(v3-i3*R)*dt-L*(i3-i31);
1
e12=sin(Pi12)*sin(Pi12)+sin(Pi12-pa/3)*sin(Pi12-pa/3);
e23=sin(Pi23-pa/3)*sin(Pi23-pa/3)+sin(Pi23-2*pa/3)*sin(Pi23-2*pa/3);
e31=sin(Pi31-2*pa/3)*sin(Pi31-2*pa/3)+sin(Pi31)*sin(Pi31);
dP12=(P/Ke)*(df1*sin(Pi12)+df2*sin(Pi12-pa/3))/e12;
dP23=(P/Ke)*(df2*sin(Pi23-pa/3)+df3*sin(Pi23-2*pa/3))/e23;
dP31=(P/Ke)*(df3*sin(Pi31-2*pa/3)+df1*sin(Pi31))/e31;
Po12=Pi12+dP12;Po23=Pi23+dP23;Po31=Pi31+dP31;
Po12n=Po12+Kp*((sin(Po12))*df2-(sin(Po12-pa/3))*df1);
Po23n=Po23+Kp*((sin(Po23-pa/3))*df3-(sin(Po23-2*pa/3))*df2);
Po31n=Po31+Kp*((sin(Po31-2*pa/3))*df1-(sin(Po31))*df3);
2
e=sin(Pi)*sin(Pi-pa/3)+sin(Pi-pa/3)*sin(Pi-2*pa/3)+sin(Pi-2*pa/3)*sin(Pi);
dP=(P/Ke)*(df1*sin(Pi-pa/3)+df2*sin(Pi-2*pa/3)+df3*sin(Pi))/e;
Po=Pi+dP;
Pon=Po+Kp3ph*(df1*sin(Po-pa/3)+df2*sin(Po-2*pa/3)+df3*sin(Po)-df1*sin(Po-2*pa/3)-df2*sin(Po)-df3*sin(Po-pa/3));
3
VenRo=VenR;
dPosOut=((VenRo>0.7)&&(VenRPre<0.7))?pa/250:((VenRo>0.7)&&(VenRPre>0.7))?0:0;
PosOut=PosIn+dPosOut;
PosOut=(PosOut>pa)?PosOut-pa:(PosOut<0)?PosOut+pa:PosOut;
PosOut_1=PosIn_1+dPosOut;
4
Perr12=-Po12n_1+PosOut_1;
Perr23=-Po23n_1+PosOut_1;
Perr31=-Po31n_1+PosOut_1;
Perr3ph=-Pon_1+PosOut_1;
5
2.5
-1.866
-0.08
i11
i21
i31
i1
i2
i3
v1
v2
v3
1.17
Pi12
Pi23
Pi31
1.17
5
Pi
VenRPre
1.17
PosIn
PosIn_1
VenR
Ch A signal of Encoder
Kp3ph
Kp
P
R
L
Ke
dt
pa
1
60
2
0.87
0.0021
0.093
1E-5
2π
i
1
2
3
df1
df2
df3
e12
e23
e31
dP12
dP23
dP31
Po12
Po23
Po31
Po12n
Po23n
Po31n
e
dP
Po
Pon
VenRo
dPosOut
PosOut
PosOut_1
Perr12
Perr23
Perr31
Perr3ph

(b)

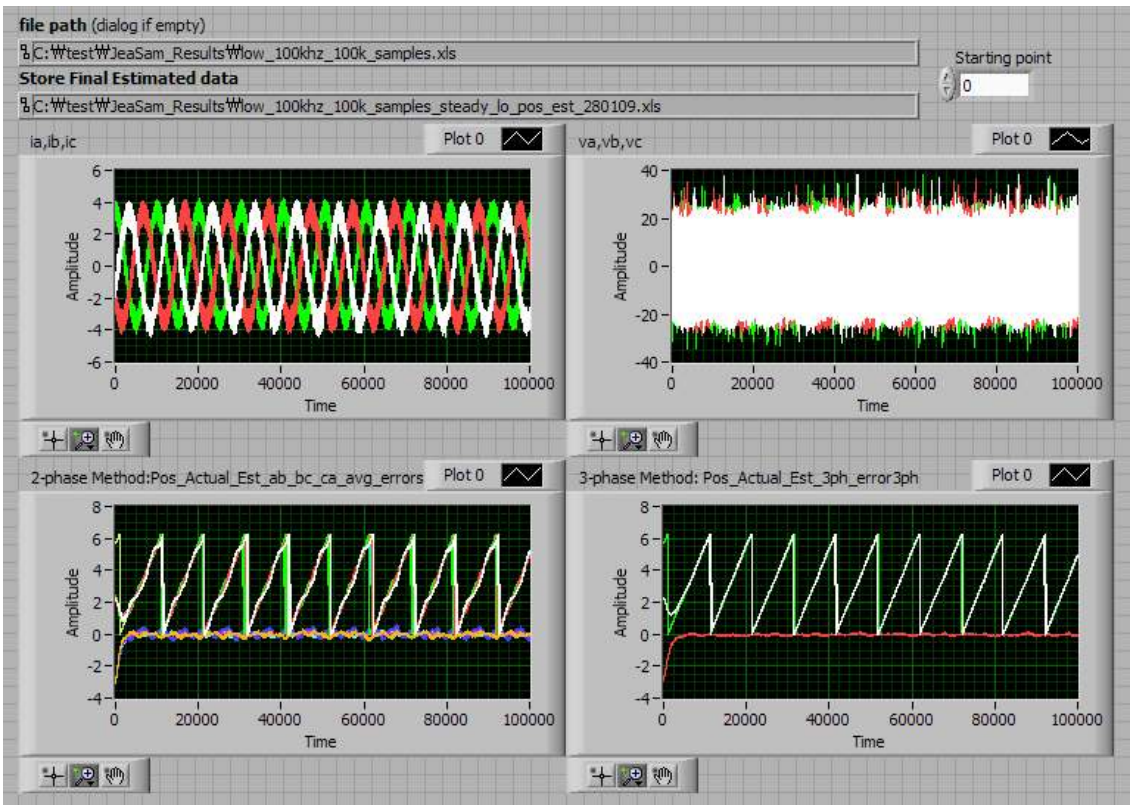

(c)

Figure 6.5 The block diagrams ((a) and (b)), and (c) the front panel of the custom LabVIEW VIs of the two-phase and the three-phase position estimation methods.

6.4 Experimental Results

In order to validate the feasibility of the developed position estimation techniques, extensive experimental tests were performed under various operating conditions. The operating conditions included steady-state operation at low and high speeds, parameter changes, measurement errors, dynamic operation including starting from standstill and step load changes, and operation under faults (one phase winding open-circuit and a single current or single voltage sensor failure).

During the tests the amplitude of the reference current was set to 3.5A, the hysteresis bandwidth of the hysteresis current controllers was 0.8A, the DC link power supply voltage of the inverters was 20V, and the sampling frequency in the data acquisition system was 100 kHz.

The resistive load (13.5 Ω) was not connected to the DC generator during the starting from standstill test or during the steady-state tests at 2100 rpm including the

one-phase winding open-circuit condition. However, the load was connected under the steady-state speed test at 300 rpm. To conduct the step load changes on the motor drive, the load was removed or added during operation.

Note that in the captions of the figures illustrating the results of the off-line real data i_a, i_b and i_c represent the measured phase currents, v_a, v_b and v_c are the measured phase voltages, θ_{actual} indicates the actual electrical rotor position in the motor module 1. In the two-phase sensorless position estimation method, θ_{ab}, θ_{bc} and θ_{ca} denote the electrical rotor position estimates obtained from the phases A-B, B-C and C-A; ε_{ab}, ε_{bc} and ε_{ca} are the position estimation errors obtained from phases A-B, B-C and C-A, θ_{2ph} and ε_{2ph} represent the electrical rotor position estimate and the estimation error of the motor module 1 respectively. In the three-phase position estimation method, θ_{3ph} and ε_{3ph} represent the electrical rotor position estimates and the estimation error of motor module 1 respectively.

6.4.1 Steady-State Test Results

To examine the steady-state performance of the proposed indirect position estimation methods under low speed operation (300 rpm), a set of results are given in Figure 6. 6. In this test, while the motor was operating at 300 rpm, it was loaded by the resistor load connected to the DC generator.

As it can be seen in the figure, in this mode of operation the measured phase currents (i_a, i_b, i_c) present sinusoidal waveforms controlled within a hysteresis bandwidth of 0.8 A and the measured phase voltages (v_a, v_b, v_c) varies between the dc link voltage ± 20 V. Figure 6.6 also shows the three rotor position estimates (θ_{ab}, θ_{bc} and θ_{ca}), the corresponding estimation errors (ε_{ab}, ε_{bc}, ε_{ca}), an averaged rotor position estimate (θ_{2ph}) and its estimation error (ε_{2ph}) obtained from the two-phase position estimation technique in the motor module 1. In addition, the rotor position estimate (θ_{3ph}) and its estimation error (ε_{3ph}) for the motor module 1 are given by the three-phase position estimation method and the actual rotor position (θ_{act}) is also presented in the same figure.

The shape of the waveforms obtained with offline voltage-current data (Figure 6.6) matches well with those obtained previously with simulated data (Figure 5.4). The measured current ripple is somewhat larger than predicted however this could be due to measurement noise. It can also be seen that with simulated data, the position errors for the three two-phase estimates are similar while with offline data there are significant differences between the phases with the a-b result showing the largest errors. This is likely to be due to differences in the motor parameters or sensor errors between the phases.

The three two-phase rotor position estimates were averaged to obtain a better accurate final rotor position estimate as observed in Figure 6.6. As was seen with the simulated data, the rotor position estimate obtained with the three-phase position estimation method had a smaller RMS estimation error of 0.11 rads than the two-phase position estimation method whose RMS error value was 0.150 rads.

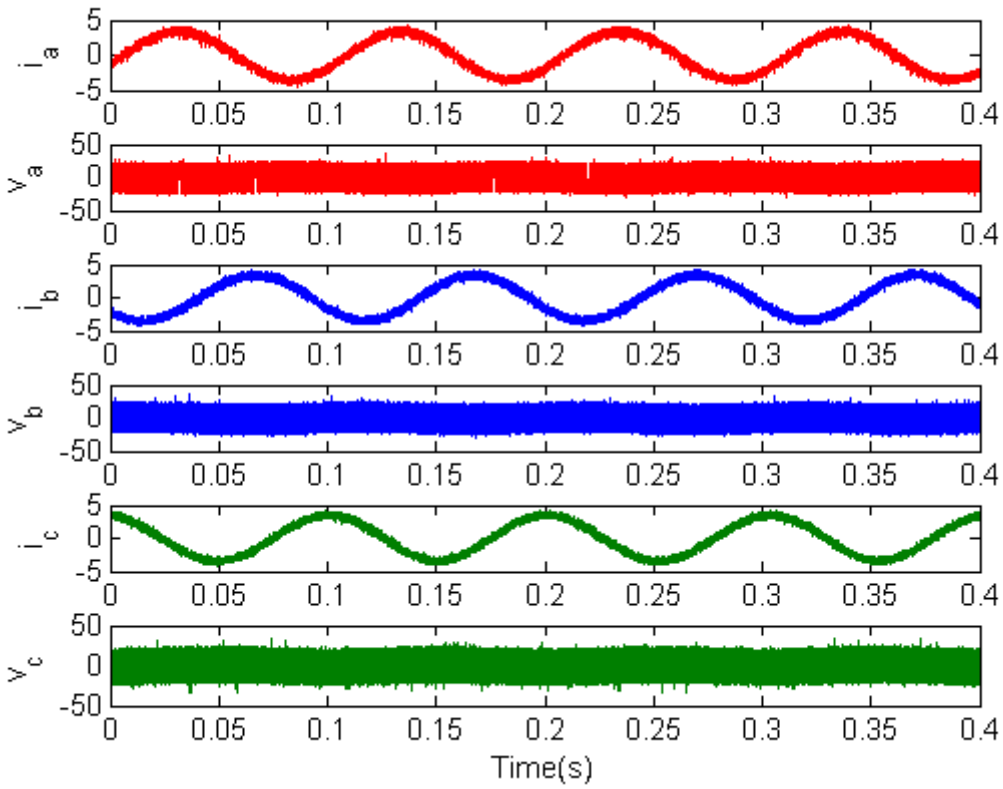

(a)

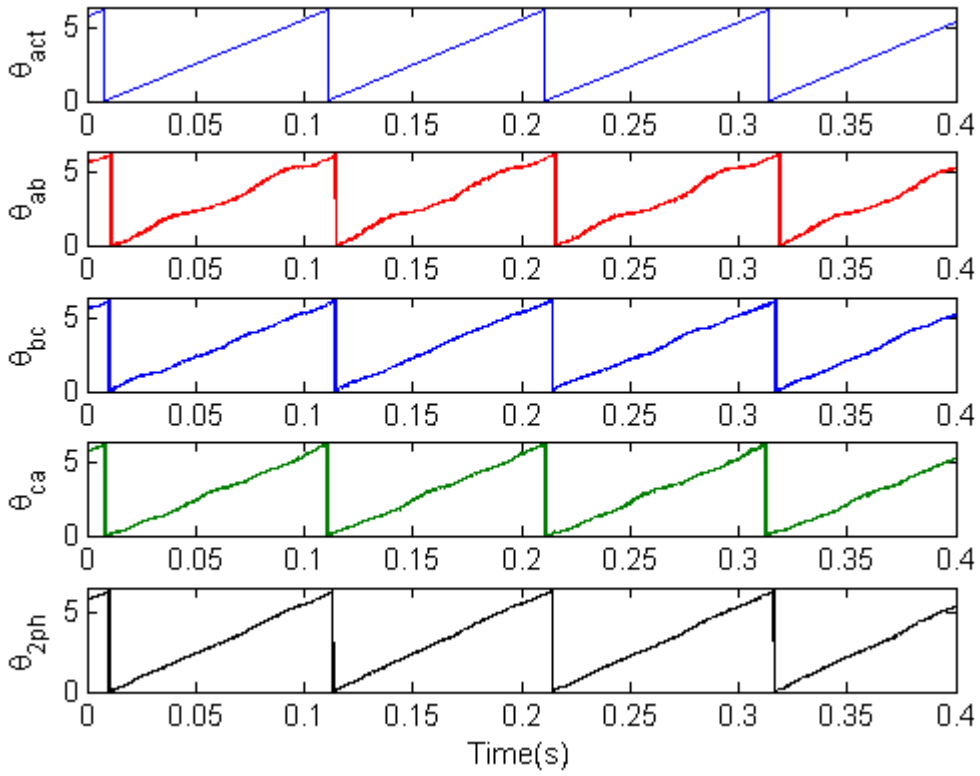
θact
θab
θbc
θca
θ2ph
5
0
0.05
0.1
0.15
0.2
0.25
0.3
0.35
0.4
Time(s)

(b)

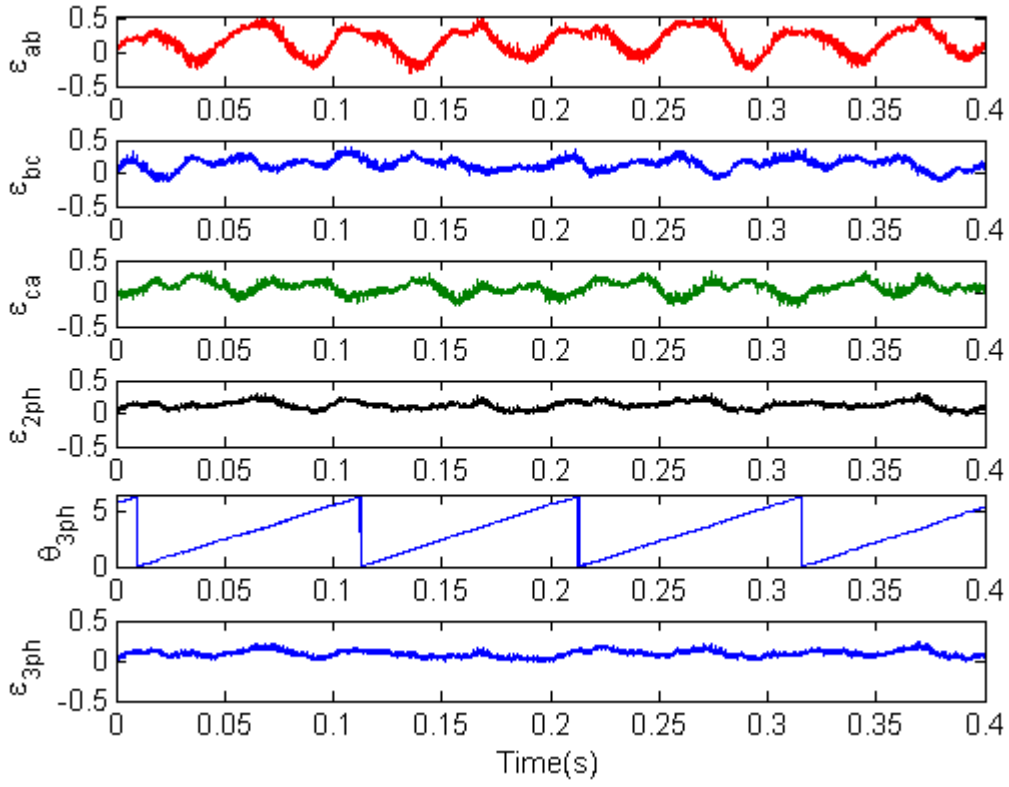
εab
εbc
εca
ε2ph
θ3ph
ε3ph
0.5
0
-0.5
5
0
0.05
0.1
0.15
0.2
0.25
0.3
0.35
0.4
Time(s)

(c)

Figure 6.6 Steady-state test results of the motor drive 1 at a low speed of 300 rpm from the top: (a) phase currents and voltages (b) actual and estimated rotor positions (c) 3ph estimated rotor position and position errors

The high speed (2100 rpm) steady-state test results are given in Figure 6.7. In this mode of operation the resistive load is not connected to the generator to reduce the load torque hence to increase the speed of the motor.

The offline test waveforms show a good correspondence with the results with simulated voltage-current data as seen previously in Figure 5.5. In particular the distortion in the phase current due to the high back-emf voltages is predicted accurately..

As previously presented in the computer simulation results of Figure 5.5, the offline results in Figure 6.7 illustrate that the position estimates obtained using both methods have better accuracy than the low speed results. It was also found that the three-phase position estimation method had better accuracy than the two-phase position estimation method where the RMS estimation errors were 0.019 and 0.022 rads respectively as seen in Table 6.2. However, the offline estimation errors are generally two to three times larger than those obtained under the previous computer simulation test. This is likely to be due to practical factors such as measurement errors or inaccurate parameters.

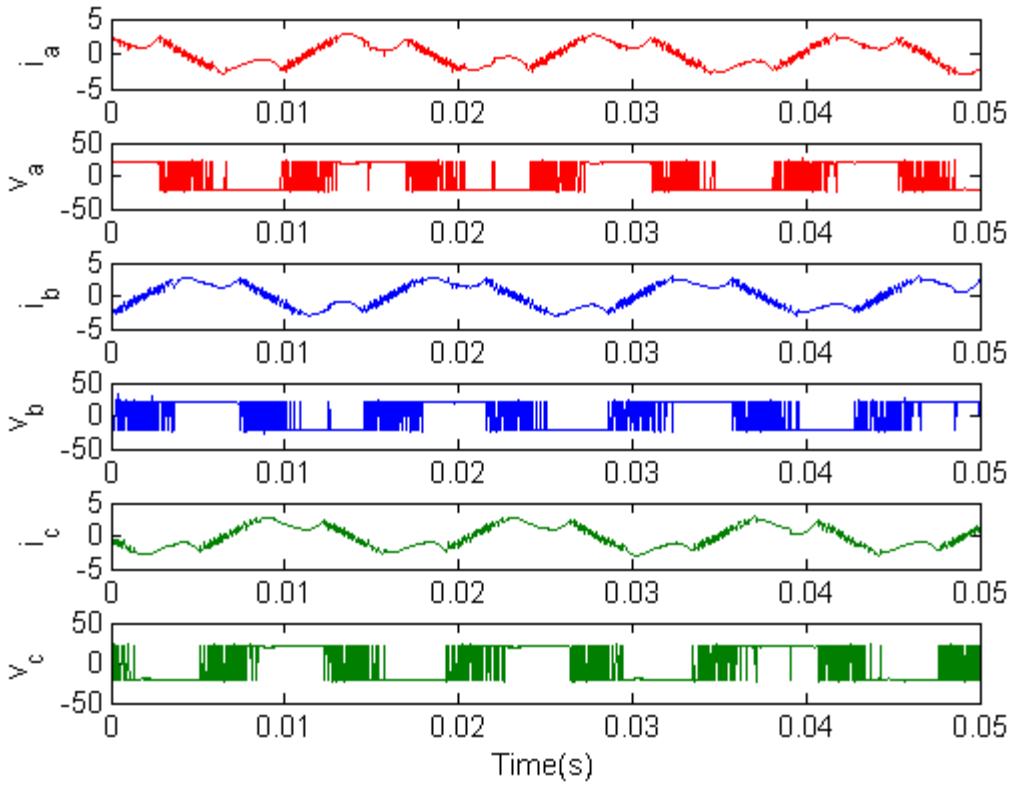
i_a
v_a
i_b
v_b
i_c
v_c
5
0
-5
50
-50
0.01
0.02
0.03
0.04
0.05
Time(s)

(a)

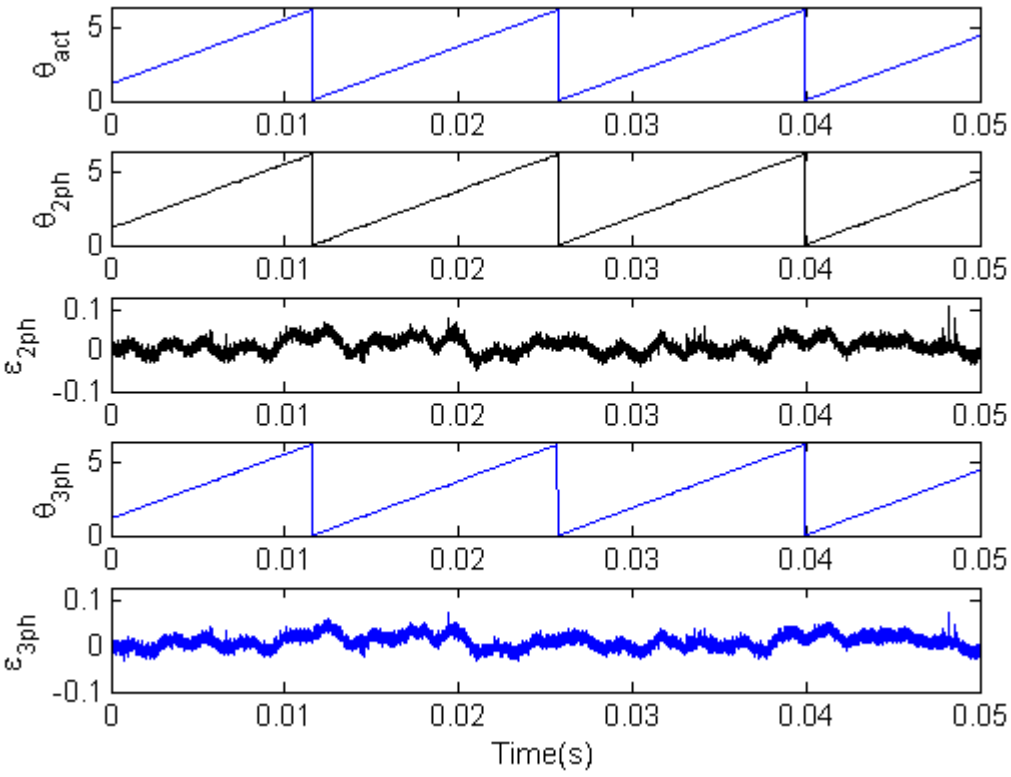
θ_act
θ_2ph
ε_2ph
θ_3ph
ε_3ph
5
0
0.1
-0.1
0.01
0.02
0.03
0.04
0.05
Time(s)

(b)

Figure 6.7 Steady-state performance of the motor drive 1 at high speed operation (2100 rpm). From the top: (a) i_a, v_a, i_b, v_b, i_c, v_c, (b) θ_{act}, θ_{2ph}, ε_{2ph}, θ_{3ph}, ε_{3ph}.

Table 6.2 RMS position estimation error in computer simulation and offline tests under low and high speed steady-state operation

		RMS Position Estimation Error (rad)	
		Two-Phase Method	Three-Phase Method
Low-Speed	Phase a-b: sim/offline	0.0551/0.261	
	Phase b-c: sim/offline	0.0594/0.171	
	Phase c-a: sim/offline	0.0657/0.130	
	Total: sim/offline	0.0434/0.150	0.0362/0.110
High-Speed	Total: sim/offline	0.0098/0.0221	0.008/0.0193

Effect of Incorrect Initial Rotor Position under Steady-State Operation

To study the effect of an incorrect initial rotor position data in the estimators, a test was also performed using the off-line data obtained in Figure 6.6. An initial rotor position error of 2.5 radians was introduced to the original initial rotor position and the results are given in Figure 6.8. As it can be seen in the figure, the initial phase differences of the position estimates obtained in both methods were compensated in the first electrical cycle due to the PLL method adopted in the sensorless algorithms. The results are similar to those obtained using simulated data which were shown earlier in Figure 5.6. After the error was compensated for by the PLL method, the rms error was comparable to that obtained previously in the steady-state simulation.

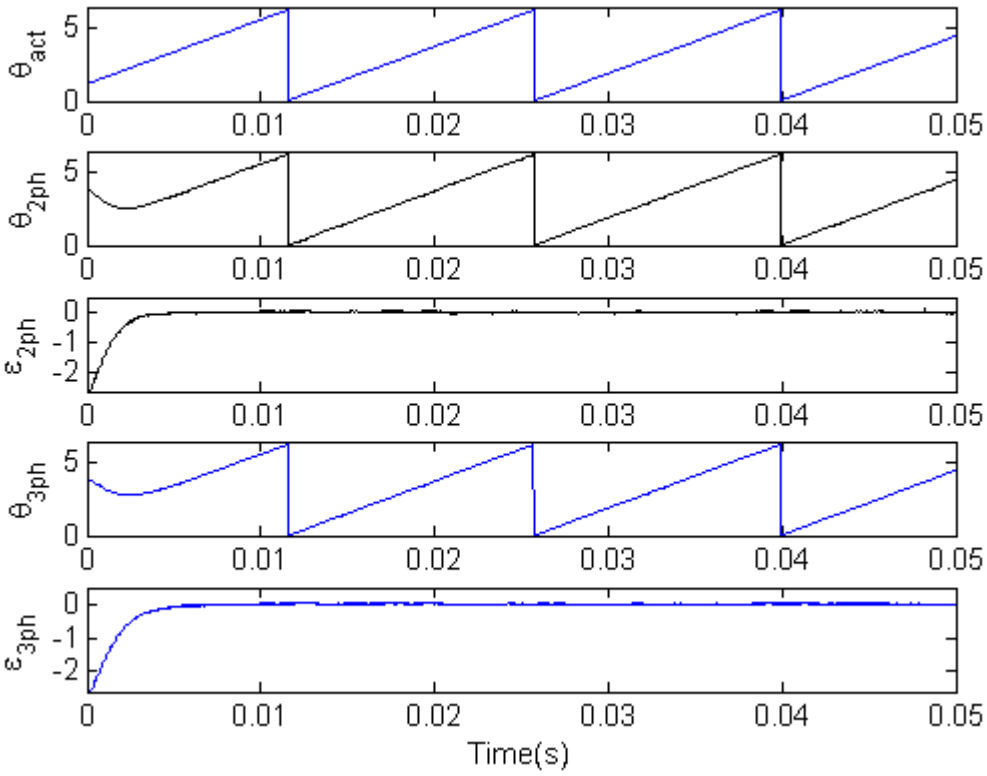

Figure 6.8 Performance of motor drive 1 at 2100 rpm while starting with an incorrect initial rotor position.

Parameter Variations and Measurement Errors

To investigate the robustness of the proposed estimation methods under parameter variations and measurement errors, an extensive number of tests were also performed at a constant speed of 2,100 rpm. In these tests, the phase resistances, the phase inductances and the back EMF constant used in the estimator were varied by ±30% with respect to their original values. Figure 6.9 and Table 6.3 illustrate the position estimation errors obtained using the two proposed position estimation methods. It is concluded that both methods have robustness against the parameter variations where the most critical parameter is the back-EMF constant errors and where the phase resistance errors produce the smallest resultant position estimation errors. These observations match those found in the previous computer simulation tests shown in Figure 5.7. The position estimation errors with the offline test data are generally between 0 to 50% larger than those with the simulated data.

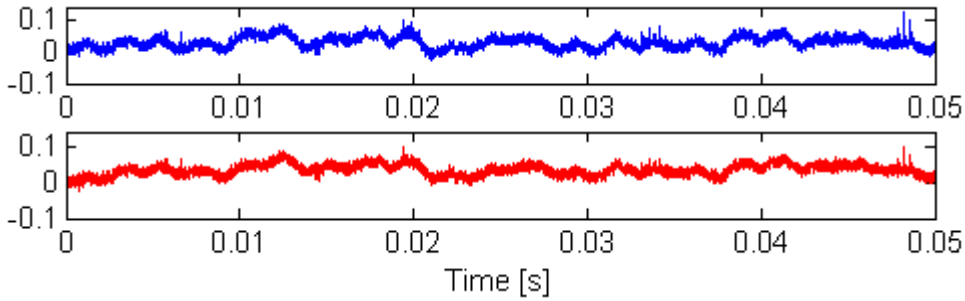

(a) +30 % resistances ($1.3 \times R$)

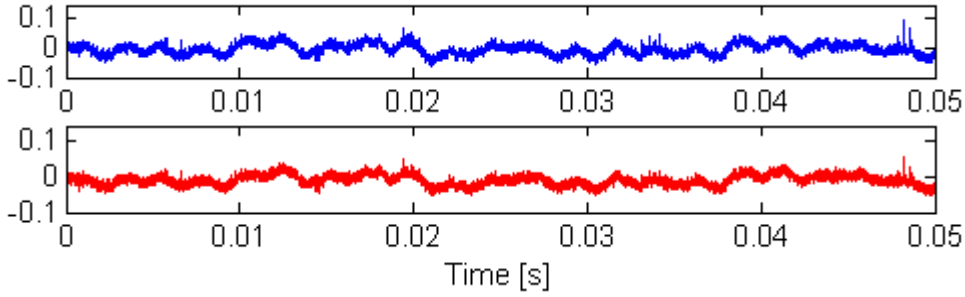

(b) -30 % resistances ($0.7 \times R$)

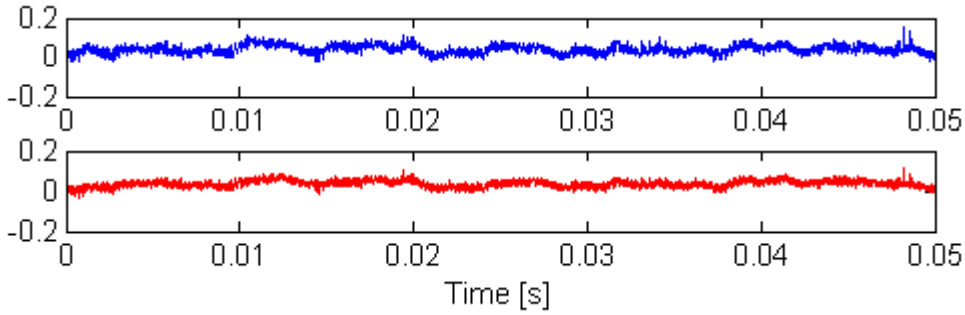

(c) +30 % inductances ($1.3 \times L$)

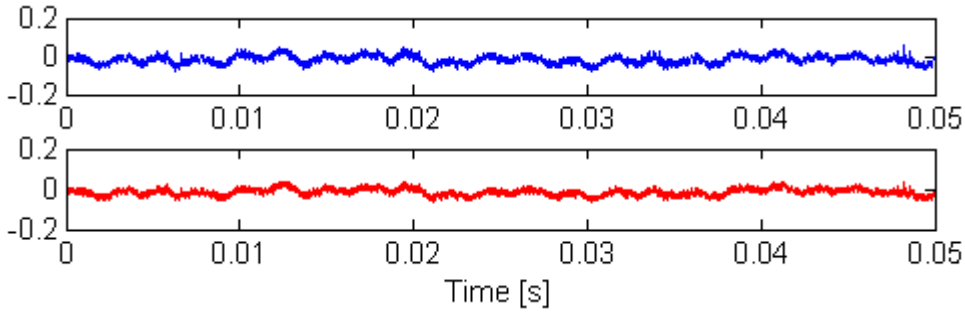

(d) -30 % inductances ($0.7 \times L$)

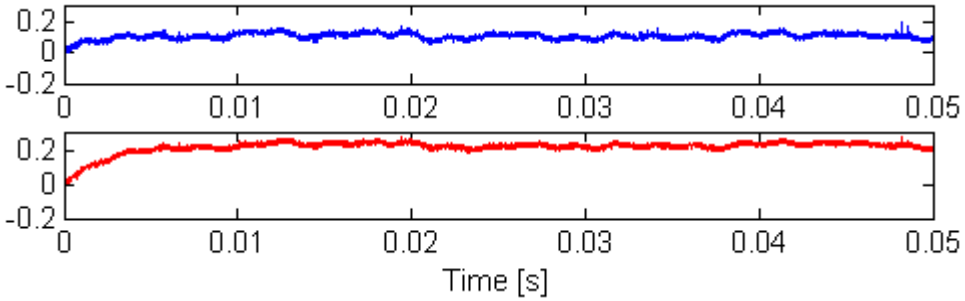

(e) +30 % back EMF constants ($1.3 \times k_e$)

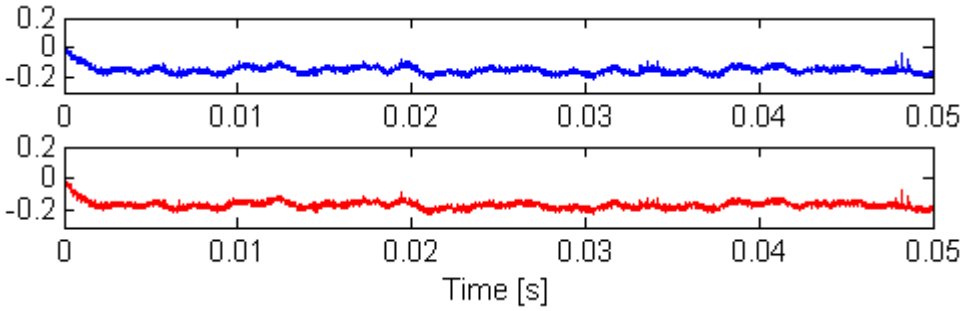

(f) -30 % back EMF constants ($0.7 \times k_e$)

Figure 6.9 Steady-state performance of the position estimators at 2100 rpm for the different motor parameters: ε_{2ph}, ε_{3ph}.

Table 6.3 RMS position estimation error in computer simulation and offline tests under parameter variations

	RMS Position Estimation Error (rad)	
	Two-Phase Method	Three-Phase Method
No Parameter Errors: sim/offline	0.0098/0.0221	0.008/0.0193
Resistance ±30%: sim/offline	0.0186/0.0276	0.0212/0.0292
Inductance±30%: sim/offline	0.03425/0.037	0.0336/0.0327
Back-EMF Constant ±30%: sim/offline	0.133/0.135	0.160/0.200

Figure 6.10 and Table 6.4 present the position estimation errors obtained under inaccurate measurements during high speed operation (2,100 rpm). In this test, the gains of the measured quantities (voltage and current) were varied within ±10 % of their original values. In addition, the offsets of the current sensors were set to ± 0.3 A and the voltage sensor offsets were ± 2 V. As already found in the simulation studies seen in Figure 5.8 and Table 5.5, it can be observed from the test results of Figure 6.10 that errors in the gain generate larger estimation errors than in the case of the offset errors in each sensor for both methods. Particularly, the voltage sensor gain errors are the most serious factor. In addition, the three-phase method is almost insensitive to the offset errors of both sensors. However, the two-phase method is more sensitive in the voltage sensor offset errors than the current sensor offset errors. Furthermore, the current offset error produces the least estimation errors in both techniques. This is likely to be due to the offset errors not affecting the incremental current value in Equation (5.1).

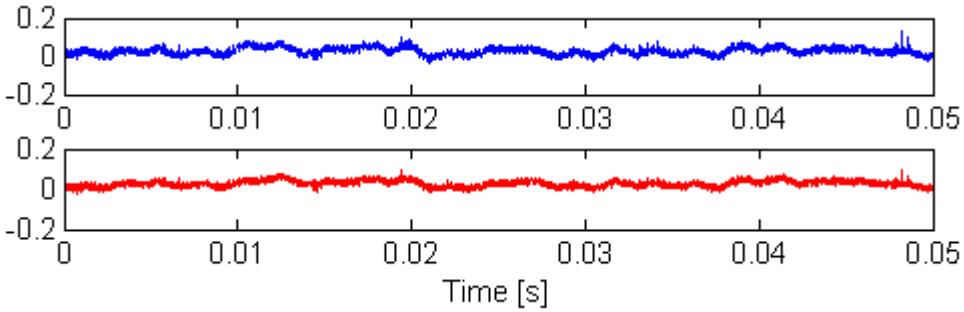

(a) +10 % current sensor gains ($1.1 \times k_i$)

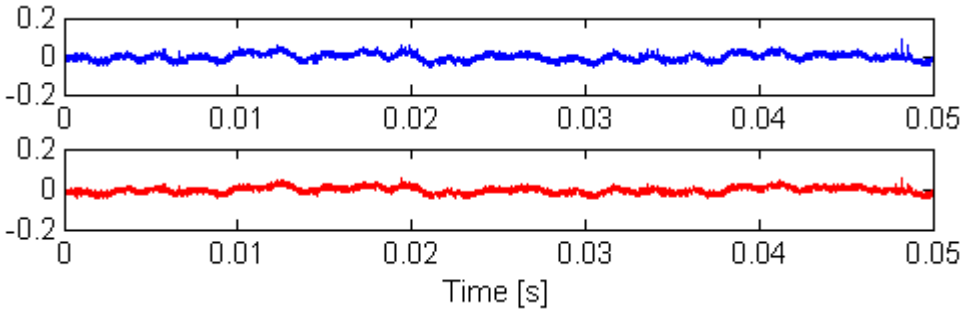

(b) -10 % current sensor gains ($0.9 \times k_i$)

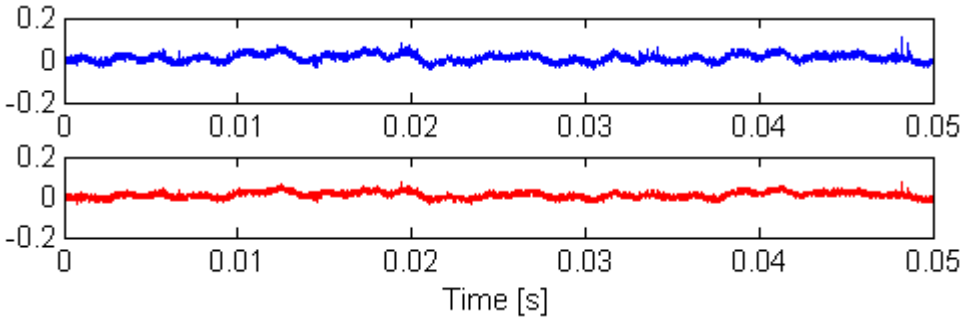

(c) +0.3A current sensor offsets

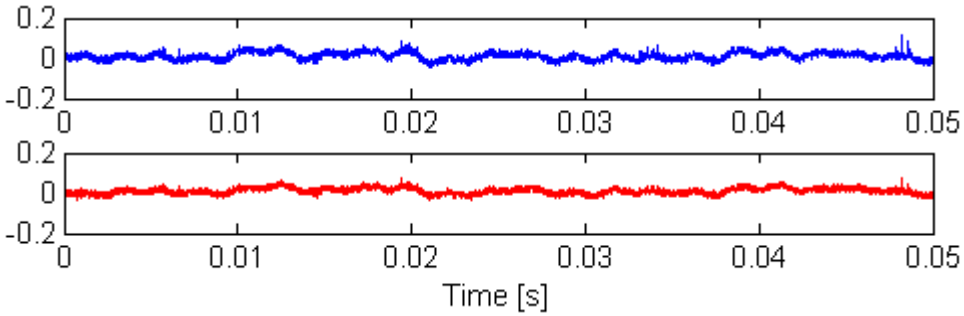

(d) -0.3A current sensor offsets

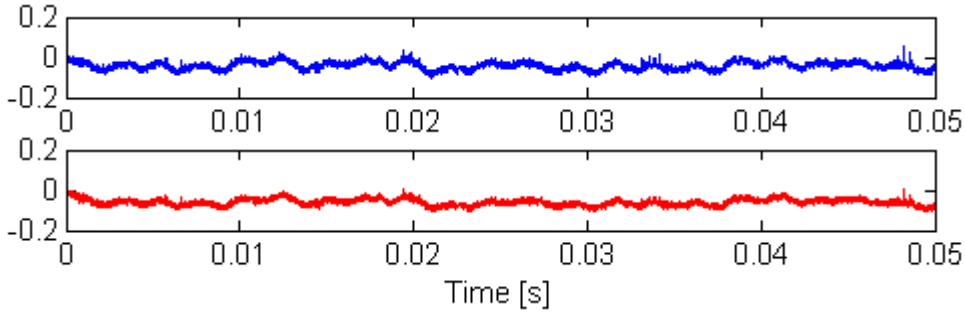

(e) +10 % voltage sensor gains ($1.1 \times k_v$)

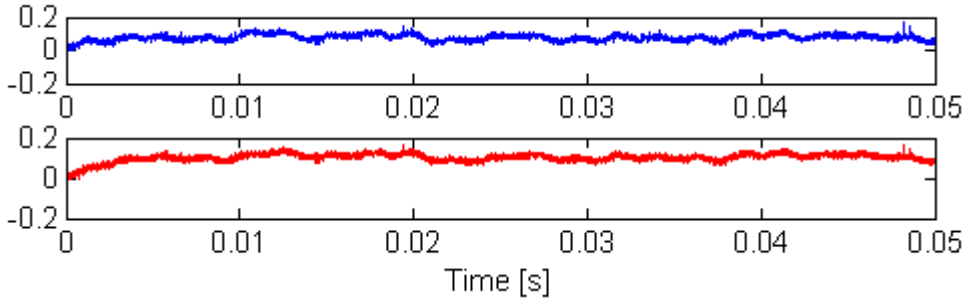

(f) -10 % voltage sensor gains ($0.9 \times k_v$)

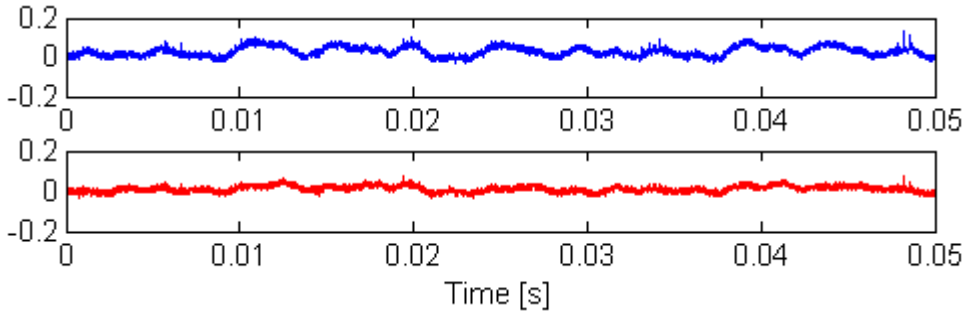

(g) +2V voltage sensor offsets

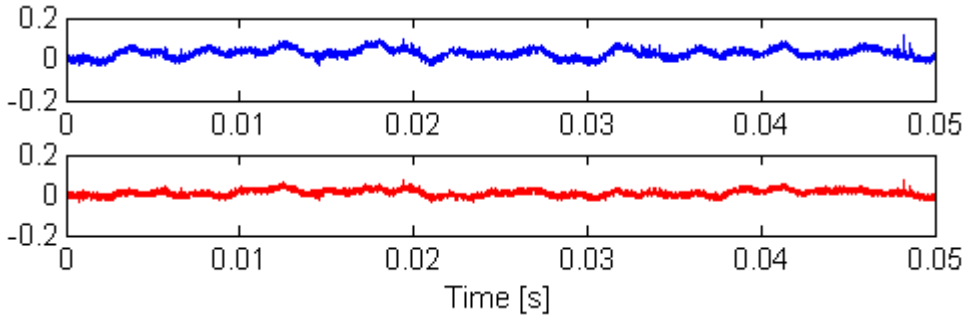

(h) -2V voltage sensor offsets

Figure 6.10 Steady-state test results at 2100 rpm and under measurement errors. From the top: ε_{2ph}, ε_{3ph} for each test case.

Table 6.4 RMS position estimation error in computer simulation and offline tests under inaccurate measurements

		RMS Position Estimation Error (rad)	
		Two-Phase Method	Three-Phase Method
No Measurement Errors: sim/offline		0.0098/0.0221	0.008/0.0193
Current Sensor	Gain ±10%: sim/offline	0.0188/0.0267	0.0191/0.0249
	Offset ±0.3A: sim/offline	0.00995/0.0223	0.008/0.0193
Voltage Sensor	Gain ±10%: sim/offline	0.0586/0.0632	0.0717/0.0845
	Offset ±2V: sim/offline	0.0203/0.037	0.008/0.0193

6.4.2 Dynamic-State Operation

In order to examine the dynamic operation performance of the position estimation methods for the fault-tolerant PMAC motor drive, several experimental tests were also done when starting from standstill and under step load changes. In the starting test, the effect of the incorrect initial rotor position value was also examined. In the results, the measured phase currents, the phase voltages, the actual rotor position, the position estimates and the position errors are given for both position estimation methods.

Figure 6.11 shows a set of test results obtained from motor module 1 during the starting of the motor drive. This test was initiated by tuning on the DC link voltage supply of the inverter. The results in Figure 6.11 illustrate the phase current waveforms and the corresponding voltage waveforms of all three phases of the motor module 1. As can be seen in the figure, although the position estimation errors are larger initially, they are compensated quickly within the first electrical cycle due to the automatic correction capabilities in both techniques. These large errors were not seen when using the simulated voltage-current data in Figure 5.9 though the high-speed steady-state performance is more comparable. A possible reason for this is that the algorithms are more sensitive to parameter and measurement errors at low speeds.

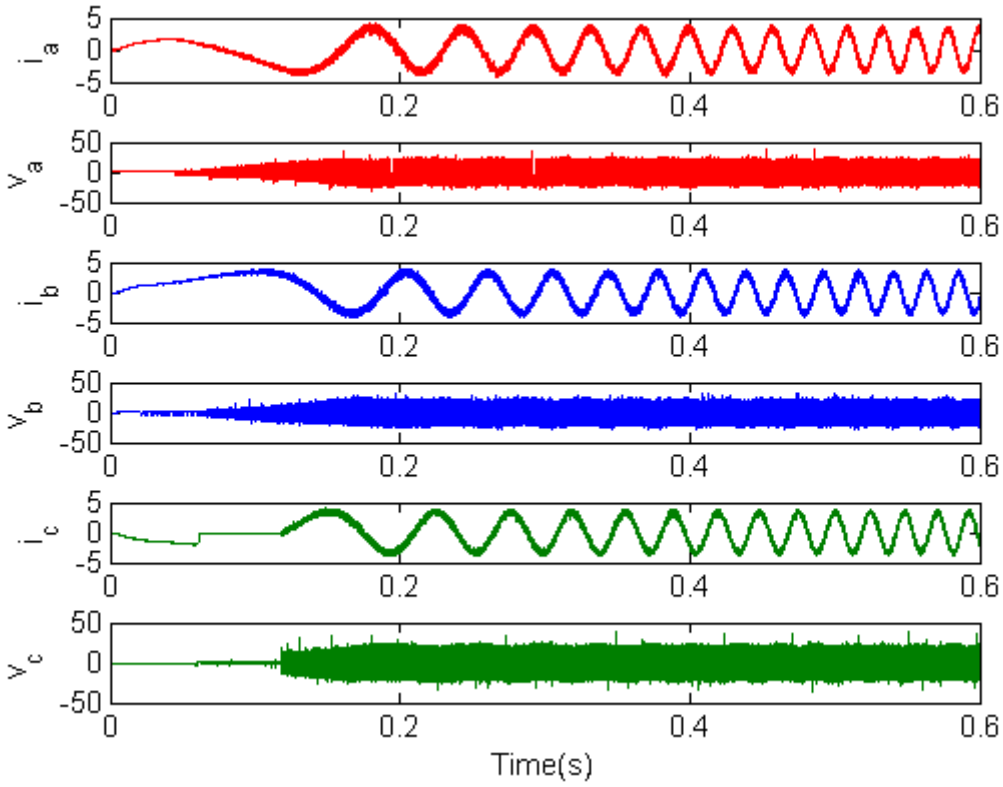
i_a
v_a
i_b
v_b
i_c
v_c
5
0
-5
50
-50
0
0.2
0.4
0.6
Time(s)

(a)

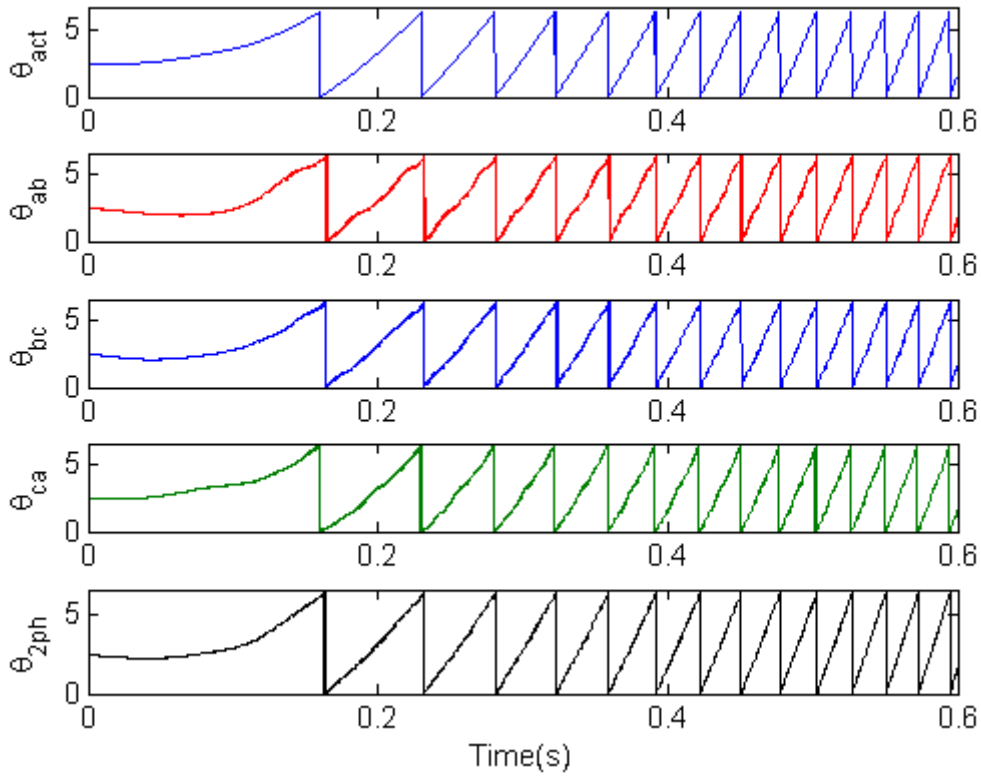
θ_{act}
θ_{ab}
θ_{bc}
θ_{ca}
θ_{2ph}
5
0
0
0.2
0.4
0.6
Time(s)

(b)

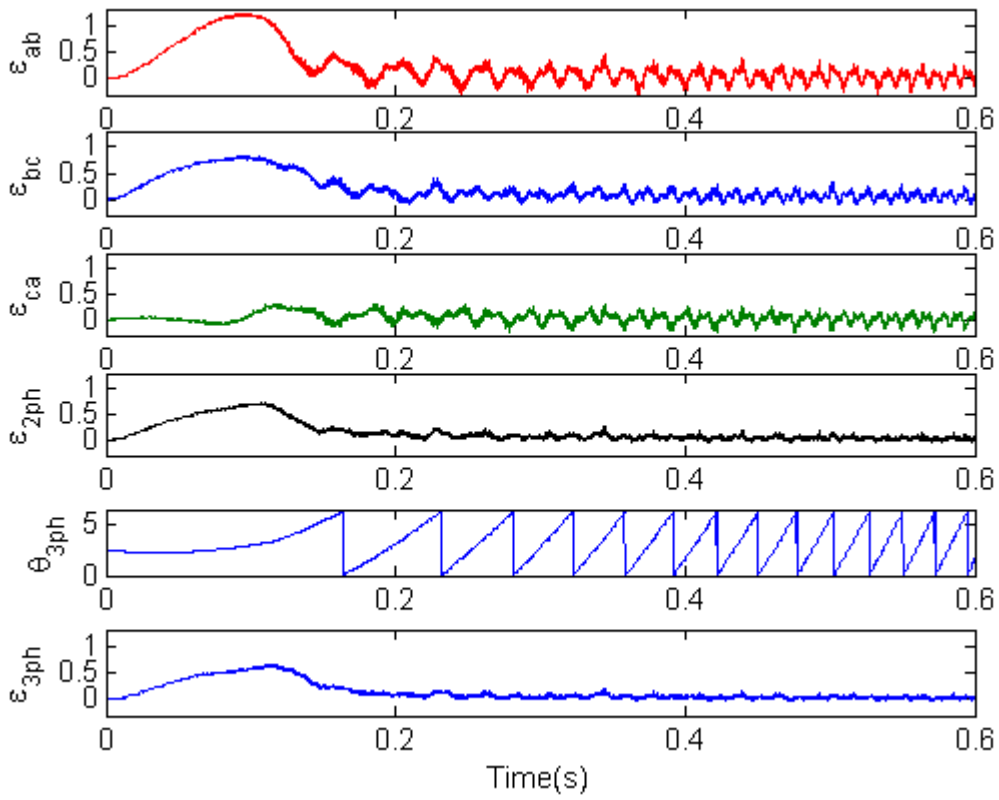

(c)

Figure 6.11 Starting performance of the motor drive 1. From the top: (a) phase currents and voltages (b) actual and estimated 2ph rotor positions (c) 3ph estimated rotor position and position errors

To explore the effect of an incorrect initial rotor position value while starting from standstill the measured voltage and the current waveforms in Figure 6.11 are utilized to estimate the rotor position using the two-phase and the three-phase position estimation methods. It was assumed in this test that the starting position data was in error by 2 rad. It is seen in Figure 6.12, that the rotor position estimates in both methods converge quickly to the actual rotor position within the first electrical cycle due to the automatic correction capabilities of the estimation algorithms. Similar results were seen with simulated voltage-current data in Figure 5.10.

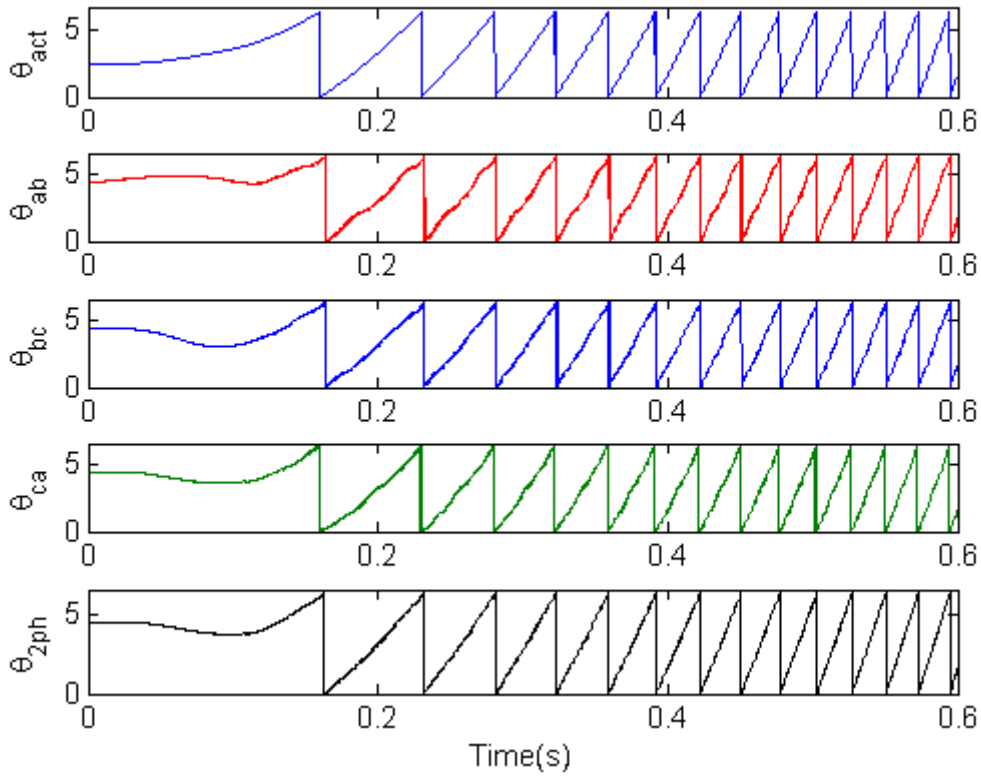
θact
θab
θbc
θca
θ2ph
5
0
0.2
0.4
0.6
Time(s)

(a)

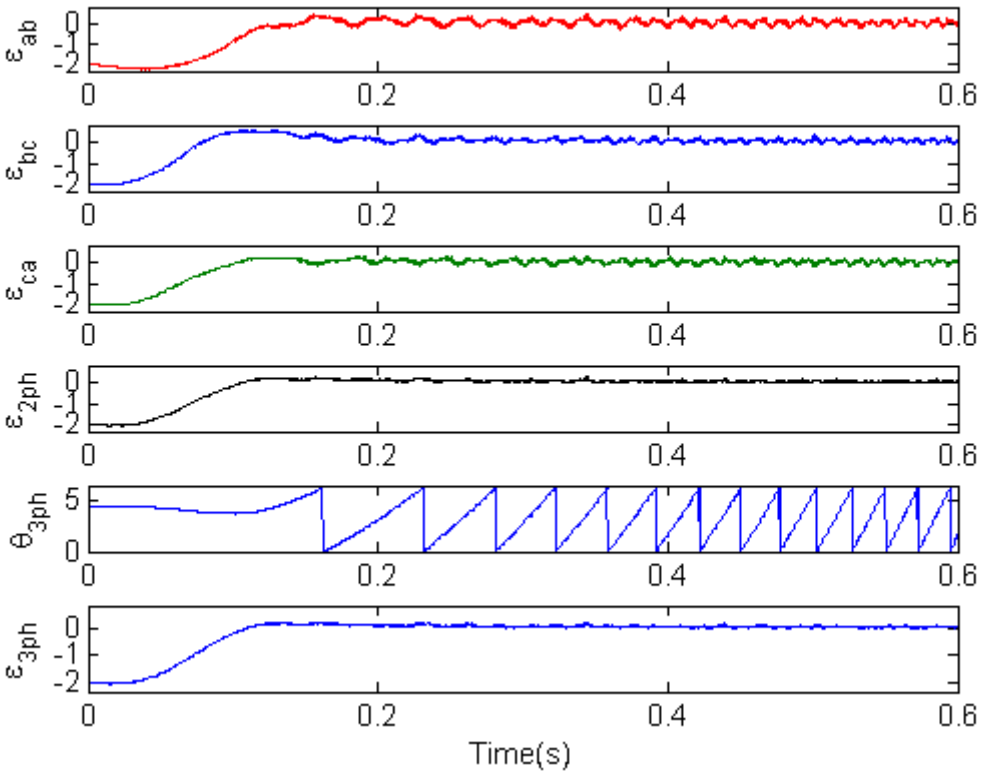
εab
εbc
εca
ε2ph
θ3ph
ε3ph
0
-1
-2
5
0.2
0.4
0.6
Time(s)

(b)

Figure 6.12 Starting performance of the motor drive 1 with an initial position error of 2 rad. From the top: (a) actual and estimated 2ph rotor positions (b) 3ph estimated rotor position and position errors

In Figures 6.13 and 6.14, two sets of test results are presented to investigate the dynamic performance of the sensorless position estimation methods under a step load change in the motor drive. In the first set of results a deceleration of the motor is demonstrated (which is similar to the simulation results given in Figure 5.11). In this operating mode while the motor was operating at a steady-state speed of 2,100 rpm, a step load was applied at about 0.15s by connecting a resistive load to the DC generator. As can be seen in the figure, the phase current waveforms were distorted until the instant of the step load due to the high back EMF voltage. However, as the motor speed is reduced due to addition of load, the distortion in the phase currents are reduced significantly. However, it was observed that the estimation error increases slightly after the step load as shown in Figure 6.13, which also confirms the simulation results in Figure 5.11. Note that although these results indicate a poor dynamic performance in terms of torque control the estimated position is still at the acceptable levels which can be used in the real time system.

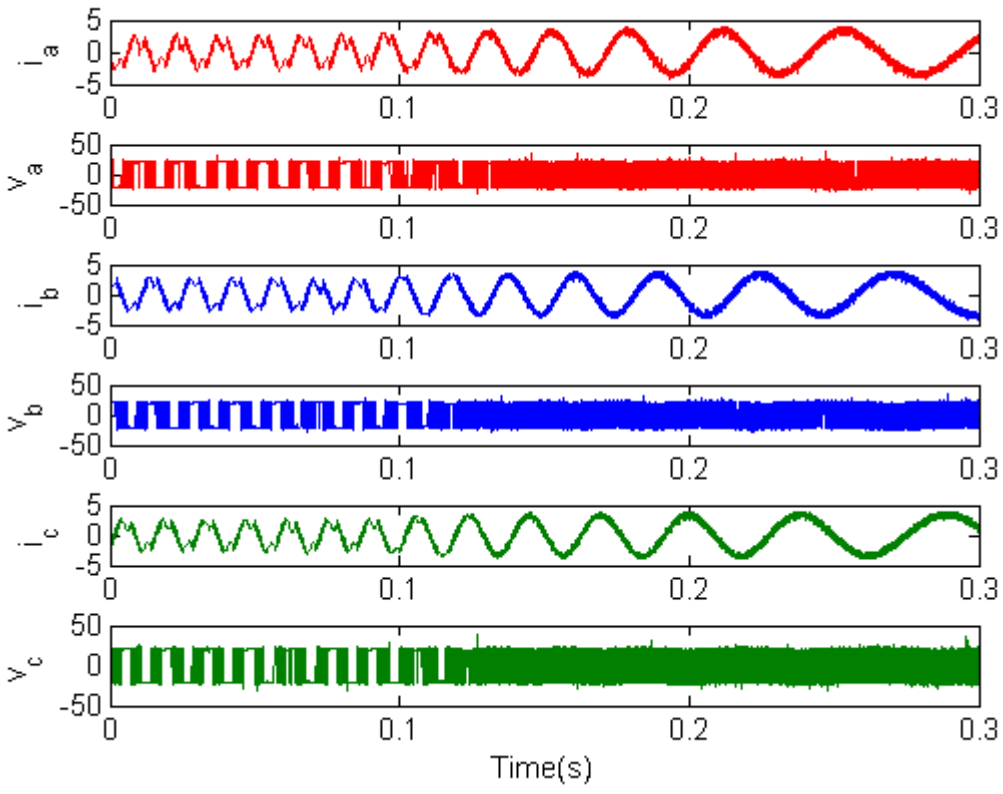

(a)

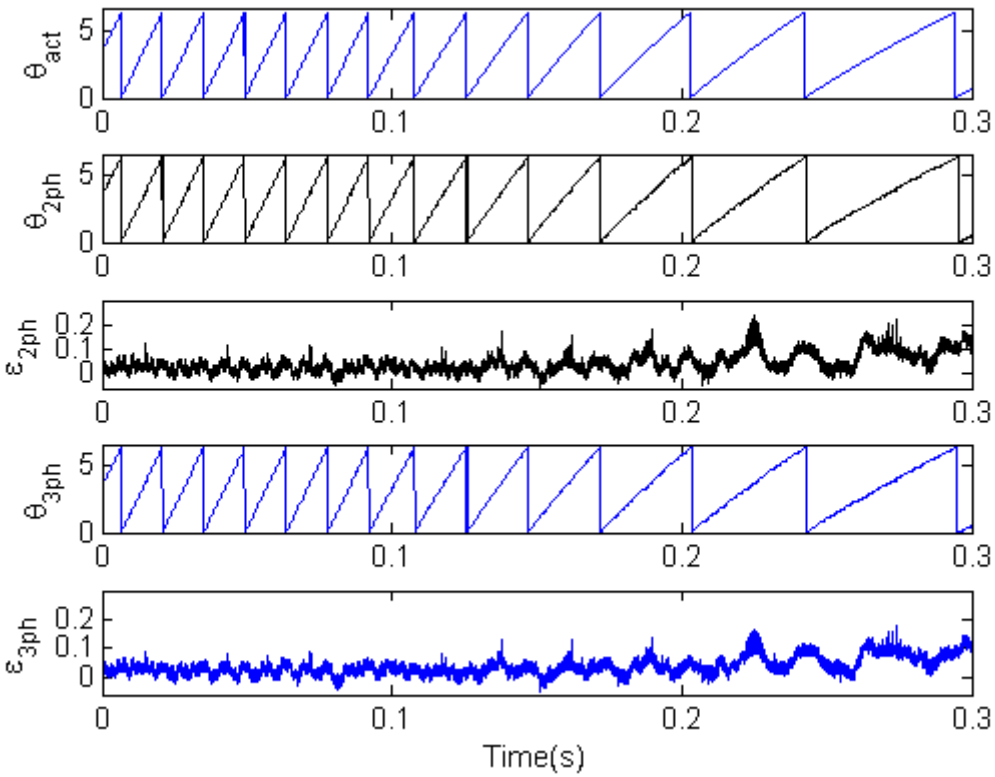

(b)

Figure 6.13 Dynamic performance of the motor drive 1 with a step load change (deceleration test). From the top: (a) phase currents and voltages (b) actual and estimated position and errors.

Figure 6.14 shows another set of test results to examine the acceleration performance of the motor drive as illustrate in Figure 5.11 simulation results. In this test, while the motor was operating at a speed of 300 rpm, the generator load was removed at about 0.25s, which resulted the motor speed to increase to about 1500 rpm. As it can be observed, the position estimation error decreased slightly after the load was removed, which is a desirable outcome. It should be noted here that the offline results given in Figure 6.13 and 6.14 were selected to be consistent with the simulation studies and they confirm the effectiveness of the position estimation methods under such extreme operating condition as it can be present in a real motor drive.

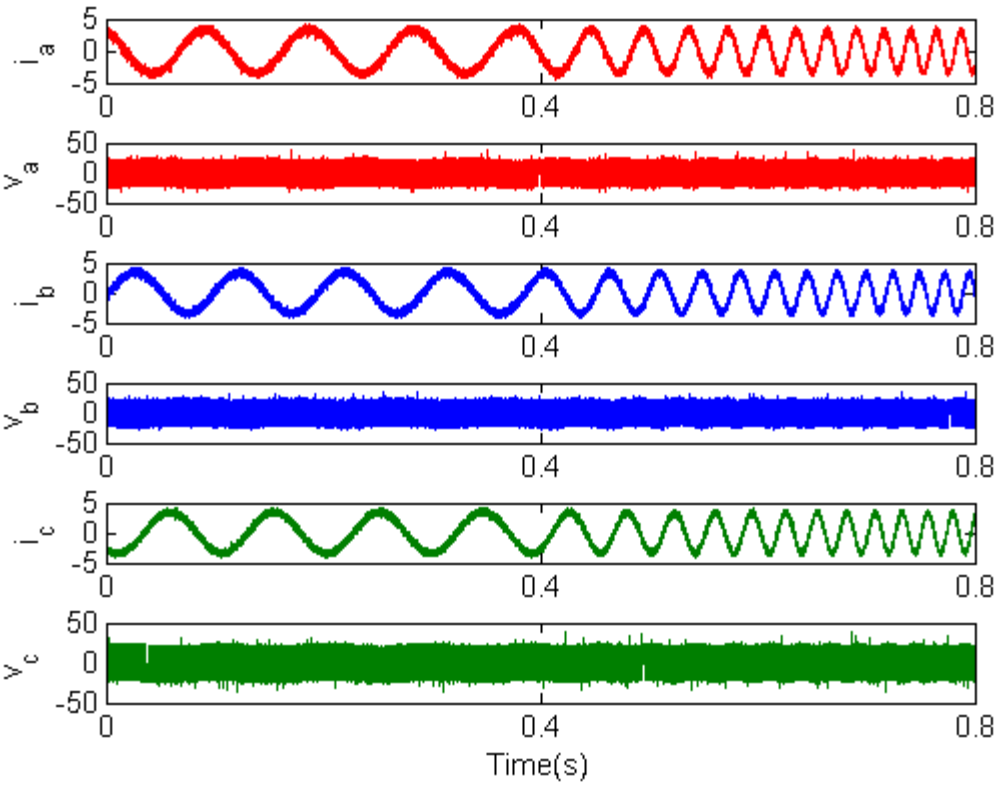
i_a
v_a
i_b
v_b
i_c
v_c
5
0
-5
50
-50
0.4
0.8
Time(s)

(a)

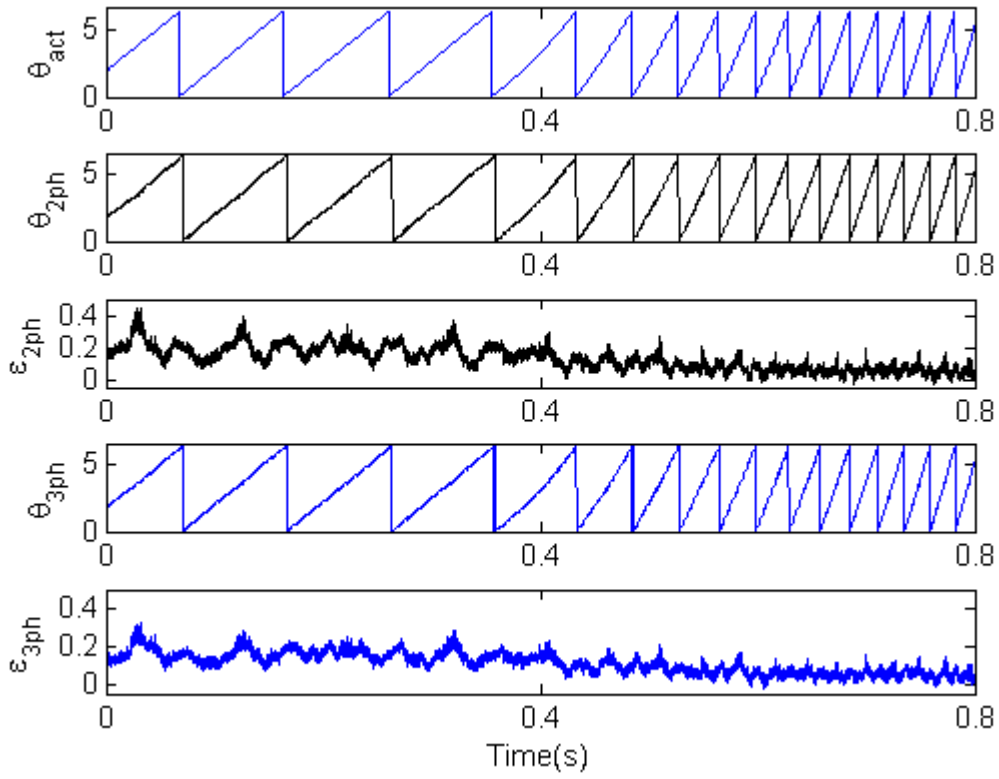
θact
θ2ph
ε2ph
θ3ph
ε3ph
5
0
0.4
0.2
0.8
Time(s)

(b)

Figure 6.14 Dynamic performance of the motor drive 1 with a step load change (acceleration test). From the top: (a) phase currents and voltages (b) actual and estimated position and errors.

6.4.3 Operation under Faults

To investigate the capabilities of the proposed position estimation methods under faults as carried out in the simulation study in Figure 5.12, a number of tests were performed using the off-line real data. Figure 6.15 illustrates the performance of the two position estimation techniques under a one-phase winding open-circuit fault of the motor module 1. While the motor was rotating at a steady-state speed of 2,100 rpm, Phase C of the motor module 1 was open-circuited at 0.51s where it was assumed that the fault occurred after the voltage sensor measurement point. As can be seen in the results, the phase current in Phase C becomes zero and the terminal voltage of the corresponding phase becomes the back EMF voltage induced in the phase after the failure. As the voltage measurement for the open-circuited phase was still available, the position estimation techniques were not affected by this fault and the estimated position is similar to the actual rotor position as illustrated in the figure.

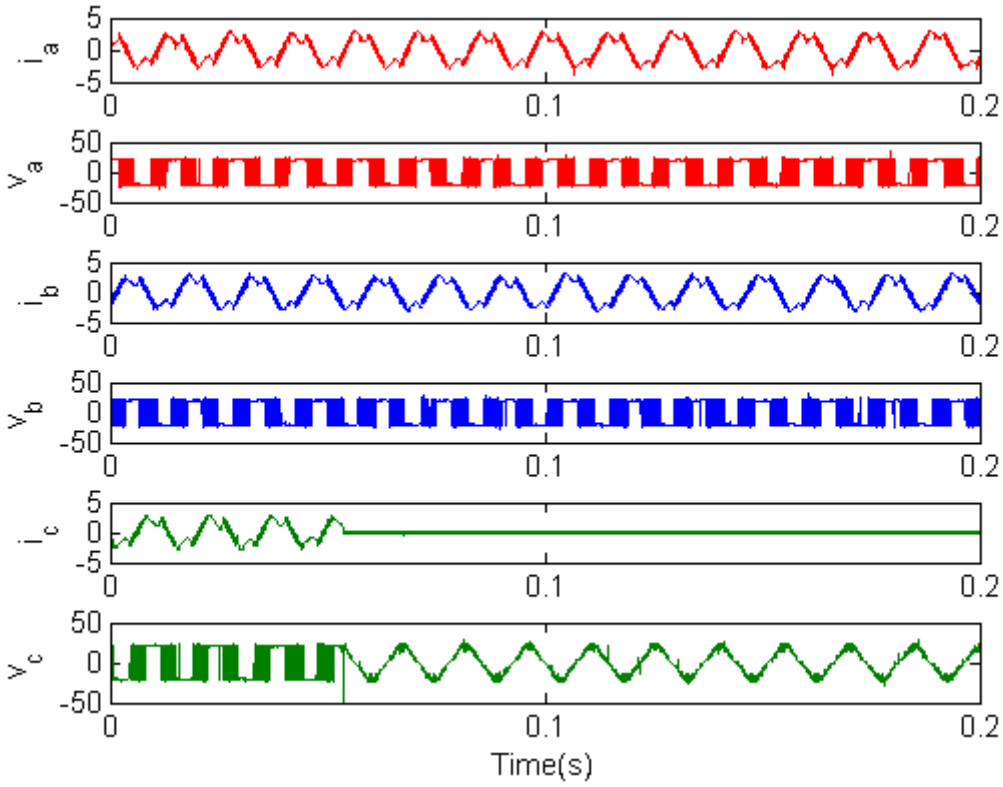

(a)

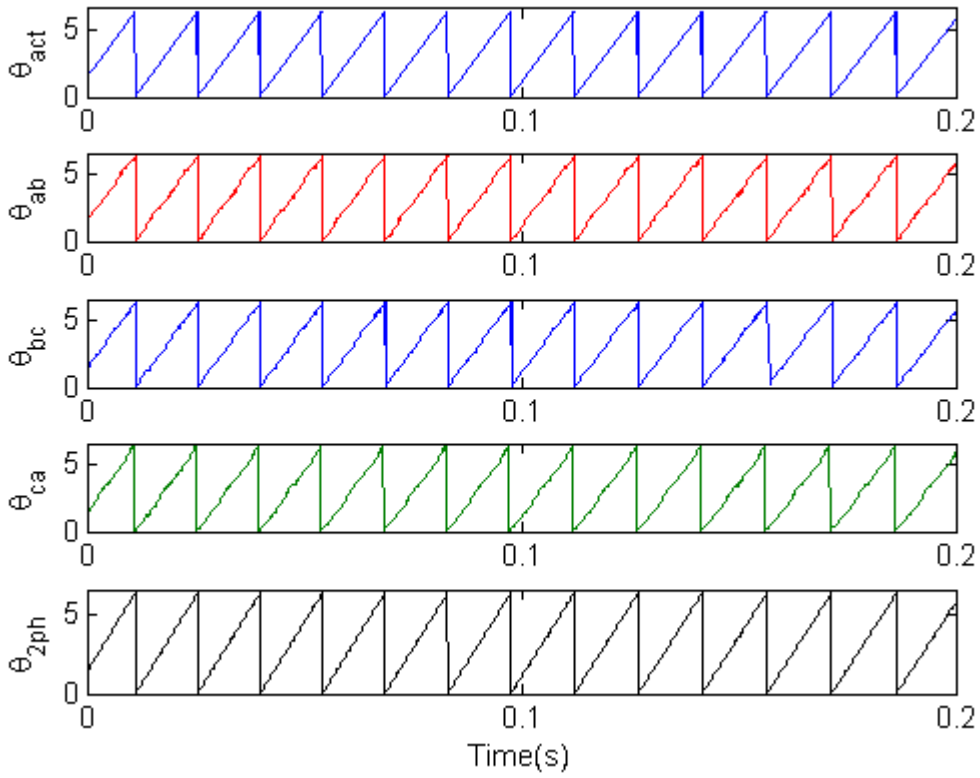
θact
θab
θbc
θca
θ2ph
5
0
0.1
0.2
Time(s)

(b)

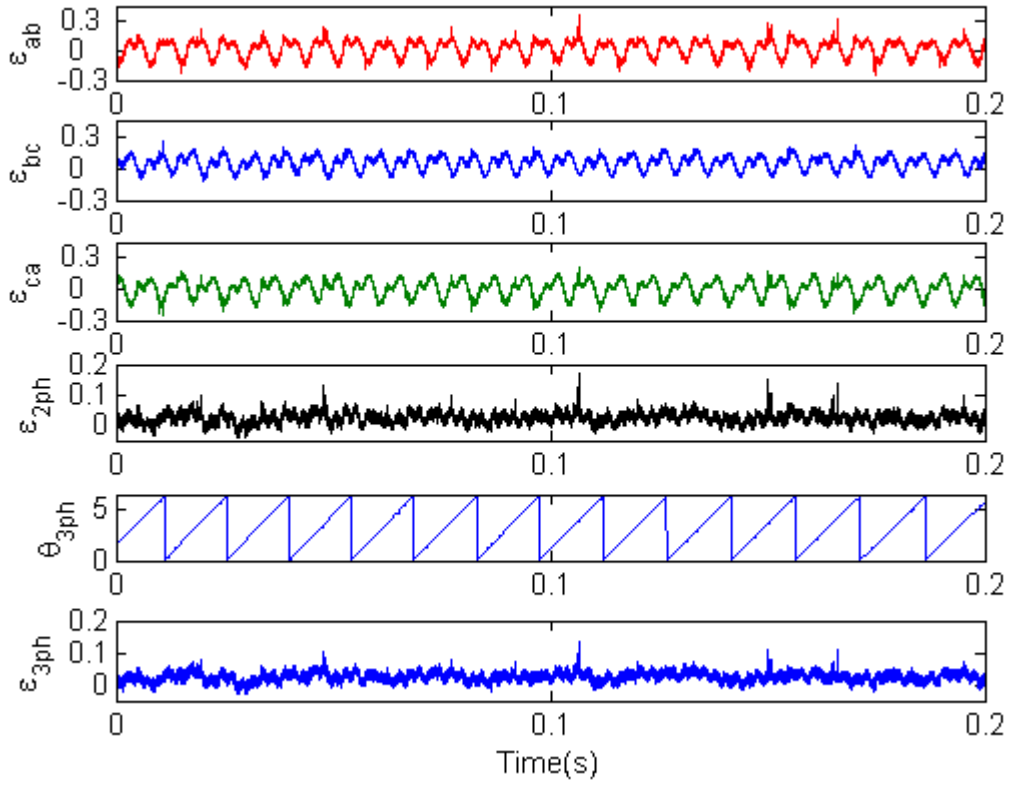
εab
εbc
εca
ε2ph
θ3ph
ε3ph
0.3
0
-0.3
0.2
0.1
5
0.1
0.2
Time(s)

(c)

Figure 6.15 Performance of the position estimators under an open-winding fault in the phase A. From the top: (a) phase currents and voltages (b) actual and estimated 2ph rotor positions (c) 3ph estimated rotor position and position errors

A single sensor fault in a current sensor or a voltage sensor was also introduced during the offline study like the previous simulation test seen in Figure 5.13. Two tests were carried out as shown in Figure 6.16. In order to simulate a current sensor fault, the gain of the single current sensor (Phase A of the motor module 1) was increased by a factor of 10 times (compared to the original gain). Similarly, the gain of the voltage sensor of the same phase was increased 10 times to simulate the voltage sensor fault.

Figures 6.16 (a) and (b) show the results obtained from the above mentioned tests. The results indicate that the two-phase position estimation method failed to obtain accurate rotor position estimates using a pair of phases which included the faulty phase A (such as Phases A-B and Phases C-A). However, an accurate rotor position estimate was possible using the healthy pair of phases (Phases B-C) of the motor module 1 where RMS value of the estimation errors were 0.077 rads in both tests. On the other hand, the three-phase position estimation method cannot operate effectively under such fault since it utilizes measurements obtained from all three winding phases including the faulty-phase Phase A.

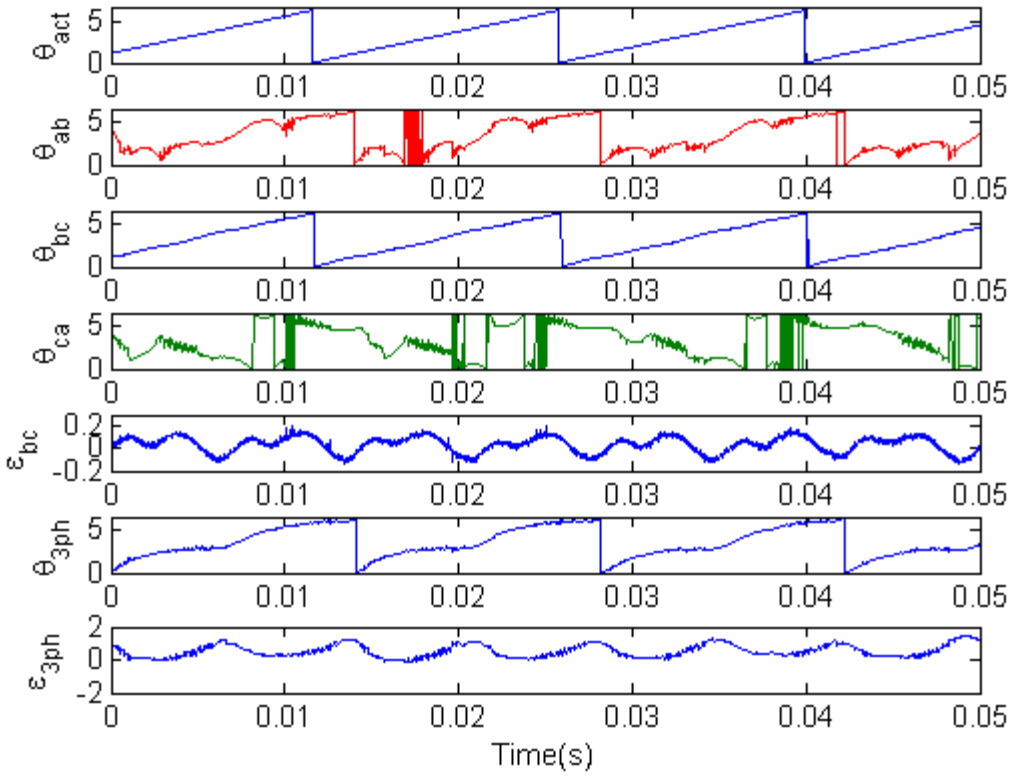

(a) a current sensor fault in Phase A

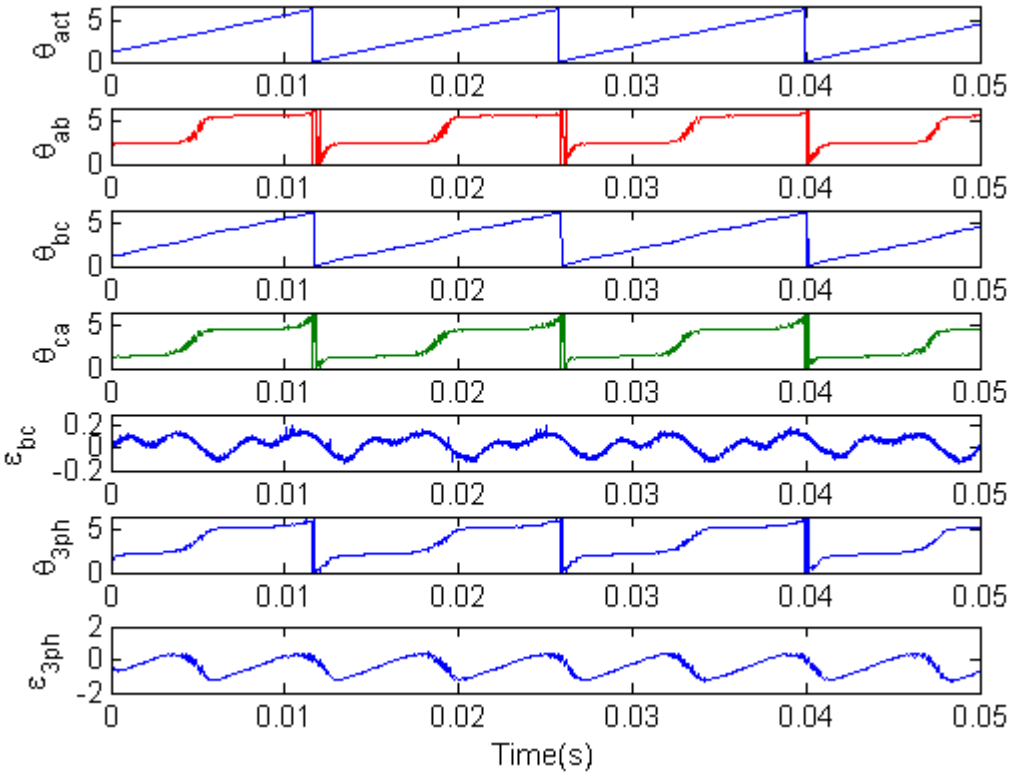

(b) a voltage sensor fault in Phase A

Figure 6.16 Operation performance of the motor drive 1 under (a) a current sensor fault in Phase A and (b) a voltage sensor fault in Phase A.

Table 6.5 RMS position estimation error in computer simulation and offline tests under a current or voltage sensor fault in Phase A

		RMS Position Estimation Error (rad)	
		Two-Phase Method	Three-Phase Method
Current Sensor Fault in Phase A	Phase a-b: sim/offline	0.836/0.785	
	Phase b-c: sim/offline	0.0126/0.0772	
	Phase c-a: sim/offline	large /large	
	Total: sim/offline	large /large	0.7432/0.698
Voltage Sensor Fault in Phase A	Phase a-b: sim/offline	1/0.953	
	Phase b-c: sim/offline	0.0126/0.0772	
	Phase c-a: sim/offline	0.7722/0.644	
	Total: sim/offline	0.482/0.464	0.666/0.651

6.5 Conclusions

In order to prove the effectiveness of the proposed two-phase and the three-phase sensorless position estimation methods, an extensive number of tests were performed using the real motor drive. The hardware of the fault-tolerant PMAC motor drive consisted of two fault-tolerant PMAC motor drives on a common shaft including six H-bridge inverters, the current measurement circuits and two DSP-based motor controllers. An incremental encoder was attached to the rotor to obtain the actual rotor position for the control system and to estimate the position error. The hardware also included a DC generator on the shaft whose load was changed via a resistor/switch arrangement (to simulate the step load change).

During the tests, the motor drive was operated in torque control mode and the phase currents, the phase voltages and the encoder signals were sampled simultaneously by the LabVIEW-based data acquisition system, where the measured data was saved for off-line processing. The measured phase currents and the phase voltages were utilized to estimate the rotor position using the proposed position estimation methods, which were

also implemented in LabVIEW. Finally, the rotor position estimates were compared with the actual rotor position obtained from the encoder.

As studied, in the two-phase position estimation method, three rotor position estimates were obtained by using the phase currents and the phase voltages. Each position estimation consisted of a pair of neighbouring phases, such as A-B, B-C and C-A. Under normal operating conditions (no fault) in the motor drive, the three position estimates were averaged to obtain a single more accurate rotor position estimate. However, the three-phase position estimation technique provided only one rotor position estimate per module since it utilizes the measured phase currents and the phase voltages from all three phases.

In order to investigate the steady-state performance of the methods, the motor was operated at a constant speed of 300rpm (considered as low-speed) and a constant high speed of 2100rpm. From the off-line test results, it was observed that the RMS position estimation errors obtained at low speeds was around 0.11 to 0.15 rads which reduced to about 0.02 rads at higher speeds. However, the position errors were found acceptable in both cases. In addition, it was observed that both position estimation methods have similar accuracy under the steady-state speeds.

As the proposed position estimation techniques rely on the motor parameters (i.e. the phase resistances, the phase inductances and the back EMF constants) and the measured phase currents and phase voltages, the parameter variations and measurement inaccuracies were also considered in this chapter to examine the robustness of the methods. It was concluded that the methods are robust enough against such changes, but more sensitive to errors in the back EMF constant than the other motor parameters. The position estimation errors due to the variations of the parameters were found satisfactory.

The measurement inaccuracies were simulated by changing the gains and the offsets of both the current and voltage sensors. It was concluded that the gains of the voltage sensor measurements caused the largest errors in the rotor position estimates in both position estimation methods. The RMS position errors were 0.063 rads for the two-phase position estimator and 0.085 rads for the three-phase position estimator respectively which are still acceptable.

In order to study the dynamic performance of the position estimation methods, the motor was also started from standstill, and tested under step-load changes. In these tests, the proposed methods demonstrated good dynamic performance and also good accuracies in the position estimates using the off-line real data. It was also observed that the estimation errors were large at start but reduced quickly (within one electrical cycle) to an acceptable value due to the PLL method adopted.

The effect of a large incorrect initial rotor position in the estimation was also studied using the off-line data captured during dynamic and steady-state operation. The operating conditions in this part included starting from standstill and operation at steady-state high speed. The test results demonstrated that the estimation techniques can track the real position even if the initial value of the rotor position is incorrect. As shown, this initial phase difference (2 rad) was compensated within the first electrical cycle. These results demonstrate that the proposed rotor position estimation methods have the capability to estimate the rotor position value even when the motor starts from an unknown value of the rotor position.

Several tests using the measured off-line data were also done in this chapter to examine the performance of the position estimation methods under a single winding open-circuit fault, a current sensor and a voltage sensor fault. In the single winding open-circuit fault, both proposed estimation techniques generate accurate rotor position estimates due to the presence of the back EMF voltage in the faulty phase after the fault.

In a single current sensor or a voltage sensor fault however the three-phase sensorless position estimation method and the two-phase sensorless position estimation method failed to obtain an effective rotor position estimate due to using information from the faulty phase. However, it was shown that the two-phase sensorless position estimation method was able to calculate the rotor position accurately using the healthy phases only.

It can be concluded from the results that both position sensorless methods show good performance over a wide range of operating conditions. However the three-phase method can not obtain an acceptable level of rotor position estimate when a fault occurs. It was shown that the two-phase method can estimate the rotor position value accurately using a pair of phase measurements consisting two healthy phases in a three-phase motor drive module. Therefore, it can be concluded that the two-phase sensorless

position estimation method has better reliability than the three-phase sensorless position estimation method.

It should be noted here that the three-phase position estimation method has in general better performance than the two-phase position estimation method. As it was demonstrated, under the back-EMF constant variation and voltage sensor gain error, however, the three-phase method presents larger estimation errors than the two-phase method. This is due to the fact that back emf constants have greater effect on the position increment estimation than the parameter variations or measurement inaccuracies (see equations (5.3) and (5.8)).

7. General Conclusions and Suggestions for the Future Study

7.1 Summary of Thesis

In this thesis, position estimation methods were developed to obtain the rotor position information for fault-tolerant PMAC motor drives with redundancy for safety critical applications under normal and faulty operating conditions. The fault-tolerant motor drive system had dual motor drive modules on a common shaft to give parallel redundancy. Each module contained electrically, magnetically, thermally and physically independent phases to provide inherent fault-tolerant capabilities. The following statements provide a general summary of the thesis.

In order to give a theoretical basis for the study, Chapter 2 introduced the operating principles and control techniques for the fault-tolerant PMAC motor drive with redundancy utilized in the thesis. This contained two fault-tolerant PMAC motor drives on a common rotor shaft giving parallel redundancy. Each PMAC motor drive adopted a special design methodology to provide electrical, magnetic, thermal and physical independence between winding phases so that it had inherently fault-tolerant capabilities. In addition, each motor drive used three H-bridge inverters. Furthermore, Chapter 2 described the torque control, closed-loop current control scheme and current excitation for the motor drive.

Chapter 3 provided a comprehensive survey of sensorless position estimation methods to obtain the rotor position without using a position sensor and starting techniques in PMAC motors. The position estimation techniques can be broadly classified into three groups. Firstly, the rotor position information is determined from the back-EMF. This includes schemes based on the back EMF induced in the unexcited stator winding, the third harmonic component of the back EMF of the open-circuit phase winding or detecting the conduction states of freewheeling diodes of the inverter in the unexcited phase in a trapezoidal PMAC motor. However, these approaches have limited performance at low speeds since the magnitude of back EMF is small. Therefore, they require special starting schemes.

Secondly, a number of position estimation methods have utilized both knowledge of the motor parameters and measurements of the terminal voltages and winding currents

to obtain the rotor position. They were generally based on state observers, Kalman filtering methods, to estimate the flux linkages. These methods however depend on the accuracy of the measured currents or voltages and also are sensitive to motor parameter variations due to temperature or saturation. In addition, the techniques are computationally intensive and hence require expensive and powerful processors. In these techniques, the drift due to the use of integration functions degrades performance at low speeds.

Finally, a range of position detection methods were based on detecting the magnetic saliencies due to the geometric construction as in the case of salient pole PMAC motors or saturation effects as in the case of surface-mounted PM motors to determine the rotor position information. While a few methods have tracked the inductance variation with respect to the rotor position without using any special signal injection, a number of methods have made use of injected signals such as pulse or sinusoidal signals for using the magnetic saliencies of salient or non-salient PMAC motors. The most important advantage of the approaches based on the magnetic saliencies is that they are able to estimate the rotor position at low speeds including zero speed. Also, the methods are less sensitive or completely insensitive to parameter variations of the motor. However, the rotor position detection may depend on the rotor geometry as the techniques are based on the magnetic saliencies. Due to iron saturation, the methods may be limited to part loads. Also, the techniques demonstrate a limited performance in high speed regions due to the effect of back EMF.

As seen in the literature review in Chapter 3, a lot of methods have been proposed to estimate the rotor position for PMAC motors. However, the developed sensorless methods chiefly have been applied to conventional PMAC motors. Thus, they may not be directly applicable to the fault-tolerant PMAC motor drive with redundancy utilized in the thesis. Also, most of them have not considered faulty conditions in the motor drives and are not able to provide redundant rotor position information which is vital to improve the reliability and the fault tolerant capability of the motor drive.

In order to explore the performance of the fault-tolerant PMAC motor drive with redundancy, modelling and simulation were conducted in Chapter 4. The mathematical modelling involved dual fault-tolerant three-phase surface-mounted PMAC motors with sinusoidal back EMF voltages and H-bridge inverters where each phase was excited with sinusoidal currents utilizing a hysteresis current controller producing switching

signals for a corresponding H-bridge inverter. The motors were modelled by voltage, torque and motion equations in the abc reference frame where the voltage equations were utilized to develop the sensorless position estimation methods later in the thesis.

Based on the developed modelling, simulation models using a graphical programming language, Simulink™ were employed to study the steady and dynamic performance of the motor drive system. This included low and high speed operation and starting from standstill.

In Chapter 5, two position estimation schemes were proposed to obtain rotor position information without using a position sensor for the fault-tolerant PMAC motor drive with redundancy. These techniques had the capability to achieve multiple available rotor position estimates under normal and faulty conditions in the motor windings, the inverters or sensors and hence increasing both the reliability and the fault tolerance of the drive system. They are referred to as the three-phase and the two-phase sensorless position estimation methods.

Both algorithms utilize measurements of the voltages and currents in the stator winding phases. Using the measured data, the flux-linkage increments of the phase windings are computed directly without an integration process. Next, the rotor position increments can be calculated using the flux-linkage increments as well as knowledge of the back EMF functions. These are assumed to be sinusoidal functions with unity magnitude. It should be noted that the back EMF voltages are divided into two sub-parts, the back EMF functions and their amplitudes which are proportional to the mechanical rotor speed. After that, the rotor position can be predicted by integrating the rotor position increments. This predicted position value should be precise in an ideal motor drive system. However, due to motor parameter variations and measurement errors in a practical motor drive, errors will be produced in the rotor position increment estimates and accumulated in the integration procedure used to obtain the predicted rotor position. In order to compensate for these errors, a phase-locked loop (PLL) scheme is employed to allow the predicted rotor position to be locked on to the flux linkage increments. This produces a more accurate rotor position estimate.

The three-phase sensorless position estimation algorithm utilizes the measured data from all three phase windings in each motor drive module. As a result, it can obtain two position estimates (one from each module) for the fault-tolerant PMAC motor drive

with redundancy. However, the two-phase sensorless position estimation technique is based on the measurement of values from two phases in each motor drive module. Consequently, it is able to produce three rotor position estimates for each module and hence six rotor position estimates are available for the dual motor drive modules. Under normal operating conditions, all available position estimates can be averaged to achieve a final accurate rotor angle estimate in both algorithms. However, under faulty conditions, a final rotor position estimate can be obtained by averaging position estimates obtained by using the measured values from healthy phases since position estimates obtained with the measurements from a phase (or phases) involving a failure will not produce acceptable position estimates.

In order to verify the effectiveness of the proposed position estimation schemes for the fault-tolerant PMAC motor drive with redundancy, computer simulation and off-line studies were carried out under healthy and faulty conditions in the motor drive in Chapters 5 and 6. In Chapter 5, simulation models were developed for the proposed algorithms and these were tested using simulated voltage and current data from the motor drive model developed in Chapter 4. In Chapter 6, the algorithms were tested using offline measured voltage and current data. This data was obtained from a prototype system operated in a torque control mode using a data acquisition system.

7.2 Key Results

The simulation and off-line test results validated the effectiveness of the proposed position estimation methods under steady-state, dynamic and faulty operating conditions. Some features and comparisons of the developed position estimation techniques can be summarized as follows.

- Both sensorless position estimation schemes had the ability to give multiple rotor position estimates to improve the reliability and the fault tolerant capability of the motor drive system. Even under faulted conditions in the motor windings, inverters or sensors, they could obtain accurate rotor position estimates utilizing the measurements of phase currents and terminal voltages from healthy phases in the motor drive system. However, the two-phase sensorless position estimation method is more reliable than the three-phase sensorless position estimation method as it can give more redundant position estimates in the presence of faults.

- They were able to obtain accurate rotor position information under steady state operation involving low and high state speeds. However, the position estimation errors in the low speed test were larger than those of the high speed test in both methods.
- They presented good dynamic performance and similar accuracies under starting from standstill and step load changes. Though the rotor position estimates had large errors initially in the starting test, they were quickly compensated by the PLL technique utilized in the developed algorithms within an electrical cycle.
- Both proposed sensorless methods were robust against parameter variations as well as inaccurate measurements. However, both methods in particular were more affected by variations of the back EMF constants than the other parameter variations. Also, gain errors were more serious than offsets errors in both the current and voltage sensors.
- They had the capability to rapidly obtain accurate rotor position estimate even when starting with an initially incorrect rotor position angle with a large phase difference from the actual rotor position.

7.3 Suggestions for Future Research

This thesis has verified the feasibility of the proposed position estimation methods for the fault-tolerant PMAC motor drive with redundancy under normal and faulty operating conditions. It has carried out modelling, computer simulation and analysis using off-line real data. Some suggestions can be made for future work as follows:

- Although the results presented in this research using the offline real data demonstrates a robust and an accurate position estimation method for the fault-tolerant motor drive, the final performance tests should include a closed-loop real system. Due to the availability of the resources and time limitations this was not covered in this study. In such a real-time closed-loop control system, the sampling rate to measure the phase voltages and the phase currents should be sufficiently large (at least six times greater than the switching frequency of the inverter). In addition, the current and the voltage sensors with high bandwidths should be utilized to meet these sampling requirements.

Furthermore, faster and more powerful DSP controllers (such as TMS320F281x, TMS320F2833x or TMS320F2833x of Texas Instruments) are required to achieve the computationally intensive estimations.

- As stated earlier in Section 5.5.3, this research requires the integration of the research in [14] to be able to obtain a complete fault-tolerant motor drive.
- Finally, a reconstruction technique for the phase voltages (such as in [25]) in the stator windings can be integrated into the proposed position estimation methods to reduce the number of sensors required.

Publications

[I] J. S. An, N. Ertugrul, W. L. Soong, J. W. Zhu and A. Gargoom, "An Indirect Rotor Position Estimation Technique for a Fault-Tolerant Brushless PM Motor Drive," In CD of IEEE 39th Power Electronics Specialists Conference, (ID 8722), Rhodes, Greece, Jun. 2008.

[II] J. S. An, N. Ertugrul and W. Soong, “Sensorless Position Estimation in a Fault Tolerant Motor Drive with Redundancy,” Australian Journal of Electrical & Electronics Engineering, Vol. 3, No. 2, pp. 157-165, 2007.

[III] J. S. AN, N. Ertugrul and W. L. Soong, “Sensorless Position Estimation in a Fault Tolerant Surface-Mounted Permanent Magnet AC Motor Drive with Redundancy,” 32nd Annual IEEE Industrial Electronics Conference (IECON 2006), 6-10 Nov. 2006, Paris, France, pp. 1429-1434.

[IV] J. S. An, N. Ertugrul and W. L. Soong, “Sensorless Position Estimation in a Fault Tolerant Motor Drive with Redundancy,” Proceedings of the Australasian Universities Power Engineering Conference (AUPEC 2005), 25-28 Sep. 2005, Hobart, Tasmania, Australia, pp. 497-502.

References

[1] J. S. Cloyd, "Status of the United States Air Force's More Electric Aircraft Initiative," IEEE Aerospace and Electronic Systems Magazine, Vol. 13(4), pp. 17-22, Apr. 1998.

[2] "Today… Tomorrow…," IEEE Aerospace and Electronic Systems Magazine, Vol. 15(10), pp. 137-144, Oct. 2000.

[3] J. C. Knight, "Safety Critical Systems: Challenges and Directions," Proceedings of the 24th International Conference on Software Engineering (ICSE2002), 2002, pp. 547-550.

[4] M. D. Kankam and M. E. Elbuluk, "A Survey of Power Electronics Applications in Aerospace Technologies," Prepared for the 36th Intersociety Energy Conversion Engineering Conference (IECEC2001-AT-32), National Aeronautics and Space Administration, Jul. 29-Aug. 2 2001, pp. 1-8.

[5] R. J. Patton, F. J. Uppal and C. J. Lopez-Toribio, "Soft Computing Approaches to Fault Diagnosis for Dynamic Systems: A Survey," IFAC Symposium SAFEPROCESS 2000, Budapest, Jun. 14-16, 2000, pp. 298-311.

[6] C. M. Stephens, "Fault Detection and Management System for Fault-Tolerant Switched Reluctance Motor Drives," IEEE Transactions on Industry Applications, Vol. 27(6), pp. 1098-1102, Nov./Dec. 1991.

[7] T. M. Jahns, "Fault-Tolerant Switched Reluctance Machine," United States Patent, Patent Number: 4,896,088, Date of Patent: Jan. 23, 1990.

[8] X. Chen, Z. Deng and J. Peng, "Fault Tolerant Switched Reluctance Machine for Fuel Pump Drive in Aircraft," 4th IEEE Conference on Industrial Electronics and Applications (ICIEA 2009), 25-27 May 2009, pp. 2340-2344.

[9] R. Rabinovici, "Torque Ripple, Vibrations, and Acoustic Noise in Switched Reluctance Motors," HAIT Journal of Science and Engineering B, Vol. 2, Issues 5-6, pp. 776-786, 2005.

[10] A. G. Jack, B. C. Mecrow and J. A. Haylock, "A Comparative Study of Permanent Magnet and Switched Reluctance Motors for High-Performance Fault-Tolerant

Applications," IEEE Transactions on Industry Applications, Vol. 32, No. 4, pp. 889-895, Jul./Aug. 1996.

[11] T. Gopalarathnam, H. A. Toliyat and J. C. Moreira, "Multi-Phase Fault-Tolerant Brushless DC Motor Drives," Conference Record of the 2000 IEEE Industry Applications Conference, Vol. 3, 8-12 Oct. 2000, pp. 1683-1688.

[12] N. Ertugrul, W. Soong, G. Dostal and D. Saxon, "Fault Tolerant Motor Drive System with Redundancy for Critical Applications," IEEE 33rd Power Electronics Specialists Conference, 23-27 June 2002, Vol. 3, pp. 1457-1462.

[13] N. Ertugrul, W. L. Soong, S. Valtenbergs and H. Chye, "Investigation of a Fault Tolerant and High Performance Motor Drive for Critical Applications," IEEE International Conference on Electrical and Electronic Technology, 19-22 August, 2001, Vol. 2, pp. 542-548.

[14] J. Zhu, "Modelling, Simulation and Implementation of a Fault Tolerant Permanent Magnet AC Motor Drive with Redundancy," PhD Thesis, School of Electrical and Electronic Engineering, The University of Adelaide, Australia, 2008.

[15] J. D. Ede, K. Atallah, J. Wang and D. Howe, "Effect of Optimal Torque Control on Rotor Loss of Fault-Tolerant Permanent-Magnet Brushless Machines," IEEE Transactions on Magnetics, Vol. 38, No. 5, pp. 3291-3293, Sep. 2002.

[16] K. Atallah, J. Wang and D. Howe, "Torque-Ripple Minimization in Modular Permanent-Magnet Brushless Machines," IEEE Transactions on Industry Applications, Vol. 39, No. 6, pp. 1689-1695, Nov./Dec. 2003.

[17] J. Wang, K. Atallah and D. Howe, "Optimal Torque Control of Fault-Tolerant Permanent Magnet Brushless Machines," IEEE Transactions on Magnetics, Vol. 39, No. 5, pp. 2962-2964, Sep. 2003.

[18] C. Bianchini, E. Fornasiero, T. N. Matzen, N. Bianchi and A. Bellini, "Fault Detection of a Five-Phase Permanent-Magnet Machine," 34th Annual Conference of the IEEE Industrial Electronics (IECON 2008), 10-13 Nov. 2008, pp. 1200-1205.

[19] B. C. Mecrow, A. G. Jack, J. A. Haylock and J. Coles, "Fault-Tolerant Permanent Magnet Machine Drives," IEE Proc.-Electr. Power Appl., Vol. 143, No. 6, pp. 437-442, Nov. 1996.

[20] J. A. Haylock, B. C. Mecrow, A. G. Jack and D. J. Atkinson, “Operation of Fault Tolerant Machines with Winding Failures,” IEEE Transactions on Energy Conversion, Vol. 14, No. 4, pp. 1490-1495, Dec. 1999.

[21] J. A. Haylock, B. C. Mecrow, A. G. Jack and D. J. Atkinson, “Operation of a Fault Tolerant PM Drive for an Aerospace Fuel Pump Application,” IEE Proc.-Electr. Power Appl., Vol. 145, No. 5, pp. 441-448, Sep. 1998.

[22] S. Green, D. J. Atkinson, A. G. Jack, B. C. Mecrow and A. King, “Sensorless Operation of a Fault Tolerant PM Drive,” IEE Proc.-Electr. Power Appl., Vol. 150, No. 2, pp. 117-125, Mar. 2003.

[23] B. C. Mecrow, A. G. Jack, D. J. Atkinson, S. R. Green, G. J. Atkinson, A. King and G. Green, “Design and Testing of a Four-Phase Fault-Tolerant Permanent-Magnet Machine for an Engine Fuel Pump,” IEEE Transactions on Energy Conversion, Vol. 19, No. 4, pp. 671-678, Dec. 2004.

[24] G. J. Atkinson, B. C. Mecrow, A. G. Jack, D. J. Atkinson, P. Sangha and M. Benarous, “The Analysis of Losses in High-Power Fault-Tolerant Machines for Aerospace Applications,” IEEE Transactions on Industry Applications, Vol. 42, No. 5, pp. 1162-1170, Sep./Oct. 2006.

[25] Y. Li, “A PMAC Motor Drive with a Minimum Number of Sensors,” PhD Thesis, School of Electrical and Electronic Engineering, The University of Adelaide, Australia, 2002.

[26] N. Ertugrul, “Position Estimation and Performance Prediction for Permanent-Magnet Motor Drives,” PhD Thesis, Department of Electrical and Electronic Engineering, The University of Newcastle Upon Tyne, UK, 1993.

[27] P. P. Acarnley and J. Watson, “Review of Position-Sensorless Operation of Brushless Permanent-Magnet Machines,” IEEE Transactions on Industrial Electronics, Vol. 53, No. 2, pp. 352-362, Apr. 2006.

[28] A. M. EL-Rafaie, T. M. Jahns and D. W. Novotny, “Analysis of Surface Permanent Magnet Machines with Fractional-Slot Concentrated Windings,” IEEE Transactions on Energy Conversion, Vol. 21, No. 1, pp. 34-43, March 2006.

[29] A. M. EL-Rafaie and T. M. Jahns, "Optimal Flux Weakening in Surface PM Machines using Fractional-Slot Concentrated Windings," IEEE Transactions on Industry Applications, Vol. 41, No. 3, pp. 790-800, May-June 2005.

[30] N. Mohan, T. M. Undeland and W. P. Robbins, "Power Electronics: Converters, Applications, and Design," John Willey & Sons Inc., Singapore, 1989.

[31] P. Pillay and R. Krishnan, "Modelling, Simulation, and Analysis of Permanent-Magnet Motor Drives, Part I: The Permanent-Magnet Synchronous Motor Drive," IEEE Transactions on Industry Applications, Vol. 25, No. 2, pp.265-273, March/April 1989.

[32] D. M. Brod and D. W. Novotny, "Current Control of VSI-PWM Inverters," IEEE Transactions on Industry Applications, IA-21, No. 3, pp. 562-570, May 1985.

[33] J. Holtz, "Pulsewidth Modulation-A Survey," IEEE Transactions on Industrial Electronics, Vol. 39, No. 5, pp. 410-420, Dec. 1992.

[34] L. Dalessandro, U. Drofenik, S. D. Round and J. W. Kolar, "A Novel Hysteresis Current Control for Three-Phase Three-Level PWM Rectifiers," 20th Annual IEEE Applied Power Electronics Conference and Exposition (APEC 2005), 6-10 Mar. 2005, Vol. 1, pp. 501-507.

[35] A. Nami, H. Ghoreishy and F. Zare, "A Novel Random Hysteresis Current Control for a Single-Phase Inverter," Australian Journal of Electrical & Electronics Engineering, Vol. 4, No. 3, pp. 285-295, 2008.

[36] K. Iizuka, H. Uzuhashi, M. Kano, T. Endo and K. Mohri, "Microcomputer Control for Sensorless Brushless Motor," IEEE Transactions on Industry Applications, Vol. IA-21, No. 4, pp. 595-601, May/June 1985.

[37] R. C. Becerra, T. M. Jahns and M. Ehsani, "Four Quadrant Sensorless Brushless ECM Drive," IEEE Applied Power Electronics Conference and Exposition, 1991, pp. 202-209.

[38] H. R. Andersen and J. K. Pedersen, "Sensorless ELBERFELD Control of Brushless DC-Motors for Energy-Optimized Variable-Speed Household Refrigerators," 7th European Conf. on Power Electronics and Applications, 8-10 Sep., 1997, Trondheim, Norway, Vol. 1, pp. 314-318.

[39] J. C. Moreira, “Indirect Sensing for Rotor Flux Position of Permanent Magnet AC Motors Operating in a Wide Speed Range,” Conference Record of IEEE IAS Annual Meeting, 1994, pp. 401-407.

[40] J. C. Moreira, “Indirect Sensing for Rotor Flux Position of Permanent Magnet AC Motors Operating Over a Wide Speed Range,” IEEE Transactions on Industry Applications, Vol. 32, No. 6, pp. 1394-1401, Nov./Dec. 1996.

[41] S. Ogasawara and H. Akagi, “An Approach to Position Sensorless Drive for Brushless DC Motors,” IEEE Transactions on Industry Applications, Vol. 27, No. 5, pp. 928-933, Sept./Oct. 1991.

[42] N. Ertugrul and P. P. Acarnley, “A new Algorithm for Sensorless Operation of Permanent Magnet Motors,” IEEE Transactions on Industry Applications, Vol. 30, pp. 126-133, 1994.

[43] C. French, P. Acarnley and I. Al-Bahadly, “Sensorless Position Control of Permanent Magnet Drives,” IEEE IAS-95, 1995, pp. 61-68.

[44] N. Ertugrul, P. P. Acarnley and C. D. French, “Real-Time Estimation of Rotor Position in PM Motors During Transient Operation,” 5th European Conference on Power Electronics and Applications, EPE’93, 13-16 Nov. 1993, Brighton, UK, Vol. 5, pp. 311-316.

[45] C. French and P. P. Acarnley, “Control of Permanent Magnet Motor Drives Using a New Position Estimation Technique,” IEEE Transactions On Industry Applications, Vol. 32, No. 5, pp. 1089-1097 Sep./Oct. 1996.

[46] R. Wu and G. R. Slemon, “A Permanent Magnet Motor Drive Without a Shaft Sensor,” Conference Record of IEEE IAS Annual Meeting, 1990, pp. 553-558.

[47] A. Consoli, S. Musumeci, A. Raciti and A. Testa, “Sensorless Vector and Speed Control of Brushless Motor Drives,” IEEE Transactions on Industrial Electronics, pp. 91-96, February 1994.

[48] R. Dhaouadi, N. Mohan and L. Norum, “Design and Implementation of an Extended Kalman Filter for the State Estimation of a Permanent Magnet Synchronous Motor,” IEEE Transactions on Power Electronics, Vol. 6, No. 3, pp. 491-497,1991.

[49] S. Bolognani, L. Tubiana and M. Zigliotto, “Extended Kalman Filter Tuning in Sensorless PMSM Drives,” IEEE Transactions on Industry Applications, Vol. 39, No. 6, pp. 1741-1747, Nov./Dec. 2003.

[50] S. Bolognani, R. Oboe and M. Zigliotto, “DSP-based Extended Kalman Filter Estimation of Speed and Rotor Position of a PM Synchronous Motor,” IECON’94, 20th International Conference on Industrial Electronics, Control and Instrumentation, 5-9 Sep. 1994, Vol. 3, pp. 2097-2102.

[51] V. Comnac, M. Cernat, F. Moldoveanu and I. Draghici, “Sensorless Speed and Direct Torque Control of Surface Permanent Magnet Synchronous Machines using an Extended Kalman Filter,” The 22nd Convention of Electrical and Electronics Engineers in Israel, 2002, pp. 39-44.

[52] R. C. Panaitescu and L. E. Norum, “Kalman-Filter Based Sensorless Control of an IPM Motor Drive,” 7th European Conference on Power Electronics and Applications, EPE’97, 8-10 Sep., 1997, Trondheim, Norway, Vol. 4, pp. 567-572.

[53] S. Bolognani, L. Tubiana and M. Zigliotto, “EKF-Based Sensorless IPM Synchronous Motor Drive for Flux-Weakening Applications,” IEEE Transactions on Industry Applications, Vol. 39, No. 3, pp. 768-775, May/Jun. 2003.

[54] L. A. Jones and J. H. Lang, “A State Observer for the Permanent Magnet Synchronous Motor,” IEEE Transactions on Industrial Electronics, Vol. 36, No. 3, pp. 374-382, Aug. 1989.

[55] M. Eskola and H. Tuusa, “Sensorless Control of a Permanent Magnet Synchronous Motor-Application to a Hoist Drive,” PESC’02 2002 IEEE 33rd Annual IEEE Power Electronics Specialists Conf., June 23-27, 2002, Cairns, Australia, Vol. 2, pp. 967-972.

[56] K. Tatemtsu, D. Hamada, K. Uchida, S. Wakao and T. Onuki, “Sensorless Control for Permanent Magnet Synchronous Motor with Reduced Order Observer,” Record of the 29th Annual IEEE Power Electronics Specialists Conference (PESC 98), 17-22 May 1998, Fukuoka, Vol. 1, pp. 125-131.

[57] J. S. Kim and S. K. Kim, “High Performance PMSM Drives Without Rotational Position Sensors Using Reduced Order Observer,” Conference Record of IEEE IAS Annual Meeting, 1995, pp. 75-82.

[58] Z. Chen, M. Tomita, S. Ichikawa, S. Doki and S. Okuma, “Sensorless Control of Interior Permanent Magnet Synchronous Motor by Estimation of an Extended Electromotive Force,” Conference Record of the 2000 IEEE Industry Applications Conference, Oct. 2000, Vol. 3, pp.1814-1819.

[59] S. Morimoto, K. Kawamoto, M. Sanada and Y. Takeda, “Sensorless Control Strategy for Salient-Pole PMSM Based on Extended EMF in Rotating Reference Frame,” IEEE Transactions on Industry Applications, Vol. 38, No. 4, pp. 1054-1061, 2002.

[60] S. Morimoto, Y. Inoue, T. Weng and M. Sanada, “Position Sensorless PMSM Drive System Including Square-wave Operation at High-speed,” Conference Record of the 2007 IEEE Industry Applications Conference, 42nd IAS Annual Meeting, 23-27 Sep. 2007, pp.676-682.

[61] Y. Inoue, K. Yamada, S. Morimoto and M. Sanada, “Expanding the Operating Speed Range of Model-based Sensorless Control for IPMSMs,” Conference Record of the 2007 IEEE Industry Applications Conference, 42nd IAS Annual Meeting, 23-27 Sep. 2007, pp.2386-2392.

[62] N. Matsui and M. Shigyo, “Brushless DC Motor without Position and Speed Sensors,” IEEE Transactions on Industry Applications, Vol. 28, No. 1, pp. 120-127, Jan./Feb. 1992.

[63] Z. Chen, M. Tomita, S. Doki and S. Okuma, “New Adaptive Sliding Observer for Sensorless Control of Surface Permanent Magnet Synchronous Motor,” Proc. IPEMC2000, The 3rd Int. Power Electronics and Motion Control Conf., 15-18 Aug. 2000, Beijing, China, pp. 180-185.

[64] P. B. Schmidt and A. H. Wijenayake, “Sensorless Control of a Permanent Magnet Synchronous Machine Down to Near Zero Speed Applied to Position Motion Control,” Conf. Record of the 1996 IEEE IAS, 31st IAS Annual Meeting, 6-10 Oct. 1996, San Diego, CA, USA, Vol. 1, pp. 21-28.

[65] A. B. Kulkarni and M. Ehsani, “A Novel Position Sensor Elimination Technique for the Interior Permanent-Magnet Synchronous Motor Drive,” IEEE Transactions on Industry Applications, Vol. 28, No. 1, pp. 144-150, Jan./Feb. 1992.

[66] S. Ogasawara and H. Akagi, “Implementation and Position Control Performance of a Position-Sensorless IPM Motor Drive System Based on Magnetic Saliency,” IEEE Transactions on Industry Applications, Vol. 34, No. 4, pp. 806-812, Jul./Aug. 1998.

[67] S. Ogasawara and H. Akagi, “An Approach to Real-Time Position Estimation at Zero and Low Speed for a PM Motor Based on Saliency,” IEEE Transactions on Industry Applications, Vol. 34, No. 1, pp. 163-168, Jan./Feb. 1998.

[68] R. Mizutani, T. Takeshita and N. Matsui, “Current Model-Based Sensorless Drives of Salient-Pole PMSM at Low Speed and Standstill,” IEEE Transactions on Industry Applications, Vol. 34, No. 4, pp. 841-846, Jul./Aug. 1998.

[69] M. Schroedl, “Sensorless Control of Permanent Magnet Synchronous Motors,” Electric Machines and Power Systems, Vol. 6, pp. 173-185, Taylor & Francis, Inc., Washington, D.C., 1994.

[70] M. Schroedl, “Sensorless Control of AC Machines at Low Speed and Standstill Based on the “INFORM” Method,” Conf. Record of the 1996 IEEE IAS 31st IAS Annual Meeting, Vol. 1, pp. 270-277., 8-10 Sep. 1997, Trondheim, Norway, Proc., Vol. 4, pp. 541-546.

[71] T. Noguchi, K. Takehana and S. Kondo, “Mechanical-Sensorless Robust Control of Permanent-Magnet Synchronous Motor Using Phase Information of Harmonic Reactive Power,” IEEE Transactions on Industry Applications, Vol. 37, No. 6, pp. 1786-1792, Nov./Dec. 2001.

[72] P. L. Jansen, M. Corley and R. D. Lorenz, “Flux, Position, and Velocity Estimation in AC Machines at Zero Speed via Tracking of High Frequency Saliencies,” Proc. EPE’95, Sevilla, Spain 1995, pp. 154-160.

[73] L. Wang and R. D. Lorenz, “Rotor Position Estimation for Permanent Magnet Synchronous Motor Using Saliency-Tracking Self-Sensing Method,” Conf. Record of the IEEE 2000 IEEE Industry Applications Conference, 35th IAS Annual Meeting and World Conf. on Industrial Applications of Electrical Energy, 8-12 Oct 2000, Roma, Italy, Vol. 1, pp. 445-450.

[74] L. Wang, G. Qingding and R. D. Lorenz, “Sensorless Control of Permanent Magnet Synchronous Motor,” Proc. IPEMC 2000, The 3rd Int. Power Electronics and Motion Control Conf., Aug. 15-18, 2000, Beijing, China, pp. 186-190.

[75] A. Consoli, G. Scarcella and A. Testa, “Industry Application of Zero-Speed Sensorless Control Techniques for PM Synchronous Motors,” IEEE Transactions on Industry Applications, Vol. 37, No. 2, pp. 513-521, Mar./Apr. 2001.

[76] M. W. Degner and R. D. Lorenz, “Using Multiple Saliencies for the Estimation of Flux, Position, and Velocity in AC Machines,” IEEE Transactions on Industry Applications, Vol. 34, No. 5, pp. 1097-1104, Sep./Oct. 1998.

[77] M. J. Corley and R. D. Lorenz, “Rotor Position and Velocity Estimation for a Salient-Pole Permanent Magnet Synchronous Machine at Standstill and High Speeds,” IEEE Transactions on Industry Applications, Vol. 34, No. 4, pp. 784-789, Jul./Aug. 1998.

[78] J. Ha, K. Ide, T. Sawa and S. Sul, “Sensorless Rotor Position Estimation of an Interior Permanent-Magnet Motor From Initial States,” IEEE Transactions on Industry Applications, Vol. 39, No. 3, pp. 761-767, May/Jun. 2003.

[79] M. Leksell, L. Harnefors and H. Nee, “Machine Design Considerations for Sensorless Control of PM Motors,” ICEM’98 International Conference on Electrical Machines, Sep. 2-4, 1998, Istanbul, Turkey, Vol. 1, pp. 619-624.

[80] J. Jang, S. Sul, J. Ha, K. Ide and M. Sawamura, “Sensorless Drive of Surface-Mounted Permanent-Magnet Motor by High-Frequency Signal Injection Based on Magnetic Saliency,” IEEE Transactions on Industry Applications, Vol. 39, No. 4, pp. 1031-1039, Jul./Aug. 2003.

[81] J. Jang, J. Ha, M. Ohto, K. Ide and S. Sul, “Analysis of Permanent-Magnet Machine for Sensorless Control Based on High-Frequency Signal Injection,” IEEE Transactions on Industry Applications, Vol. 40, No. 6, pp. 1595-1604, Nov./Dec. 2004.

[82] J. X. Shen, Z. Q. Zhu and D. Howe, “Sensorless Flux-Weakening Control of Permanent-Magnet Brushless Machines Using Third Harmonic Back EMF,” IEEE Transactions on Industry Applications, Vol. 40, No. 6, pp. 1629-1636, Nov./Dec. 2004.

[83] S. Ostlund and M. Brokemper, “Sensorless Rotor-Position Detection from Zero to Rated Speed for an Integrated PM Synchronous Motor Drive,” IEEE Transactions on Industry Applications, Vol. 32, No. 5, pp. 1158-1165, Sep./Oct. 1996.

[84] M. Tursini, R. Petrella and F. Parasiliti, “Initial Rotor Position Estimation Method for PM Motors,” IEEE Transactions on Industry Applications, Vol. 39, No. 6, pp. 1630-1640, Nov./Dec. 2003.

[85] P. B. Schmidt, M. L. Gasperi, G. Ray and A. H. Wijenayake, “Initial Rotor Angle Detection of a Non-Salient Pole Permanent Magnet Syncrhonous Machine,” Conf. Record of the 1997 IEEE Industry Applications Society 32nd Annual Meeting, New Orleans, Lousiana, Oct. 5-9, 1997, Vol. 1, pp. 459-463.

[86] N. Matsui and T. Takeshita, “A Noble Starting Method of Sensorless Salient-Pole Brushless Motor,” 1994 IAS IEEE Industry Applications Society 29th Annual Meeting, Oct. 2-6 1994, Denver, Colorado, Vol. 1, pp. 386-392.

[87] L. Cardoletti and A. Cassat, “Sensorless Position and Speed Control of a Brushless DC Motor from Start-up to Nominal Speed,” EPE Journal, Vol. 2, No. 1, pp. 25-34, Mar. 1992.

[88] N. Kasa and H. Watanabe, “A Sensorless Position Control by Salient-Pole Brushless DC Motor,” 7th European Conf. on Power Electronics and Applications, 8-10 Sep. 1997, Trondheim, Norway, Proc., Vol. 4, pp. 529-534.

[89] S. Kondo, A. Takahashi and T. Nishida, “Armature Current Locus Based Estimation Method of Rotor Position of Permanent Magnet Synchronous Motor without Mechanical Sensor,” Conf. Record of the 1995 IEEE IAS, 30th IAS Annual Meeting, Oct. 8-12, 1995, Orlando, Florida, USA, Vol. 1, pp. 55-60.

[90] G. Foo and M. F. Rahman, “Sensorless Direct Torque and Flux Controlled Interior Permanent Magnet Synchronous Motor Drive over a Wide Speed Range,” Australian Journal of Electrical & Electronics Engineering, Vol. 6, No. 2, pp. 121-131, 2009.

[91] G. Foo, S. Sayeef and M. F. Rahman, “Sensorless Direct Torque and Flux Control of an IPM Synchronous Motor Drive at Low Speed and standstill,” Australian Journal of Electrical & Electronics Engineering, Vol. 6, No. 3, pp. 221-232, 2009.

[92] S. Sayeef, G. Foo and M. F. Rahman, “Rotor Position and Speed Estimation of a Variable Structure Direct Torque Controlled IPM Synchronous Motor Drive at Very Low Speeds,” Australian Journal of Electrical & Electronics Engineering, Vol. 6, No. 3, pp. 271-280, 2009.

[93] H. Kim, K. K. Huh and R. D. Lorenz, "A Novel Method for Initial Rotor Position Estimation for IPM Synchrounous Machine Drives," IEEE Transactions on Industry Applications, Vol. 40, No. 5, pp. 1369-1378, Sep./Oct. 2004.

[94] Y. Jeong, R. D. Lorenz, T. M. Jahns and S. Sul, "Initial Rotor Position Estimation of an Interior Permanent-Magnet Synchronous Machine Using Carrier-Frequency Injection Methods," IEEE Transactions on Industry Applications, Vol. 41, No. 1, pp. 38-45, Jan/Feb, 2005.

[95] M. Tursini, R. Petrella and A. Safati, "Speed and Position Estimation for PM Synchronous Motor using Self-compensated Back-EMF Observers," 32nd Annual Conference on IEEE Industrial Electronics, IECON 2006, 6-10 Nov. 2006, Paris, pp. 5087-5092.

[96] "Current Transducer LTS 15-NP Data Sheet," *http://www.lem.com/docs/products/lts%2015-np%20e.pdf*, LEM, 2006.

[97] "dsPIC30F4011/4012 Data Sheet," *http://ww1.microchip.com/downloads/en/devicedoc/70135C.pdf*, Mircrochip Tech. Inc., 2005.

[98] "PCI-6110E/6111E User Manual," *http://www.ni.com/pdf/manuals/321759b.pdf*, NI Corp., Apr. 1998.

[99] "PCI-6534 Data Sheet," *http://www.ni.com/pdf/products/us/3daqsc378-379.pdf*, NI Corp., 2010.

[100] "NI PCI-6534," *http://sine.ni.com/nips/cds/view/p/lang/en/nid/13505*, NI Corp., 2010.